Democratic and Popular Republic of Algeria
Ministry of Higher Education and Scientific Research
University Mohamed Khider of Biskra
Faculty of Exact Sciences and Nature and Life

Department of Matter Sciences
Domain of Matter Sciences
Section of Physics

Thesis Presented to obtain the Degree of
Doctorate 3rd cycle (LMD)

Speciality: Physics of thin films

Preparation and characterization of Titanium dioxide and Zinc oxide thin films via Sol-Gel (spin coating) technique for optoelectronic applications

Presented by:

Dahnoun Mohamed

To the Jury composed by:

Attaf Nadir	*Professor*	*University of Constantine 1*	*President*
Attaf Abdallah	*Professor*	*University Med Khider of Biskra*	*Reporter*
Saidi Hanane	*Professor*	*University Med Khider of Biskra*	*Co-Reporter*
Guerbous Lakhdar	*Research Director*	*Nuclear Research Center of Algiers*	*Examiner*
Bentamam Hachemi	*Professor*	*University Med Khider of Biskra*	*Examiner*

Academic Year
2019-2020

Acknowledgements

Firstly, I thank **GOD** the whole powerful for having agreed his infinite kindness, courage, the force and patience to complete this modest work.

After that, I make a point of profoundly thanking to my supervisor **Prof. Attaf Abdallah**, dean of Faculty of Exact Sciences and Sciences of Nature and Life in Mohamed Khider University of Biskra, for his help, support, guidance and encouragement. He has been a great support on all fronts and made my Doctorate thesis journey a memorable experience.

I thank also the professor **Saidi Hanane** for her assistance to completing this thesis.

I address my sincere thanks to **Prof. Nadir Attaf** for the honor that makes to me by accepting the presidency of this jury.

I am grateful to **Prof. Lakhdar Guerbous** and **Prof. Hachemi Bentamam** who agreed to accept to belong to the jury and to examine my work.

My thanks go to my parents and my wife for their unconditional love and support, I am very grateful for what they have done for me.

Special thanks go to my friends **Dr. Yahia Anouar** and **Dr. Labed Mohamed** for the participation they showed in my work and for the stimulating discussions.

I would also like to acknowledge **Prof. Tibermacine Toufik** for his generous help in the experimental phase.

Finally, I wish to address my thanks to all the teachers and students of the department of sciences of matter especially the teachers of physics and the members of thin films laboratory of our university every one by his name.

Dedication

To my parents,

To my wife,

To my son Zaid,

To my brothers and sisters and everyone who supported me.

Table of contenants

List of tables

Figure list

Preface

Transparent conducting thin films are a class of material which achieve large values of electrical conductivity, whilst maintaining a high transmission in the visible range of the electromagnetic spectrum. Since the realisation of this type of material, vast amounts of research and development have gone into commercialising these thin film coatings. The current commercial products are based on n-doped metal oxide thin films, so-called transparent conducting oxides (TCOs). These films have a far-reaching range of applications from heat-mirror window-coatings, which control the transmission of infrared energy into and out-of buildings, to their use as the transparent electrode materials in photovoltaic cells, touch-screen technology, flat panel displays and gas sensors…etc.

The first TCO material was reported in 1907 when K. Badeker sputter coated a thin film of cadmium and heat treated the sample in air. The heating step led to the incomplete oxidation of the cadmium to non-stoichiometric cadmium oxide, leaving oxygen vacancies in its structure. The oxygen vacancies led to penta-valent cadmium ions, which generated occupied defect energy levels from which electronic promotion into the cadmium oxide conduction band could easily occur.

During last decades, the conductive transparent oxides (TCO), and in particular the Indium Oxide (In_2O_3), Tin Oxide (SnO_2), Titanium Dioxide (TiO_2) and Zinc Oxide (ZnO) were synthesised as thin films using different methods such as thermal evaporation, sputtering, chemical vapour deposition (CVD), spray pyrolysis and sol-gel. Each methodology has associated pros and cons and careful consideration of the resulting film properties such as adhesion, microstructure, crystallinity, transparency and conductivity must be taken into account.

The main objective of this thesis work is to optimize the growth conditions of TiO_2 and ZnO thin films for photovoltaic applications (front electrodes for solar cells, photocatalysis, gas sensors…etc.), employing cost effective technique which is Sol-Gel spin-coating process. Sol–gel processes are particularly adapted to produce TiO_2 and ZnO thin films in a simple, low-cost and highly controlled way. The sol–gel process, called also soft chemistry, allows to elaborate a solid material from a solution by using a sol or a gel as an intermediate step, and at much lower temperatures than that is possible by traditional methods of preparation. The synthesis of solid materials via ‘soft chemistry’ often involves wet chemistry reactions and sol-

gel chemistry based on the transformation of molecular precursors into an oxide network by hydrolysis and condensation reactions.

The results are presented in 5 chapters. An overview about the structural, optical and electrical properties of Titanium dioxide and Zinc oxide is briefly presented in **Chapter 1** with focus on their photovoltaic applications.

Chapter 2 deals with the various deposition methods and characterisation tools employed in thin films science and the different methods of calculation of the deposit's characteristics (crystallite size, conductivity and optical gap...etc.).

Chapter 3 gives the definition, different steps and diverse methods of Sol-Gel process then we describe the substrate preparation steps as well as the preparation of solutions used in TiO_2 and ZnO thin films deposition. Next, details of the films deposition procedure will be given in charts.

In order to prove that films with appropriate properties (make it applicable in photovoltaic) can be deposited using simple techniques, **Chapter 4** is consecrated to investigate the influence of different parameters such as the nature of stabilizer, annealing temperature, molar concentration and Zn doping on TiO_2 thin films properties. With a view to generalize the results obtained previously on the one hand and to compare these results on the other hand **Chapter 5** is devoted to study the effect of some parameters such as the nature of stabilizer, annealing temperature and Ga doping on ZnO thin films properties.

Finally, this report will conclude with highlights the major results and the comparison between TiO2 and ZnO thin films and proposes the future steps for improving the quality of these films.

Chapter I

A Survey on TiO_2, ZnO and their applications

I. 1. Introduction

According to the energy bands theory, three electric states are possible: metal, insulator and semiconductor. In metal, the conduction band (BC) and valence band (BV) overlap, allowing the free movement of the electrons. The semiconductor has a forbidden band which separates BV and BC commonly called gap and noted Eg. The electrons can't take energies located in this band. It is necessary that they acquire energy to pass in BC. For a higher gap, one speaks about insulator because even at ambient temperature, BC is empty; their gap is higher than 4 eV [1].

A material, with a transparency in the visible and properties of conduction, has paradoxical properties from a physical point of view. In fact, conducting materials such as metals reflect most of the electromagnetic spectrum whose part of visible thanks to their free electrons. Glasses are transparent materials in the visible one. Glass is an amorphous material, i.e. Its structure is not crystallized. This material has a very high value of gap and can't lead an electrical current. It is then known as insulating. At first sight, the association of the two properties is incompatible.

However, the semiconductors having a large gap (at least higher than 3.1 eV correspondents with a wavelength of 400 nm) are theoretically transparent in the field of the visible one. The deposit in thin layer of this type of material ensures a weak absorption.

Thanks to the doping of material, that is to say a contribution of impurities which increases the number of free electrons, conduction is increased to make a "bad metal ".
Metallic oxides are in general semiconductors with large gap. They can be symbolized by MO with M an atom of metal and O an atom of oxygen [1].

I. 2. What is transparent conducting Oxide?

Transparent conducting oxides (TCOs) constitute a unique class of materials, which combine two physicals properties together, high optical transparency and high electrical conductivity. These properties are generally considered to be mutually exclusive of each other since high conductivity do metals possess a property while insulators are optically transparent. This peculiar combination of physical properties is achieved by generating free electron or hole carriers in a material having a sufficiently large energy band gap (i.e., >3.1 eV) so that it is non-absorbing or transparent to visible light.

The charge carriers are usually generated by doping the insulator with suitable dopants and by defects. It is no wonder that this unique material property makes TCOs an important material in technology and useful in commercial applications.

The TCOs used in technological applications should have following characteristics. First, they should be transparent for the visible part of light with transmittance > 80%. Second, they should be a good conductor of electricity with a high enough concentration of electrical carriers, i.e., an electron or hole concentration $\geq 10^{19}$ cm^{-3} and with a sufficiently large mobility ≥ 1 $cm^2\ V^{-1}s^{-1}$. The three most common TCOs are tin doped indium oxide In_2O_3: Sn, fluorine doped tin oxide SnO_2: F, and aluminum doped zinc oxide ZnO: Al. All three of these materials have band gaps above that required for transparency across the full visible spectrum. Note that although these TCOs are considered to be good conductors from the perspective of a semiconductor, they are actually very poor conductors compared to metals.

For example, the best conductivity of In_2O_3: Sn (for indium tin oxide or ITO) is about a factor of 10 to 60 lower than that of a typical integrated circuit contact metal. The low conductance of TCOs compared to metals has important consequences for both TCO and transparent electronics applications. Therefore, an appropriate quantitative measure of the performance of TCOs is the ratio of the electrical conductivity (σ) to the visible absorption coefficient (α). Thus, the figure of merit of TCO material is used for quantitative description of TCO performance [2].

$$Figure\ of\ merit = \frac{\sigma}{\alpha} \qquad \text{(I.1)}$$

Haacke [3], defined the figure of merit as a relation between the transmission coefficient T and surface resistance Rs, Φ_{TC} being expressed in Ω^{-1} according to the relation (I.2). This figure of merit allows a comparison between different TCOs.

$$\Phi_{TC} = \frac{T^{10}}{R_s} \qquad \text{(I.2)}$$

I. 3. Titanium dioxide

Titanium (Ti), a silver color transition metal was discovered by William Gregor in 1791. It is the ninth most abundant element and seventh most abundant metal in the Earth's crust [4]. Titanium is a strong and light metal due to high strength and low density and it is not found as a pure metal in nature due to its strong affinity for oxygen, carbon and nitrogen, making it difficult to obtain in the pure state, but it suffers the phenomenon of "passivation", which is the process of making a material "passive", usually by the deposition of a layer of oxide that adheres to the metal surface [5].

Titanium dioxide was first discovered in the early 1900s and the manufacture of titanium white for use as a pigment (anatase form) was first reported in 1923 in France, where soon replaced the lithopone and toxic lead-based pigments in the early 1930s. TiO_2 is found in three different crystallographic structures, namely rutile, anatase and brookite [6].

I. 3. 1. TiO_2 structural properties

TiO_2 occurs in three crystalline polymorphs: rutile, anatase, and brookite. Rutile is thermodynamically most stable phase and has lowest surface energy. (Anatase is more stable at low temperatures). Brookite is difficult to produce and is therefore not of practical interest. The metastable anatase and brookite phases convert irreversibly to rutile phase on heating above 600°C to 800°C temperature [7].

The basic unit-cell structures of these phases are shown in fig I.1 The crystal parameters, the $Ti-O$ interatomic distances, and the $O— Ti— O$ bond angles for the three phases are summarized in table I. 1. Rutile and anatase are both tetragonal, containing 6 and 12 atoms per unit cell, respectively. In both structures, each Ti atom is coordinated to six O atoms and each O atom is coordinated to three Ti atoms. In each case, the TiO_6 octahedron is slightly distorted, with two $Ti— O$ bonds slightly greater than the other four, and with some of the $O— Ti— O$ bond angles deviating from 90°. The distortion is greater in anatase than in rutile. The structure of rutile and anatase crystals has been described frequently in terms of chains of TiO_6 octahedra having common edges. Two and four edges are shared in rutile and anatase, respectively. The third form of TiO_2, brookite shown in fig I. 1(c), has a more complicated structure. It has eight formula units in the orthorhombic cell. The interatomic distances and the $O— Ti— O$ bond angles are similar to those of rutile and anatase. The essential difference is that there are six different $Ti— O$ bonds ranging from 1.87 to 2.04 Å. Accordingly, there are 12 12 different $O— Ti— O$ bond angles ranging from 77° to 105°. In contrast, there are only

two kinds of $Ti—\ O$ bonds and $O—\ Ti—\ O$ bond angles in rutile and anatase. We can also envision brookite as formed by joining together the distorted TiO_6 octahedra sharing three edges.

Table I. 1. Crystal structure data of TiO_2 [8].

Phase	Rutile	Anatase	Brookite
Crystal structure	tetragonal	tetragonal	orthorhombic
Lattice constants (Å)	$a = 4.5936$ $c = 2.9587$	$a = 3.784$ $c = 9.515$	$a = 9.184$ $b = 5.447$ $c = 5.145$
Space group	$P4_2/mnm$	$I4_1/amd$	$Pbca$
Molecule/cell	2	4	8
Volume/molecule (Å^3)	31.2160	34.061	32.172
Density (g/cm^3)	4.13	3.79	3.99
$Ti-O$ bond length (Å)	1.949 (4) 1.980 (2)	1.937 (4) 1.965 (2)	1.87~2.04
$O-Ti-O$ bond angle	81.2° 90°	77.7° 92.6°	77°~105°

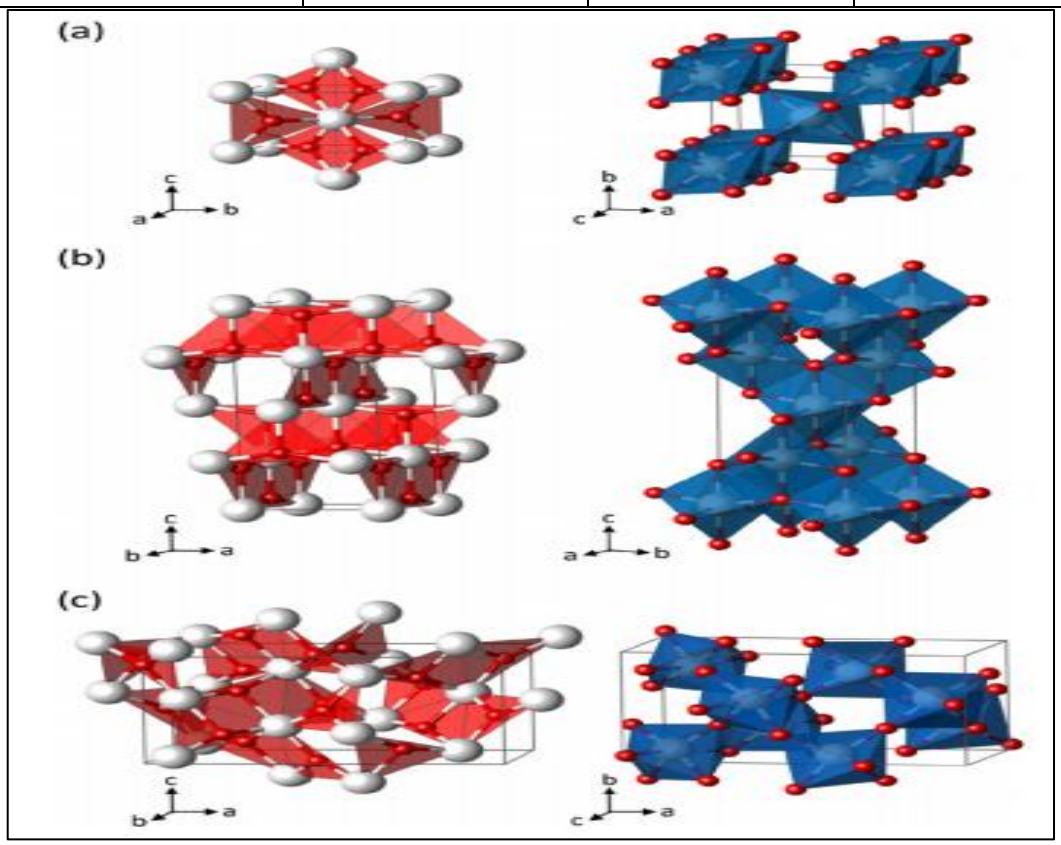

Figure I. 1. Planar Ti_3O building-block representation (left) and TiO_6 polyhedra (right) for the TiO_2 phases rutile (a), anatase (b) and brookite (c) (Ti (white); O (red)) [9].

I. 3. 2. TiO_2 optical properties

Titanium dioxide has a high refractive index *n* in the visible rang. Of the three stable crystalline phases, Rutile has the largest index ($n \approx 2.66$) which is higher than that of the anatase one ($n \approx 2.54$). This combined with a high visible light scattering coefficient, make the Rutile phase suitable for use as a white pigment for the industry (paints, food coloring or pharmaceutical ...) [10, 11].

The TiO_2 transmittance in the visible range associated with an absorption edge around 0.42 μm leads to a high absorption in the ultraviolet which gives it excellent properties such as protective layer from UV, main active component of solar cells…etc.

I. 3. 3. TiO_2 electrical properties

Titanium dioxide is n-type semiconductor. The TiO_2 single crystal has a resistivity about 10^{13} Ω.cm at room temperature and about 10^7 Ω.cm at 250 °C. These values are similar to reported conductivity for a rutile single crystal at 30 °C which was about 5.10^{-14} $\Omega^{-1}.cm^{-1}$. While at 260 °C it was decreased to 3.3×10^{-9} $\Omega^{-1}.cm^{-1}$. Therefore, TiO_2 is generally considered as an insulator for temperatures below 200 °C and it was used for a diversity applications such as a dielectric gate in MOSFET devices. However, the electrical properties of the TiO_2 films can be modified to become very conductive for many applications such as: gas sensors, photocatalyst and solar cells contact [12].

Fig I. 2 depicts TiO_2 band structure as can be seen TiO_2 is a wide band-gap semiconductor material. The gaps of Rutile, Anatase and Brookite have a value of 3 eV, 3.2 eV and 3.1 eV respectively (Eg between the valence band (corresponding to the orbital O_{2p}) and the conduction band (corresponding to Ti^{3d} orbital)). These gap values give rise to transitions corresponding to photons in the ultraviolet range [13].

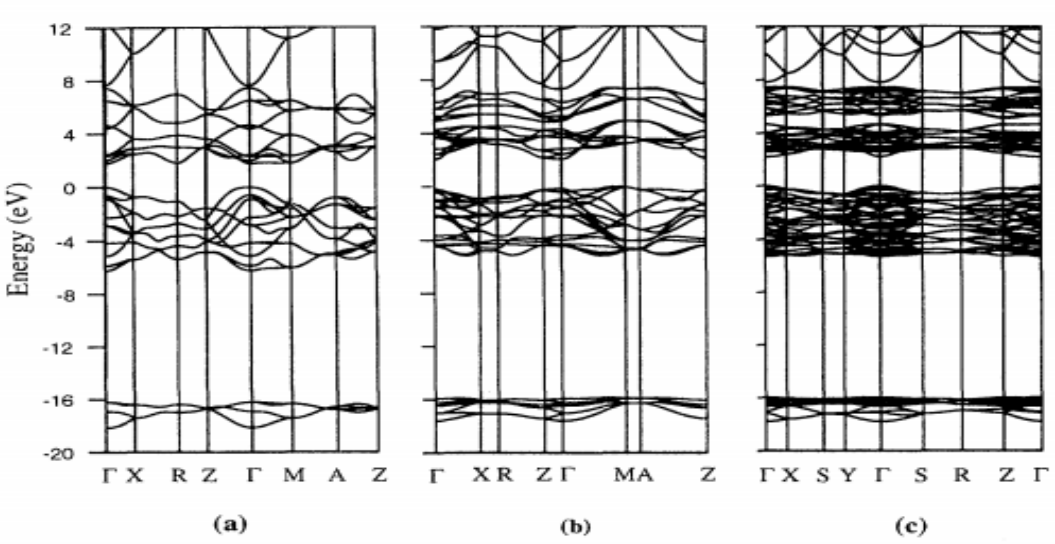

Figure I. 2. TiO_2 band structure for rutile (left panel), anatase (middle panel) and brookite (right panel) [8].

I. 4. TiO_2 applications

TiO_2 is non-toxic and does not make any negative effects inside the human body. Hence, TiO_2 is used in medical tablets and syrups. Due to its high diffraction index, strong light scattering and incident light reflection capacity, it is widely used as a white pigment. TiO_2 is an important material in industrial uses as a main component in paint, pigment, cosmetics etc., [14]. It is also used in optical coatings, beam splitters, anti-reflection coatings, humidity sensors and high temperature oxygen sensors [15, 16]. The temperature, environmentally stable dielectric properties of TiO_2 is characterized by high relative dielectric constant and low dielectric loss. This has stimulated research in the fabrication of novel microelectronic devices and microwave communication systems. The properties of TiO_2, like high surface area, high surface to volume ratio, high stability, non-toxic, low cost etc., makes it a potential candidate in photovoltaics (DSSC).

I. 4. 1. Photocatalyst

Photocatalysis is defined as the acceleration of a photo reaction in the presence of a catalyst. The photo catalytic activity depends on the ability of the catalyst to create electron-hole pairs which undergo secondary reactions (equation (I. 3)).

$$TiO_2 \overset{h\nu}{\rightarrow} TiO_2 + h^+_{BV} + e^-_{BC} \qquad \text{(I.3)}$$

The discovery of water electrolysis by TiO_2 made photo catalysis practically possible. TiO_2 is the most common semiconductor used as photo catalyst which is inexpensive and commercially available. It is a good photo catalyst under UV light. And, when doped with nitrogen ions or metal oxides, it shows photo catalytic activity in visible light also [17]. The anatase phase of TiO_2 is arguably the most photo active [18]. The photo catalytic activity of TiO_2 comes from the generation of OH radicals by oxidation of OH^- anions eq (I. 4) and the generation of O_2^- radicals by reduction of O_2 eq (I. 5).

$$OH^-_{ads} + h^+ \rightarrow OH^\circ_{ads} \quad \text{(I.4)}$$

$$O_2 + e^- \rightarrow O_2^{\circ -} \quad \text{(I.5)}$$

As can be seen in the schematic diagram given in fig I. 3 both of these radical anions can react with other species to degrade or otherwise change them, making TiO_2 an effective photo catalyst for many applications. TiO_2 and UV radiation from the Sun can be used to split the hydrocarbon present in the crude oil into water and carbon dioxide. This photo catalytic activity of TiO_2 is useful in removing the oil slicks float on top of the ocean.

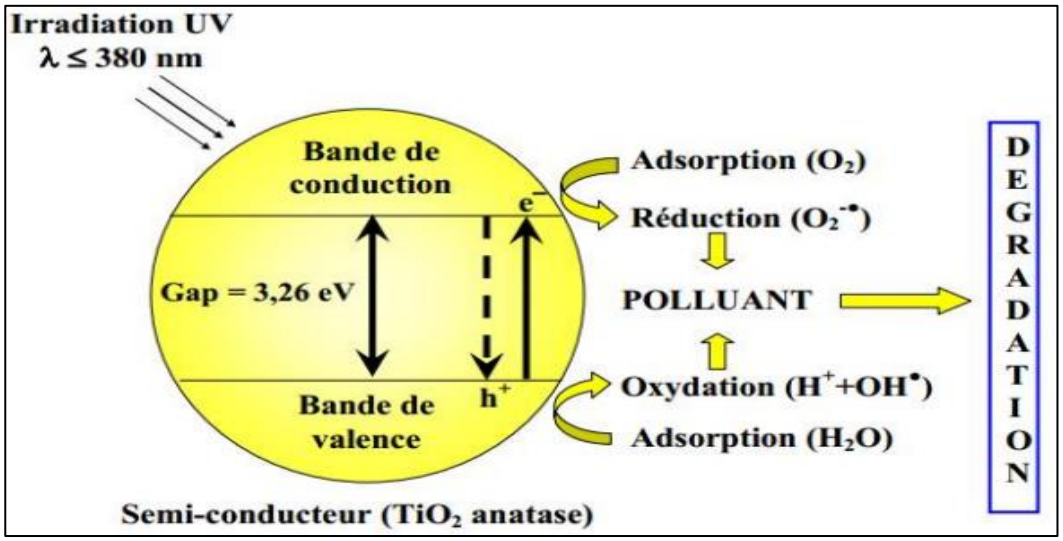

Figure I. 3. Schematic diagram of the photocatalytic process in TiO_2 anatase particle [19].

I. 4. 2. Dye Sensitized Solar Cells

TiO_2 is photo conductive n-type semiconductor which has the potential as photo electrode for energy conversion of solar energy into electricity. One of the most common semiconductors used in DSSC is TiO_2 (anatase) due to its superior properties, like nontoxic, inexpensive, high photosensitivity, structural stability under solar irradiation, good chemical stability, bio compatibility etc. The photovoltaic behavior of TiO_2 depends on crystalline nature, defects on the surface, photon absorption ability, particle size, surface area, surface roughness, surface hydroxyl group density etc. TiO_2 has low quantum yield for photo chemical conversion of solar energy. Hence, the use of colloidal suspensions with the addition of dye molecules has improved the efficiency of solar cells [20]. TiO_2 is sensitive to UV light due to its large band gap with relatively high electron-hole recombination rate. By designing proper electrode thickness and sensitization dyes, TiO_2 based DSSCs are able to absorb more light [21].

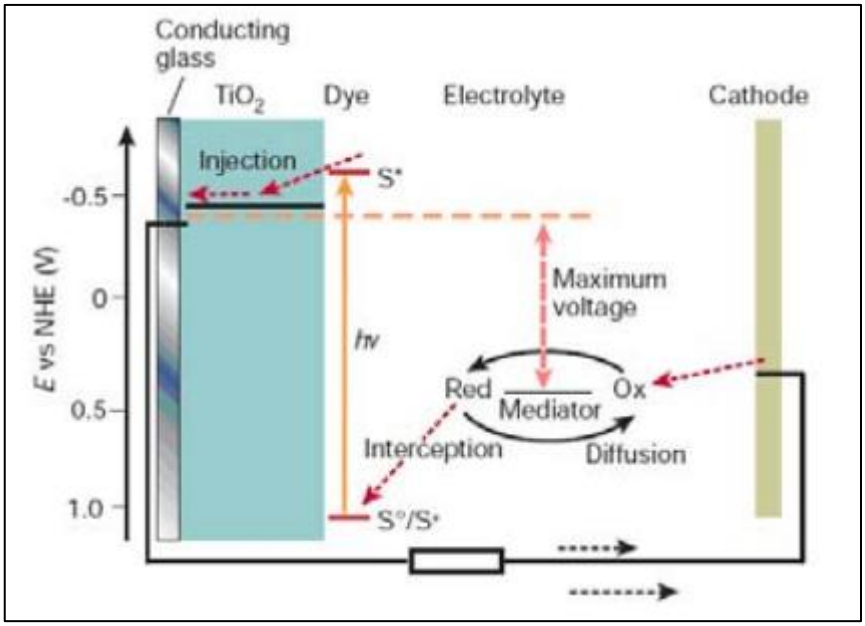

Figure I. 4. Energy diagram of the dye solar cell [22].

I. 5. Zinc oxide presentation

Zinc oxide is an important material in the electronic industry. It is an II – VI oxide semiconductor with the formula ZnO. ZnO is a white powder that is insoluble in water it has also high ionicity compared with Si, Ge and III – V compounds. Besides that, the material has some distinct features like non-stoichiometric defect structure, anisotropy in crystal structure, large direct band gap, strong absorption in the UV region, transparency in the visible region, large variation of conductivity and high surface sensitive catalytic activity in different ambient . These properties make it useful for photovoltaic solar cell windows, IR reflective coatings, piezoelectric and guided optical wave devices, surface acoustic-wave devices, phosphors and gas sensors. Ideally, pure zinc oxide is an intrinsic semiconductor with a band gap of 3.2 eV at room temperature. It crystallizes in a hexagonal wurtzite lattice. The mean lattice constants are a=3.25 A° and c=5.206 A° which slightly changes with stoichiometry of the composition. But practically, ZnO is always n-type due to its native defects created during preparation. Different workers reported that the non- stoichiometry is due to excess zinc in the interstitial position or oxygen vacancy or both. This non-stoichiometry causes a large variation in the electrical conductivity of the ZnO film and also makes it surface sensitive to the adsorption of chemical gas species [23,24].

I. 5. 1. ZnO structural properties

As mentioned earlier, ZnO is an II – VI semiconductor, displays piezoelectric effects, and has a band gap in the near UV range (3.3 eV) at room temperature. Mostly, the group II–VI binary compound semiconductors have either cubic zinc-blende or hexagonal wurtzite structure. Although ZnO can form in wurtzite, zinc blende, or rocksalt crystal structures under different conditions, its only thermodynamically stable phase is the hexagonal wurtzite crystal structure.

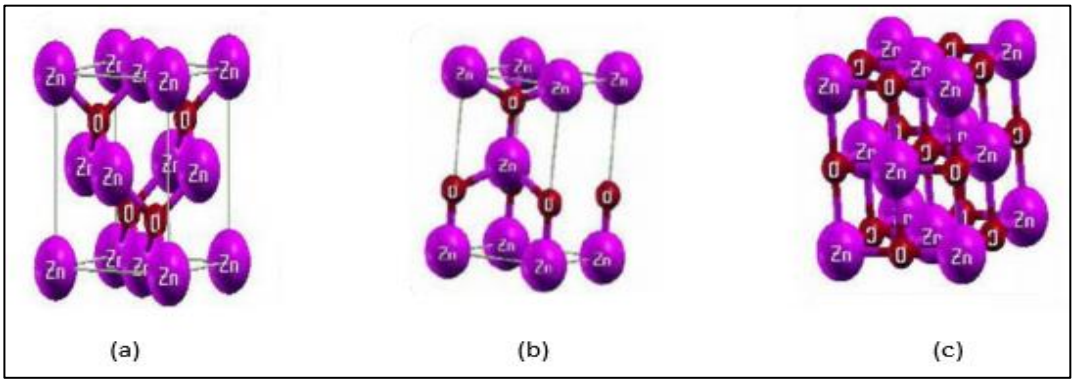

Figure I. 5. The three possible structures of Zinc oxide (a) Zinc blend, (b) Hexagonal (wurtzite) and (c) Rocksalt [25].

So, normally, ZnO crystallizes in hexagonal wurtzite crystal structure where each zinc atom is tetrahedrally coordinated to four oxygen atoms and whose lattice constants a and c are 3.24 Å and 5.2 Å, respectively. A schematic diagram of wurtzite crystal structure of ZnO is shown in Figure (1.6, (a)). The structure is composed of two interpenetrating hexagonal-close-packed (hcp) sublattices. The wurtzite unit cell, shown in Figure (1.6, (b)), contains four atoms, two anions and two cations.

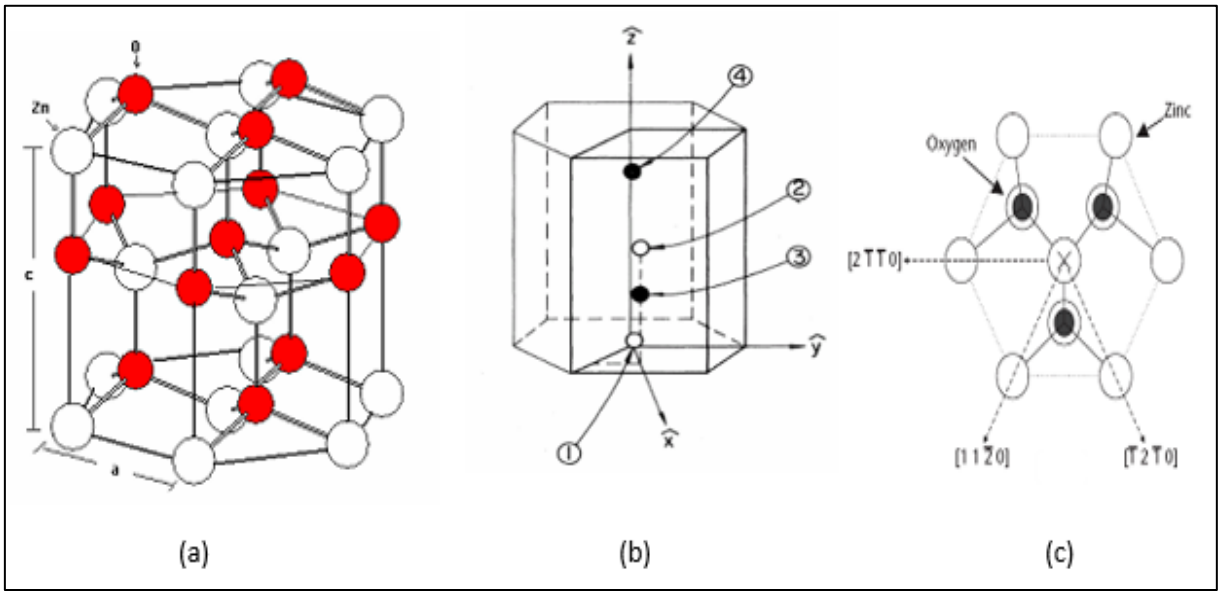

Figure 1. 6. (a) A schematic diagram of wurtzite crystal structure of ZnO, (b) Hexagonal close-packed structure with four basis atoms, (c) Projection along the [0001] direction (pointing out of the plane of paper, denoted by the "X" mark at the center) [26, 27].

I. 5. 2. ZnO electrical properties

The electronic structure of the zinc and oxygen is:

$$O: 1s^2 2s^2 2p^4$$

$$Zn: 1s^2 2s^2 2p^6 3s^2 3p^6 3d^{10} 4s^2$$

Production of quality p-type ZnO films has been problematic, mostly due to defects caused by dopants induced stresses in the crystal. Very low formation energies for oxygen vacancies and zinc interstitials in ZnO have been calculated and likely explain the native n-type conductivity observed in as-grown films [28].

The electrical resistivity *(ρ)* of ZnO films is determined by the carrier concentration *(n)* and carrier mobility *(μ)*, which is also presented as $\rho = 1/(n.e.\mu)$ where *e* is the electron charge. It is known that *e* is a constant, so, for obtaining low resistivity, the carrier concentration

(n) and carrier mobility *(μ)* should be simultaneously maximized, and most research papers have suggested that the method of achieving maximum carrier concentration is by oxygen vacancies and doping.

The literature [29] indicates, "If an oxygen vacancy is created in a perfect crystal, two electrons are created in the crystal and contributed as ionized donors". But, if there is too much oxygen created in the thin films, sub-oxides will form, causing the resistivity to rise." In addition to the oxygen vacancies, doping (most used dopants are: Al, Ga, In, B, Si, Ge, F) also can change the electrical conductivity of ZnO. As host cations are substituted by elements with a valence higher than that of the host, the extra electrons can become conduction electrons. To avoid the charge neutrality, substitution of a higher valence element creates extra electrons. It is well known that pure zinc oxide films usually have a characteristic high resistivity due to their low carrier concentration. Therefore, in order to decrease resistivity, we can increase either the carrier concentration or the carrier mobility in zinc oxide thin films. The former is probably obtained by oxygen and/or zinc non-stoichiometry, or doping with an impurity.

But, Johnson et al. [30] in 1947 stated that increasing the carrier density via doping or oxygen vacancies is self-limiting because the increase of the number of free carriers decreases the mobility of carriers due to carrier-carrier scattering. Therefore, there is a trade-off relation between the carrier density and the carrier mobility for obtaining low resistivity.

I. 5. 3. Optical properties and luminescence

Zinc oxide is a material transparent in visible with high transmittance ($T > 80\%$) . The refractive index n of bulk ZnO is equal to 2. In thin films the value of the index n and the absorption coefficient is dependent on the conditions of elaboration of thin layers where n has a value between 1.7 and 2.2. ZnO has the extremely large exciton binding energy of 60 meV which is much greater than the thermal energy (26 meV) at room temperature [24, 26].

The photoluminescence of ZnO typically consists of UV emission (350nm) and broad visible band emission (550 nm). The UV emission observed in ZnO is believed to result from band edge excitonic emission while the visible emission is due to defect emission [31].
Green emission is the most commonly observed visible emission in ZnO, although other colors like yellow and orange have also been reported. The origin of the green emission is the most controversial. It was suggested that the green emission was due to transitions between electron close to the conduction band and a deeply trapped hole at V_0^{++} [32].

I. 6. Applications of Zinc Oxide thin films

Because of its diverse properties, both chemical and physical, zinc oxide is widely used in many areas. It plays an important role in a very wide range of applications. ZnO exhibits the phenomenon of luminescence (chiefly photoluminescence-emission of light under exposure to electromagnetic radiation). Because of this property it is used in FED (field emission display) equipment, such as televisions. It is superior to the conventional materials, sulfur and phosphorus (compounds exhibiting phosphorescence), because it is more resistant to UV rays, and also has higher electrical conductivity. The photoluminescent properties of zinc oxide depend on the size of crystals of the compound, defects in the crystalline structure, and also on temperature [33].

One of the most important applications of zinc oxide in electronics is in the production of varistors. These are resistors with a non-linear current-voltage characteristic, where current density increases rapidly when the electrical field reaches a particular defined value. They are used, among other things, as lightning protectors, to protect high-voltage lines, and in electrical equipment providing protection against atmospheric and network voltage surges. These applications require a material of high compactness, since only such a material can guarantee the stability and repeatability of the characteristics of elements made from it [33]. Otherwise, due to their piezoelectric properties, the ZnO thin films can be used as pressure sensor.

I. 6. 1. ZnO as gas sensor

The most common sensing materials are metal oxide semiconductors (TiO_2, ZnO and SnO_2…), which provide sensors with several advantages such as low cost, short response time, wide range of target gases, long lifetime and high sensitivity. As sensors, various forms of fabricated ZnO are used i.e. ZnO single crystals, ZnO pellets and ZnO thin films figure I. 7.
The exact fundamental mechanisms that cause a gas response are still controversial, but essentially trapping of electrons at adsorbed molecules and band bending induced by these charged molecules are responsible for a change in conductivity. The negative charge trapped in these oxygen species causes an upward band bending and thus a reduced conductivity compared to the flat band situation. As shown in figure I. 8, when O_2 molecules are adsorbed on the surface of metal oxides, they would extract electrons from the conduction band E_c and trap the electrons at the surface in the form of ions, the oxygen is adsorbed in the form of O^{2-}, O^- and O^{2-} depending on the operating temperature [34, 35]. This will lead a band bending and an

electron-depleted region. The electron-depleted region is so called space-charge layer, of which thickness is the length of band bending region. Reaction of these oxygen species with reducing gases or a competitive adsorption and replacement of the adsorbed oxygen by other molecules decreases and can reverse the band bending, resulting in an increased conductivity. Figure I. 8 schematically shows the structural and band model of conductive mechanism upon exposure to reference gas with or without CO. When gas sensors exposure to the reference gas with CO, CO is oxidized by O^- and released electrons to the bulk materials. Together with the decrease of the number of surface O^-, the thickness of space-charge layer decreases. Then the Schottky barrier between two grains is lowered and it would be easy for electrons to conduct in sensing layers through different grains. However, the mechanism in figure I. 8 is only suitable for n-type semiconducting metal oxides of which depletion regions are smaller than grain size [35].

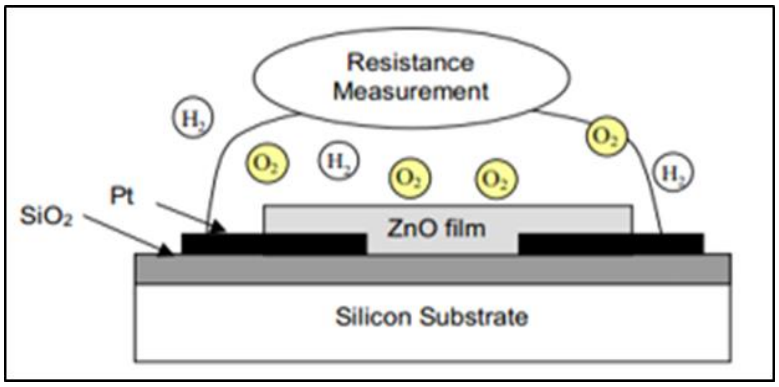

Figure I. 7. ZnO gas sensor structure [36].

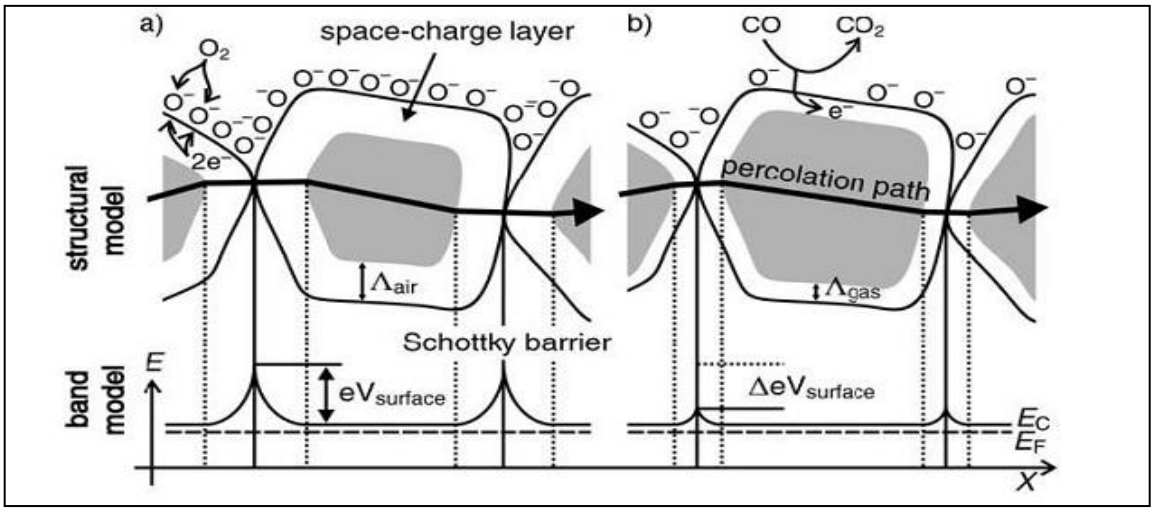

Figure I. 8. Structural and band models of conductive mechanism upon exposure to reference gas (a) With or (b) without CO [36].

I. 6. 2. ZnO for Photocatalytic activity

As mentioned in paragraph (I. 4. 1.) photocatalysis is defined as the acceleration of a photo reaction in the presence of a catalyst. Since few years, photocatalytic processes involving semiconductor ZnO Nanostructures under UV light illumination have been shown to be potentially beneficial and helpful in the treatment of various hazardous pollutants. Different studies have proved this with different pollutants like dyes, drugs, surfactants, pesticides, herbicides, insecticides and fungicides that can be completely mineralized in the presence of ZnO Nanostructures.

TiO_2 exhibits photocatalytic activity below the intensity of UV light. ZnO provides similar or superior activity to that of TiO_2, but is less stable and less sensitive to photocorrosion. Better stability, however, is provided by zinc oxide of nanometric dimensions, which offers better crystallinity and smaller defects. The photocatalytic activity of ZnO can be further improved, and the range of the visible spectrum for zinc oxide can be extended, by adding other components [33].

I. 6. 3. ZnO as transparent electrodes for solar cells

ZnO is obviously one of the best candidates among semiconductors to produce transparent electrodes for solar cells (thin film solar cells, amorphous silicon solar cells and dye sensitized solar cells (DSSC)) due to its high transparency and low resistivity, in addition, it can be synthesized easily and inexpensively into different shapes and sizes, and is environment friendly and stable indefinitely [37].

Refrences

[1] J. Garnier, *"Elaboration de couches minces d'oxydes transparents et conducteurs par spray CVD assiste par radiation infrarouge pour applications photovoltaïques ",* Doctorat thesis, Higher National school of Arts and Trades, Paris, 2009.

[2] H. Dixit, "*First-Principles Electronic Structure Calculations of Transparent Conducting Oxide Materials ",* Doctorate Thesis, University Antwerpen, Belgium, 2012.

[3] G. Haacke, *"New figure of merit for transparent conductors"*, j. Appl. Phys. 47 (1976) 4086.

[4] J. Barksdale, "*Titanium, Its Occurrence.*" Chemistry, and Technology, 2nd Edition, Roland Press Company, New York (1966).

[5] K. G. Budinski, *"Surface Engineering for Wear Resistance. (Retroactive Coverage)."* Prentice-Hall, Inc, Englewood Cliffs, New Jersey 07632, United States, 1988. 420 (1988).

[6] M. J. Gázquez., J. P. Bolivar., R. Garcia-Tenorio., F. Vaca, *"A review of the production cycle of titanium dioxide pigment."* Materials Sciences and Applications 5 (07) (2014) 441-458.

[7] A. Pottier., S. Cassaignon., C. Chanéac., F. Vilain., E. Tronc., and J. P. Jolivet., *"Size tailoring of TiO_2 anatase nanoparticles in aqueous medium and synthesis of nanocomposites. Characterization by Raman spectroscopy"*, Journal of Materials Chemistry 13, 877 (2003).

[8] S. D. Mo and W. Y. Ching, *"Electronic and optical properties of three phases of titanium dioxide: Rutile, anatase, and brookite"*, Physical review B, 51 (1), (1995).

[9] M. Landmann., E. Rauls and W. G. Schmidt, *"The electronic structure and optical response of rutile, anatase and brookite TiO_2"*, J. Phys.: Condens. Matter 24 (19), (2012) 195503.

[10] B. Thomas, *"Des nanotitanates de soduim aux dioxydes de titane : électrode négative à base de TiO_2 (B) nanométrique pour accumulateur lithium ion"*, Thèse de Doctorat, Université de Nantes, France (2009).

[11] S. Pardis, *"Synthèse de nanoparticules d'oxyde de titane par pyrolyse laser : étude des propriétés optiques et de la structure électronique"*, Thèse de Doctorat, Université Paris Sud XI, France (2001).

[12] B. S. Richards, *"Novel uses of titanuim dioxide for silicon solar cells"*, Thèse de Doctorat, Université de New South Wales Sydney2052, Australie, (2002).

[13] J. Schneider., M. Matsuoka., M. Takeuchi., J. Zhang., Y. Horiuchi., M. Anpo., and D. W. Bahnemann, *"Understanding TiO_2 Photocatalysis: Mechanisms and Materials"*, Chem. Rev. 114 (19), (2014) 9919-9986.

[14] M. A. Fox and M. T. Dulay, *"Heterogeneous Photocatalysis"*, Chem. Rev. 93 (1) (1993), 341-357.

[15] H. Cheng., J. Ma., Z. Zhao., and L. Qi, *"Hydrothermal preparation of uniform nanosize rutile and anatase particles"*, Chem. Mater. 7(4), (1995) 663-671.

[16] S. R. Dhage., R. Pasricha, and V. Ravi, *"Synthesis of ultrafine TiO_2 by citrate gel method"*, Materials Research Bulletin 38 (11-12), (2003) 1623-1628.

[17] M. E. Kurtoglu., T. Longenbach., K. Sohlberg., and Y. Gogotsi, *"Strong coupling of Cr and N in Cr–N-doped TiO_2 and its effect on photocatalytic activity"*, The Journal of Physical Chemistry C, 115(35), (2011) 17392-17399.

[18] T. Luttrell., S. Halpegamage., J. Tao., A. Kramer., E. Sutter., and M. Batzill, *"Why is anatase a better photocatalyst than rutile? -Model studies on epitaxial TiO_2 films"*, Scientific reports 4 (1), (2014) 1-8.

[19] D. Riassetto, *"Fonctionnalisation de surface par chimie douce en solution liquide Nanoparticules métallique (platine, or, argent) et revêtements TiO_2"*, Thèse de Doctorat, Institut Polytechnique de Grenoble, France, (2009).

[20] U. Diebold, *"The surface science of titanium dioxide"*, *Surface science reports* 48 (5-8), (2003): 53-229.

[21] Y. Cao., T. He., Y. Chen and Y. Cao, *"Fabrication of rutile TiO_2−Sn/anatase TiO_2−N heterostructure and its application in visible-light photocatalysis"*, *The Journal of Physical Chemistry C* 114 (8), (2010): 3627-3633.

[22] N. Sekar and V. Y. Gehlot, *"Metal complex dyes for dye-sensitized solar cells: Recent developments"*, Resonance, 15(9), (2010) 819-831.

[23] S. K. Singh and S. Basu, *"Characterisation of conducting SnO_2 layers deposited by modified spray pyrolysis technique"*, Mater. Chem. Phys. 20 (4-5), (1988) 381 – 396.

[24] A. H. Battez., R. Gonzalez., J. L. Viesca., J. E. Fernandez, J. D. Fernandez., A. Machado., R. Chou and J. Riba, *"CuO, ZrO_2 and ZnO nanoparticles as antiwear additive in oil lubricants"*, Wear 265(3-4), (2008) 422-428.

[25] S. Menakh, *"Contribution à l'étude des propriétés de films ZnO"*, Mémoire de magister en physique de Semiconducteurs, Université Mentouri, Constantine, Algerie, (2011).

[26] S. Shenlei, *"Exiton related optical properties of ZnO"*, PhD thesis, University of Hong Kong, (2006).

[27] T. Steiner, *"Semiconductor Nanostructures for Optoelectronic Applications"*, Artech House, Inc. Boston. London, (2004).

[28] F. Oba., S. R. Nishitani., S. Isotani., H. Adachi and I. Tanaka, *"Energetics of native defects in ZnO"*, J. Appl. Phys. 90 (2), (2001) 824-828.

[29] R. Eason, *"Pulsed Laser Deposition of Thin Films"*, Wiley-Interscience, New York, USA, (2007).

[30] V. A. Johnson and K. Lark-Horovitz, *"Theory of thermoelectric power in semiconductors with applications to germanium"*, Physical Review, 92 (2), (1953) 226.

[31] A. Moustaghfir, *"Élaboration et caractérisation de couches minces d'oxyde de zinc. Application à la photoprotection du polycarbonate"*, Doctorat thesis, Université Blaise Pascal, France, (2004).

[32] A. van Dijken., E. A. Meulenkamp., D. Vanmaekelbergh, and A. Meijerink, *"The kinetics of the radiative and nonradiative processes in nanocrystalline ZnO particles upon photoexcitation"*, J. Phys. Chem. B, 104 (8), (2000) 1715-1723.

[33] A. Kołodziejczak-Radzimska and T. Jesionowski, *"Zinc Oxide-From Synthesis to Application: A Review"*, Materials, 7(4), (2014), 2833-2881.

[34] C. M. Ghimbeu., J. Schoonman., M. Lumbreras and M. Siadat, *"Electrostatic spray deposited zinc oxide films for gas sensor applications"*, Applied Surface Science, 253(18), (2007) 7483-7489.

[35] C. Wang., L. Yin, L. Zhang, D. Xiang and R. Gao, *"Metal oxide gas sensors: sensitivity and influencing factors"*, Sensors, 10(3), (2010) 2088-2106.

[36] Y. Min, *"Properties and sensor performance of Zinc Oxide Thin Films"*, PhD thesis, Massachusetts Institute of Technology, USA, (2003).

[37] A. B. F, Martinson., J. E. McGarrah., M. O. Parpia, and J. T. Hupp. *"Dynamics of charge transport and recombination in ZnO nanorod array dye-sensitized solar cells"*, Physical Chemistry Chemical Physics, 8(40), (2006) 4655-4659.

Chapter II

Thin films deposition techniques and characterization tools

II. 1. Introduction

Thin-film technology is simultaneously one of the oldest arts and one of the newest sciences. Involvement with thin films dates to the metal ages of antiquity. Consider the ancient craft of gold beating, which has been practiced continuously for at least four millennia. Gold's great malleability enables it to be hammered into leaf of extraordinary thinness while its beauty and resistance to chemical degradation have earmarked its use for durable ornamentation and protection purposes.

Over the past two decades, the development of materials in the form of thin films has contributed to an explosion of performance of professional electronics, including reducing the cost of components for mass production. However, since the invention of the transistor in 1947, has seen the integration of several thousands of components (such as semiconductor components). Thereby, to trivialize devices like calculators and personal computers, which provide computing capacity and memory far superior to the first computers [1].

II. 2. What is a thin film?

Any solid or liquid object with one of its dimensions very much less than that of the other two may be called a ‘thin film’. Thin film devices would typically be about 5 to 50 μm thick in contrast to bulk devices, which are about 50 to 250 μm thick [2]. If the growth is atom by atom or molecule by molecule it is called thin film and if the growth is grain by grain it is thick film.

The limit between "thin" and "thick" films cannot generally be defined, although literature sometimes gives an arbitrary value of 1 μm, basically, a film can be considered as "thin" when its properties are significantly different from the bulk.

Thin films can be prepared from a nearly infinite range of compositions such as conductive materials, insulators, refractory (oxides, nitrides, carbides) and polymers among others. The structure of the deposited films can be mono or multilayer. Which explain the wide several of their applications: microelectronics, optics, chemistry and mechanics…etc.

The formation of thin film is carried out by a combination of coalescence, nucleation and growth process. Firstly, the absorptive species are not in thermodynamic balance with the substrate, and thus move on its surface until their temperature reach to substrate temperature. During these displacements, and when they arrive in favorable sites (crystalline defects, impurities…) which are called sites of nucleation they creating germs which will be growth to forming the film.

II. 3. Thin films preparation Techniques

Generally, any thin film deposition follows the sequential steps: a source material is converted into the vapor form (atomic/molecular/ionic species) from the condensed phase (solid or liquid), which is transported to the substrate and then it is allowed to condense on the substrate surface to form the solid film [2]. Depending on how the atoms/molecules/ions or clusters of species are created for the condensation process, the deposition techniques are broadly classified into two categories: physical methods and chemical methods.

Chemical bath deposition, chemical vapor deposition, and spray pyrolysis are examples of chemical method of thin film deposition. Thermal evaporation, e-beam evaporation, RF and DC sputtering and pulsed laser deposition (PLD) are examples of physical methods of thin film preparation. The following sections discuss the methodology and experimental setup used in various thin film deposition techniques.

II. 3. 1. Physical vapor deposition (PVD)

The various techniques used in this method are evaporation, sputtering, pulsed laser deposition and molecular beam epitaxy.

II. 3. 1. 1. Thermal evaporation by resistive heating

Thermal evaporation is the most widely used technique for the preparation of thin films of metals, alloys, and also many compounds, as it is very simple and convenient. Here the only requirement is to have a vacuum environment in which sufficient amount of heat is given to the evaporants to attain the vapor pressure necessary for the evaporation. The evaporated material is allowed to condense on a substrate kept at a suitable temperature. When evaporation is made in vacuum, the evaporation temperature will be considerably lowered and the formation of the oxides and incorporation of impurities in the growing layer will be reduced. Evaporation is normally done at a pressure of 10^{-5} Torr. At this pressure a straight-line path for most of the emitted vapor atoms is ensured for a substrate to source distance of nearly 10 to 50 cm. The characteristics and quality of the deposited film will depend on the substrate temperature, rate of deposition, ambient pressure, etc. and the uniformity of the film depends on the geometry of the evaporation source and its distance from the source. The deposition by thermal evaporation is simple, convenient and is widely use [2].

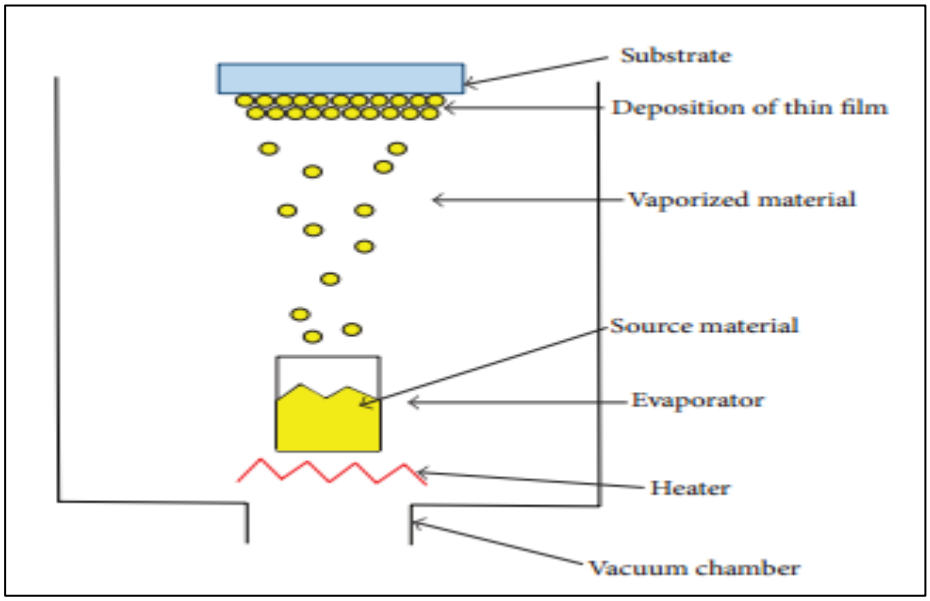

Figure II. 1. Schematic of Thermal evaporation by resistive heating [3].

II. 3. 1. 2. Electron beam evaporation

In electron beam evaporation (EBE) a stream of electrons is accelerated through fields of typically 5–10kV and focused onto the surface of the material for evaporation. The electrons lose their energy very rapidly upon striking the surface and the material melts at the surface and evaporates. That is, the surface is directly heated by impinging electrons, in contrast to conventional heating modes. Direct heating allows the evaporation of materials from water-cooled crucibles. Such water-cooled crucibles are necessary for evaporating reactive and in particular reactive refractory materials to avoid almost completely the reactions with crucible walls. This allows the preparation of high purity films because crucible materials or their reaction products are practically excluded from evaporation.

Electron beam guns can be classified into thermionic and plasma electron categories. In the former type the electrons are generated thermionically from heated refractory metal filaments, rods or disks. In the latter type, the electron beams are extracted from plasma confined in a small space [2].

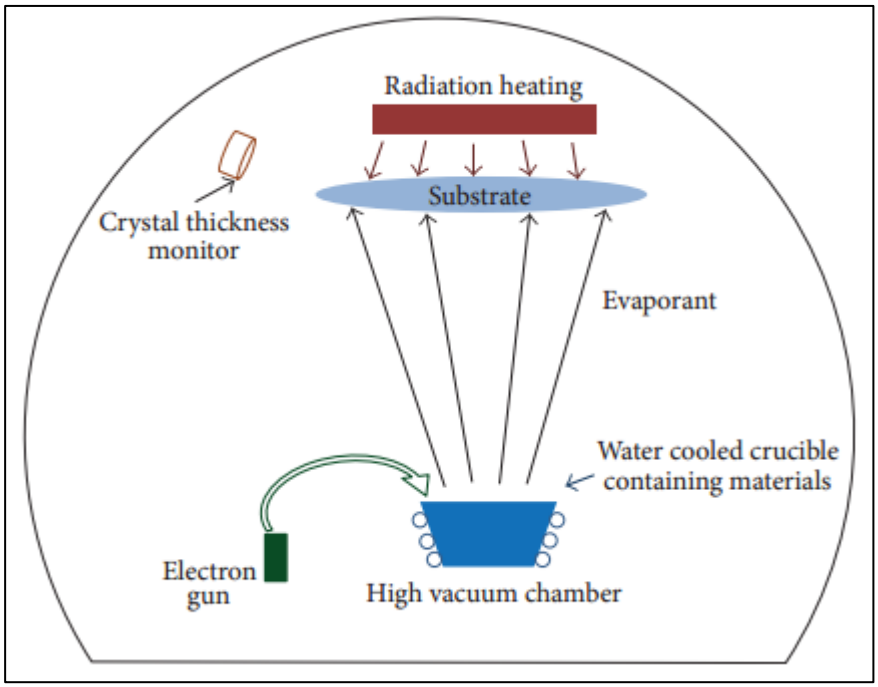

Figure II.2. General diagram of Electron Beam Evaporator [4].

II. 3. 1. 3. Sputtering

Sputtering is one of the most versatile techniques used for the deposition of transparent conductors when device quality films are required. Sputtering process produces films with better controlled composition, provides films with greater adhesion and homogeneity and permits better control of film thickness. The sputtering process involves the creation of gas plasma usually an inert gas such as argon by applying voltage between a cathode and anode. The target holder is used as cathode and the anode is the substrate holder. Source material is subjected to intense bombardment by ions. By momentum transfer, particles are ejected from the surface of the cathode and they diffuse away from it, depositing a thin film onto a substrate. Sputtering is normally performed at a pressure of 10^{-2} –10^{-3} Torr.

Normally there are two modes of powering the sputtering system; DC and RF biasing. In DC sputtering system a direct voltage is applied between the cathode and the anode. This method is restricted for conducting materials only. RF sputtering is suitable for both conducting and non-conducting materials; a high frequency generator (13.56 MHz) is connected between the electrodes of the system. Magnetron sputtering is a process in which the sputtering source uses magnetic field at the sputtering target surface. Magnetron sputtering is particularly useful when high deposition rates and low substrate temperatures are required [2].

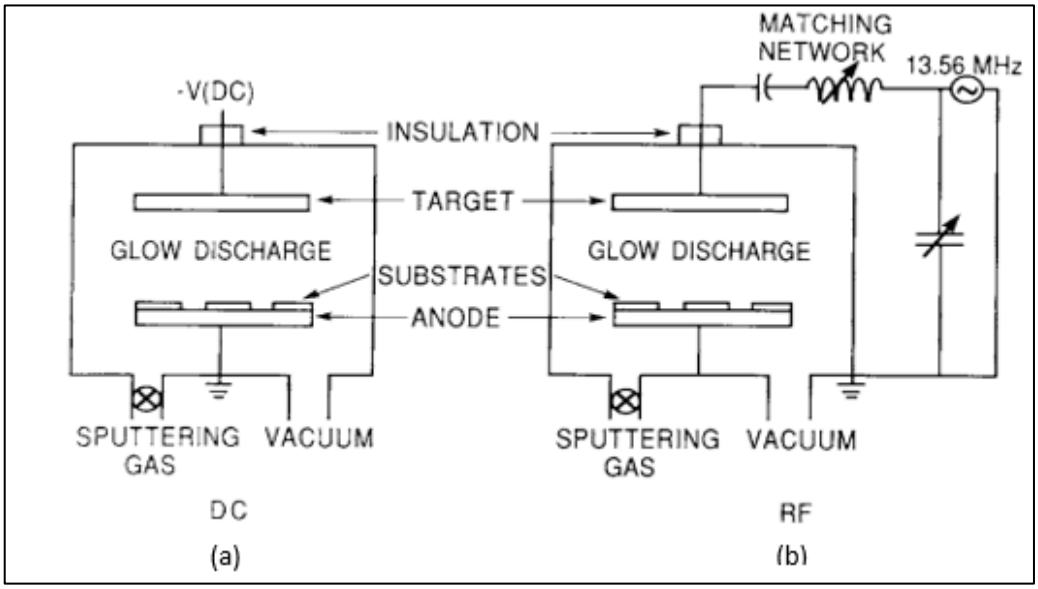

Figure II. 3. Schematics of simplified sputtering systems: (a) DC, (b) RF [1].

II. 3. 1. 4. Pulsed laser deposition (PLD)

The principle of the thin layers deposit by laser ablation (Pulsed Laser Deposition) is relatively simple. An impulse laser beam (more often nanosecond) is focused on a massive target, placed in one enclosure ultra-high vacuum. Under certain conditions of interaction, a quantity of matter target is ejected, and can be collected on a substrate placed in opposite. The nature and the quality of the deposit depend on many parameters (energy of the laser, nature and pressure of residual gas in the enclosure, temperature of the substrate...). In all the cases, it is necessary to control the transport of the species of the target until the substrate. Some characteristics return the process of deposit indeed by laser ablation particularly gravitational:

- The stoechiometric transfer of the matter of the target towards substrate. That facilitates the multi-element material deposit such as for example the superconductors at high temperature criticize.
- The purity of the targets is the only parameter influencing the purity of the deposits (deposit under ultra-high vacuum or in residual atmosphere).
- The choice of the type of material which one can deposit is vast: it is limited only by the absorption of material to the wavelength of the laser.

In the case of ablation by a laser of duration of impulse femto second (10^{-15} s), from the much higher densities of power can be obtained. The interaction laser-matter is then very different from that met in the case of a laser of duration of impulse nanosecond. The plume plasma is made up partly of species of strong kinetic energy (of the order of the KeV). The layers thus obtained have lower levels of constraint thus supporting adherence.

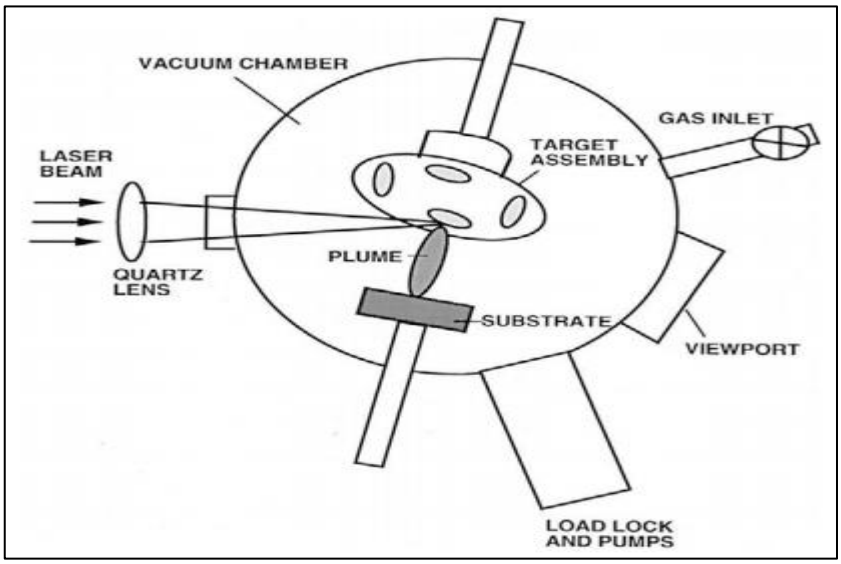

Figure II. 4. General diagram of PLD [1].

II. 3. 1. 5. Molecular Beam Epitaxy (MBE)

Selected elements, e.g. Ga, As, Al, etc. are heated in vacuum furnaces called effusion cells. Evaporated atoms and molecules leave the cells in collimated beams and impinge on a heated surface of a monocrystalline wafer. Here they enter different processes (physical adsorption, chemisorption, migration), undergo transformation (dissociation, association, etc.) and at last form a monocrystalline lattice. Molecular beams can be interrupted by shutters placed in front of the cell orifices. By this way it is possible to change composition and properties of grown layers. Some cells usually contain dopant elements (Si and Be for n- or p-doping in GaAs) which control the type of electrical conductivity. Growth process is realized in ultra-high vacuum chamber with ultimate pressure in the order of 10-11 mbar. The chamber is equipped with a number of effusion cells, with manipulator for sample heating (0–1000 C°) and azimuthal rotation, with an electron gun and screen for RHEED (reflection high-energy electron diffraction) and other accessories. Inner chamber walls are surrounded by cryopannels, which are cooled by liquid nitrogen (-197 C°) during the growth).

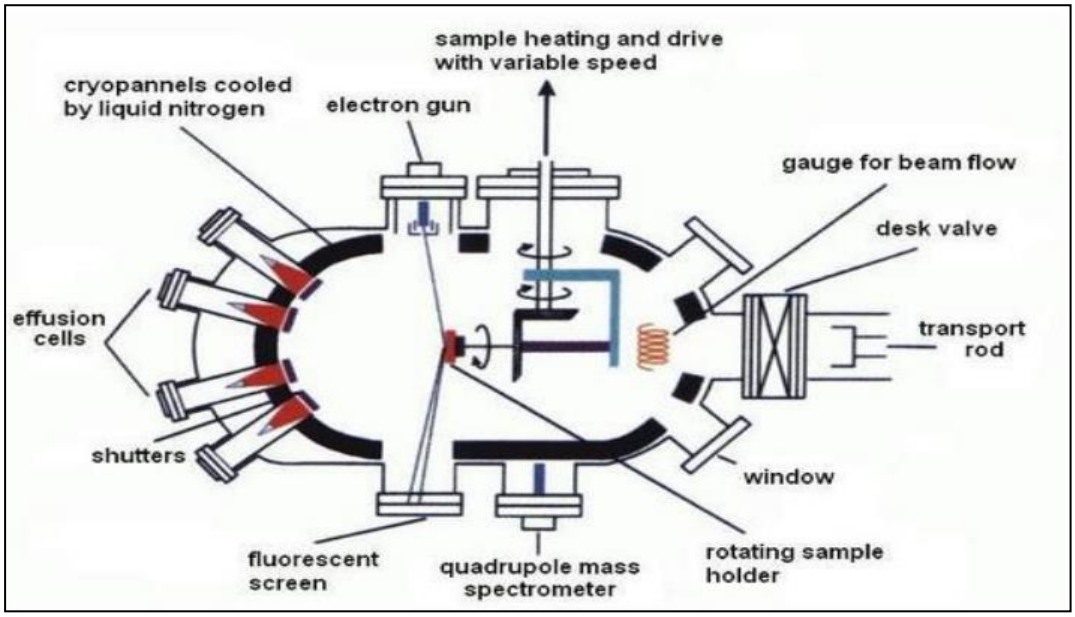

Figure II. 5. The MBE growth chamber design, the sample is fixed in the chamber center on a rotating holder [5].

II. 3. 2. Chemical vapor deposition

Methods of film formation by purely chemical processes in the gas or vapor phases include chemical vapor deposition (CVD) and thermal oxidation. CVD is a materials synthesis process whereby constituents of the vapor phase react chemically near or on a substrate surface to form a solid product. The deposition technology has become one of the most important means of creating thin films and coating of a very large variety of materials essential to advanced technology particularly solid-state electronics where some of the most sophisticated purity and composition must be met. The main feature of CVD is its versatility for synthesizing both simple and complex compounds with relative ease at generally low temperatures.

Both chemical composition and physical structure can be tailored by control of the reaction chemistry and deposition conditions. Fundamental principles of CVD encompass an interdisciplinary range of gas phase reaction chemistry, thermodynamics, kinetics, transport mechanisms, film growth phenomena and reactor engineering.

Chemical reaction types basic to CVD include pyrolysis (thermal decomposition), oxidation, reduction, hydrolysis, nitride and carbide formation, synthesis reaction, disproportionation and chemical transport. A sequence of several reaction types may be involved in more complex situations to create a particular end product. Deposition variables such as temperature, pressure, input concentrations, gas flow rates and reactor geometry and operating principle determine the deposition rate and the properties of the deposit film.

Any vapor deposition technique is based on the principles of mass transfer from one source to another. Macroscopically following three fundamental steps play critical role in the growth of a film:

- Transfer of the precursor to the gas phase.
- Transport of the gas phase to the substrate.
- Deposition onto substrate and film growth.

These three steps are either separated in space and time or superimpose with each other, depending on process requirements.

Most chemical reactions in CVD are thermodynamically endothermic and/or have a kinetic energy of activation associated with them. Generally, this is an advantage since the reactions can be controlled by regulating the energy input. However, it does mean that energy has to be supplied to the reacting system, and traditionally CVD processes have been initiated and controlled by the input of thermal energy to the substrate. Based on the energy input, three different methods of energy input in CVD processes are practiced:

- Thermal CVD (generally from 800-2000°C).
- Plasma CVD: In plasma CVD, also known as plasma enhanced CVD (PECVD) or plasma assisted CVD (PACVD), the reaction is activated by plasma and the deposition temperature is substantially lower.
- Laser and photo CVD: two methods based on photo activation have recently been developed: A laser produces a coherent monochromatic high energy beam of photons, which can be used effectively to activate a CVD reaction [6].

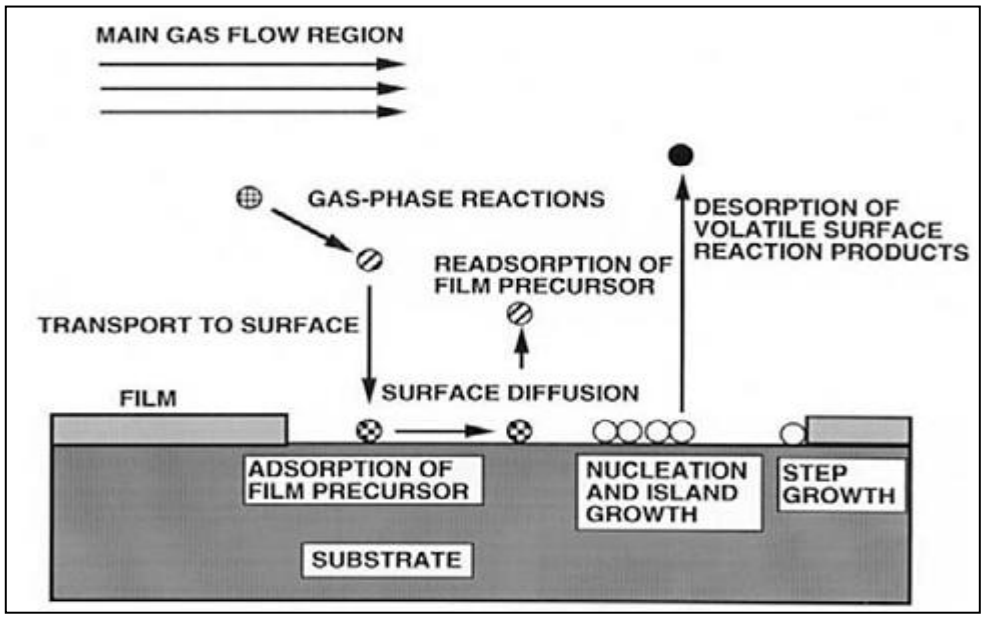

Figure II. 6. Sequence of gas transport and reaction processes contributing to CVD film growth [1].

II. 3. 3. Spray Pyrolysis technique

The spray pyrolysis is a cheap and simple technique based on chemical vapor deposition process (CVD). In this technique, the precursor of the material to be deposited is in solution and sprayed onto a heated substrate using air as carrier gas [7]. In the spray pyrolysis technique, there are many deposition variables (the parameters of the process), such as substrate temperature, gas and solution flow rates, composition and concentration of the precursor in the starting solution, deposition time, the substrate-nozzle distance, etc. Some of these parameters are mutually dependent on each other. However, to study the effects of any one of these, the remaining others must be kept constant [9].

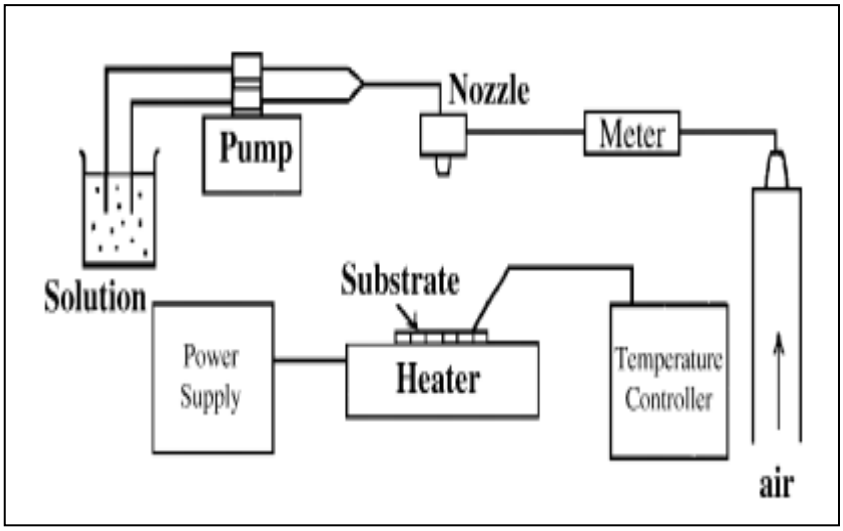

Figure II. 7. Schematic diagram of the spraying system [7].

II. 4. Characterization tools of thin films

The optimization of the preparation conditions is the main task in order to get device quality films. This has to be carried out on the basis of detailed structural, compositional, morphological, optical and electrical properties of the films obtained at different growth conditions. In the following sections the techniques used for the film characterizations are discussed briefly.

II. 4. 1. Structural characterization with X-ray diffraction

X-ray diffraction (XRD) studies were carried out to study the crystallographic properties of the thin films prepared. A given substance always produces a characteristic x-ray diffraction pattern whether that substance is present in the pure state or as one constituent of a mixture of substances. This fact is the basis for the diffraction method of chemical analysis. Diffraction analysis is useful whenever it is necessary to know the state of chemical combination of the elements involved or the particular phase in which they are present. Compared with ordinary chemical analysis the diffraction method has the advantage that it is much faster, requires only very small sample and is nondestructive.

The basic law involved in the diffraction method of structural analysis is the Bragg's law. When monochromatic x-rays impinge upon the atoms in a crystal lattice, each atom acts as a source of scattering. The crystal lattice acts as series of parallel reflecting planes. The intensity of the reflected beam at certain angles will be maximum when the path difference between two reflected waves from two different planes is an integral multiple of λ. This condition is called Bragg's law and is given by the relation:

$$2d\ sin\,\theta = n\lambda \qquad \text{(II.1)}$$

Where: n is the order of diffraction, λ is the wavelength of the x-rays, d is the spacing between consecutive parallel planes and θ is the glancing angle (or the complement of the angle of incidence).

X-ray diffraction studies give a whole range of information about the crystal structure, orientation, average crystalline size and stress in the films. Experimentally obtained diffraction patterns of the sample are compared with the standard powder diffraction files published by the International Centre for Diffraction Data (ICDD) [2].

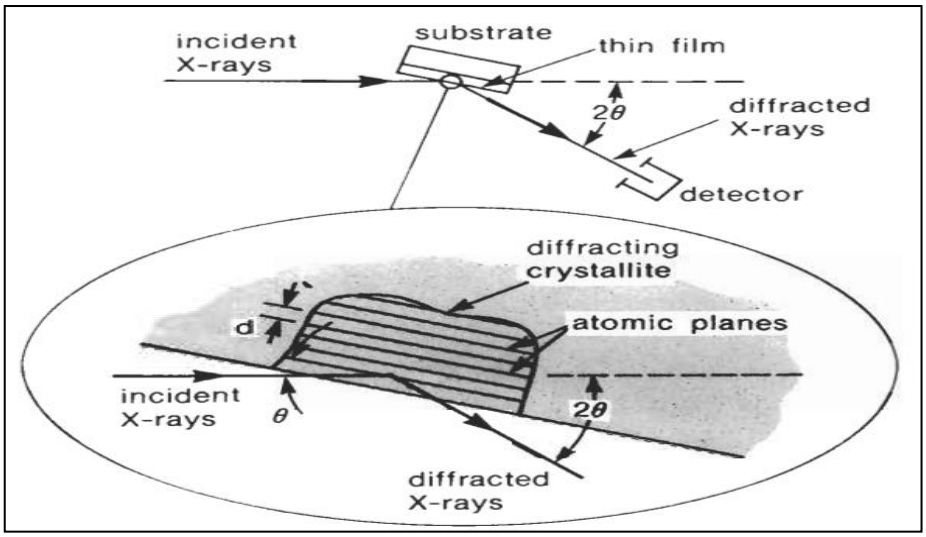

Figure II. 8. Basic features of a typical XRD experiment. [10]

II. 4. 1. 1. Determination of the grains size

The average grain size of the film can be calculated using the Scherrer's formula:

$$D = \frac{0.9\lambda}{\beta cos\theta} \qquad \text{(II.2)}$$

Where, λ is the wavelength of the x-ray and β is the full width at half maximum intensity in radians [2].

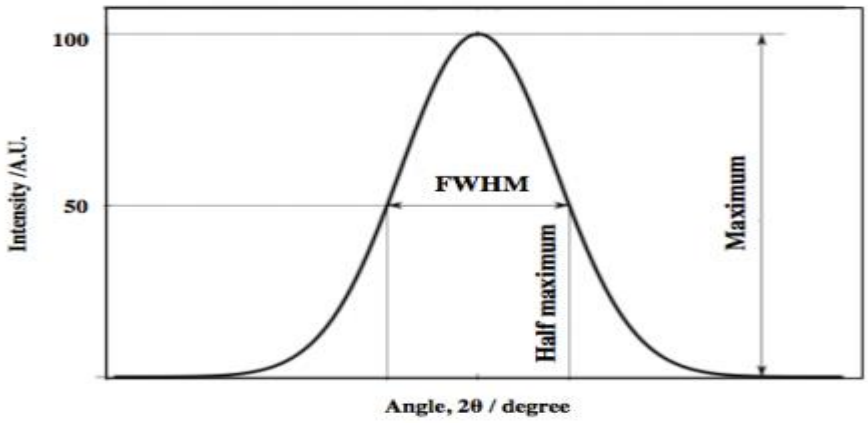

Figure II. 9. Illustrate the peak widths *FWHM* ($\Delta\theta = \beta$) [8].

II. 4. 1. 2. Determination of the interreticular distances and the cell parameters

The lattice parameter values for different crystallographic systems can be calculated from the following equations using the *(hkl)* parameters and the interplanar spacing *d* [2].

Cubic system: $$\frac{1}{d^2} = \frac{h^2+k^2+l^2}{a^2} \qquad \text{(II.3)}$$

Tetragonal system: $$\frac{1}{d^2} = \frac{h^2+k^2}{a^2} + \frac{l^2}{c^2} \qquad \text{(II.4)}$$

Hexagonal system: $$\frac{1}{d^2} = \frac{4}{3}\left(\frac{h^2+hk+k^2}{a^2}\right) + \frac{l^2}{c^2} \qquad \text{(II.5)}$$

II. 4. 2. Scanning Electron Microscope (SEM)

The Scanning Electron Microscope (SEM) is a microscope that uses electrons rather than light to form an image. There are many advantages for using the SEM instead of an optical microscope. The SEM has a large depth of field, which allows a large amount of the sample to be in focus at one time. The SEM also produces images of high resolution, which means that closely spaced features can be examined at a high magnification. Preparation of the samples is relatively easy since most SEMs only requires that sample should be conductive. The combination of higher magnification, larger depth of focus, greater resolution, and ease of sample observation makes the SEM one of the most heavily used instruments in current research and development. The electron beam comes from a filament, made of various types of materials. The most common is the tungsten hairpin gun. This filament is a loop of tungsten that functions as the cathode. A voltage is applied to the loop, causing it to heat up. The anode, which is positive with respect to the filament, forms powerful attractive forces for electrons. This causes electrons to accelerate toward the anode. The anode is arranged, as an orifice through which electrons would pass down to the column where the sample is held. Other examples of filaments are Lanthanum Hexaboride filaments and field emission guns.

The streams of electrons that are attracted through the anode are made to pass through a condenser lens, and are focused to very fine point on the sample by the objective lens figure II. 10. The electron beam hits the sample, producing secondary electrons from the sample. These electrons are collected by a secondary detector or a backscatter detector, converted to a voltage, and amplified. The amplified voltage is applied to the grid of the CRT (Cathode Ray Tube) that causes the intensity of the spot of light to change. The image consists of thousands of spots of varying intensity on the face of a CRT that correspond to the topography of the sample [11].

Figure II. 11 shows the interaction of electrons with matter in order to make sure we have the information from the sample surface only, when a SEM is used, the column must always be at a vacuum. Otherwise there are chances for contamination of the sample and also the electrons beam would induce ionization in any background gas that would affect the measurement being made on the sample.

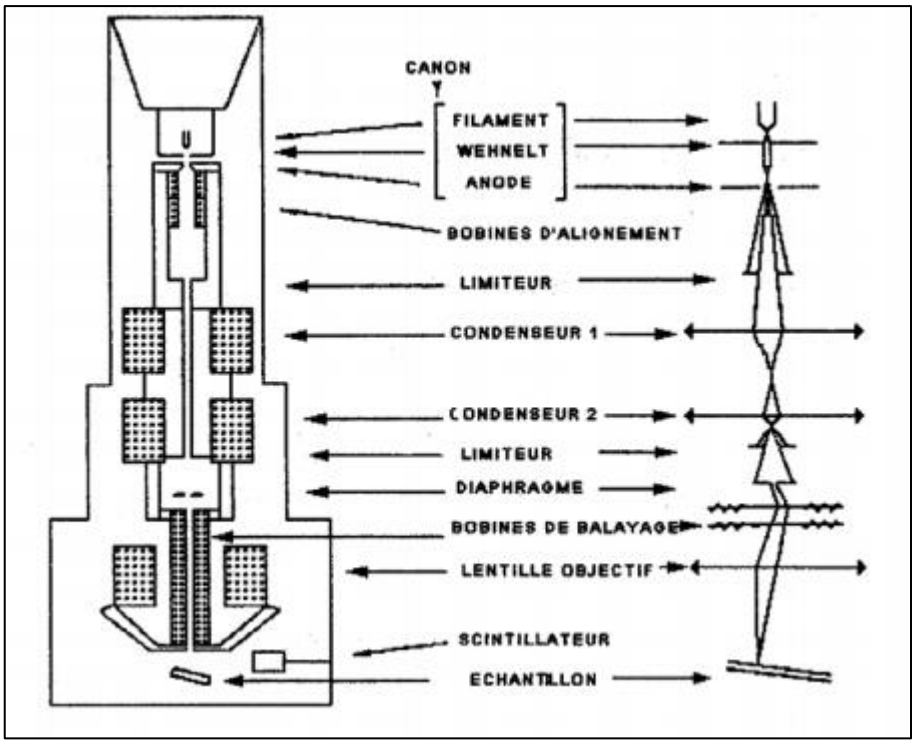

Figure II. 10. Simplified schematic of SEM [12].

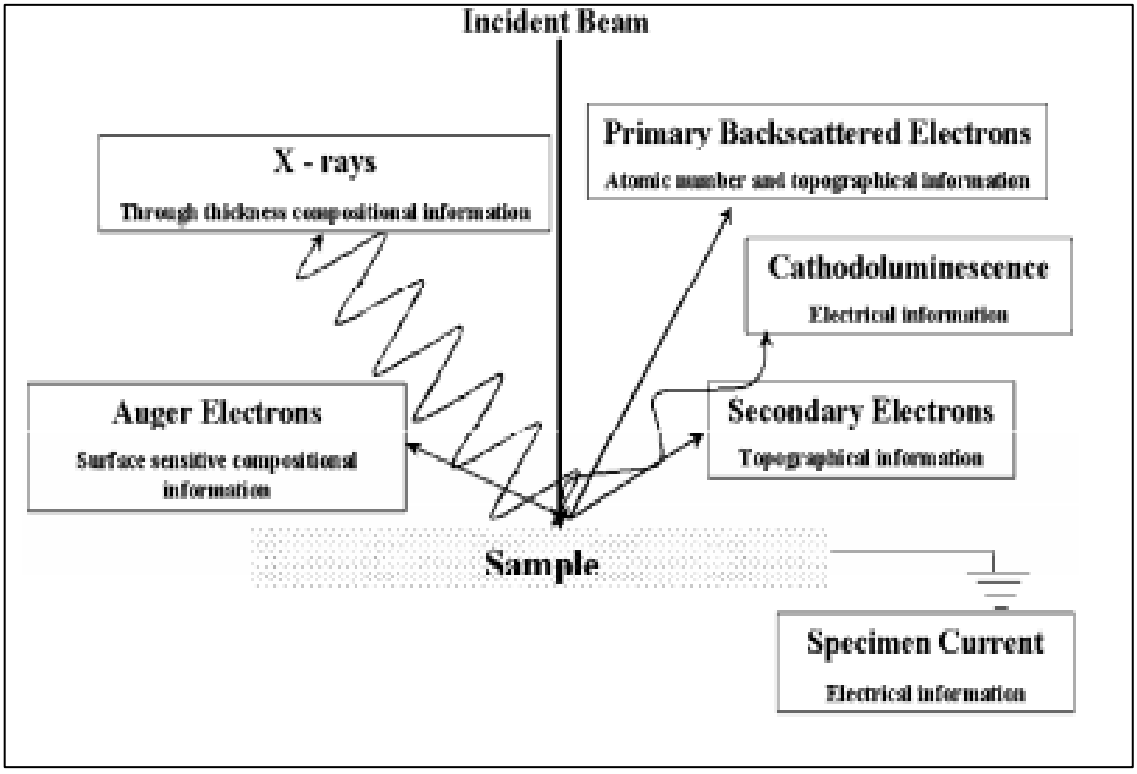

Figure II. 11. In SEM set up, interaction of electron with the sample produces both photons and electrons [11].

II. 4. 3. Fourier Transform Infrared (FTIR) and Raman spectroscopy

FTIR is one of the inexpensive techniques that can provide information about the chemical bonding in a material, it is particularly useful for the non-destructive analysis of solids and thin films. In this technique a broad band source of IR radiation is reflected from the sample (or transmitted, for thin samples). The wavelengths at which absorption occurs are identified by measuring the change in intensity of the light after reflection (transmission) as a function of wavelength. These absorption wavelengths represent excitations of vibrations of the chemical bonds and are specific to the type of bond and the group of atoms involved in the vibration.

Raman spectroscopy is a spectroscopic technique based on inelastic scattering of monochromatic light, usually from a laser source. Inelastic scattering means that the frequency of photons in monochromatic light changes upon interaction with a sample. Photons of the laser light are absorbed by the sample and then reemitted. Frequency of the reemitted photons is shifted up or down in comparison with original monochromatic frequency, which is called the Raman effect. This shift provides information about vibrational, rotational and other low frequency transitions in molecules (to determine the crystalline phases). Raman spectroscopy can be used to study solid, liquid and gaseous samples.

A Raman system typically consists of four major components: excitation source (Laser), sample illumination system and light collection optics, wavelength selector (Filter or Spectrophotometer) and detector (Photodiode array, CCD or PMT). A sample is normally illuminated with a laser beam in the ultraviolet (UV), visible (Vis) or near infrared (NIR) range. Scattered light is collected with a lens and is sent through interference filter or spectrophotometer to obtain Raman spectrum of a sample.

II. 4. 4. Photoluminescence spectroscopy

Photoluminescence spectroscopy is a contactless, non-destructive method of probing the electronic structure of materials. Light is directed onto a sample, where it is absorbed and imparts excess energy into the material in a process called photo-excitation. One way this excess energy can be dissipated by the sample is through the emission of light, or luminescence. In the case of photo-excitation, this luminescence is called photoluminescence. Photo-excitation causes electrons within a material to move into permissible excited states. When these electrons return to their equilibrium states, the excess energy is released and may include the emission of light (a radiative process) or may not (a nonradiative process). The energy of the emitted light (photoluminescence) relates to the difference in energy levels between the two

electron states involved in the transition between the excited state and the equilibrium state. The quantity of the emitted light is related to the relative contribution of the radiative process.

Typically, the emitted luminescence is collected by a lens and passed through an optical spectrometer onto a photodetector. The spectral distribution and time dependence of the emission are related to electronic transition probabilities within the sample, and can be used to provide qualitative and, sometimes, quantitative information about chemical composition, structure (bonding, disorder, interfaces, quantum wells), defects (efficiency of charge carrier trapping), impurities and kinetic processes.

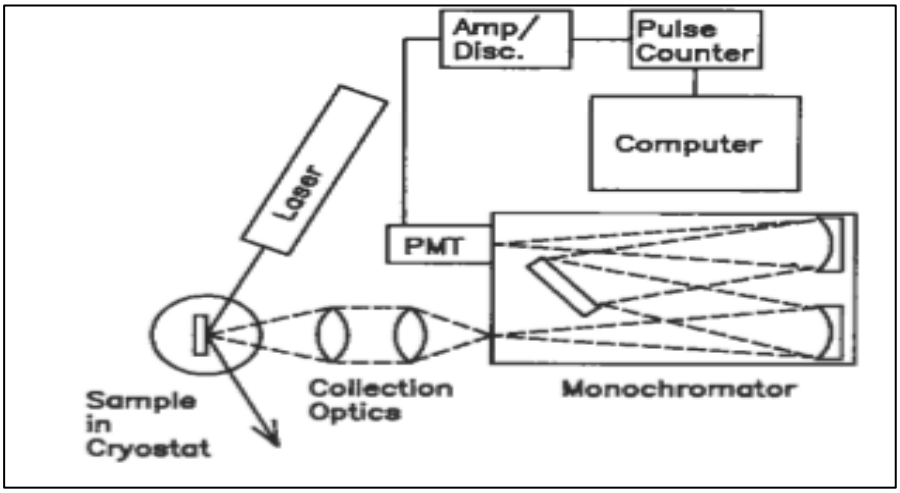

Figure II. 12. Schematic layout of a high-sensitivity PL system incorporating a laser and photon-counting electronics [10].

II. 4. 5. Electrical characterization with four-point probe method

In order to eliminate or at least minimize the contact contribution to the measured resistance value, techniques based on separate current injection and voltage drop measurements have been developed. Firstly, the two-probe technique can be used. This measurement is very simple, but it is affected by several parameters: lateral contact geometry, probe spacing, and minority carrier injection near the lateral contacts. The main disadvantage of this technique is the need for lateral contacts. This requirement is overcome with the four-point probe technique, where two probes are used for current injection and the other two probes are used to measure the voltage drop. The more usual probe geometry configuration is when the four probes are placed in a line, as shown in figure II.13. The voltage at probe 2, V_2, induced by the current flowing from probe 1 to probe 4 is given by:

$$V_2 = \frac{\rho I}{2\pi} \cdot \left(\frac{1}{s_1} - \frac{1}{s_2 + s_3}\right) \quad \text{(II.6)}$$

The voltage at probe 3 is: $V_3 = \frac{\rho I}{2\pi} \cdot \left(\frac{1}{s_1 + s_2} - \frac{1}{s_3}\right)$ (II.7)

Then, by measuring $V = V_2 - V_3$, the voltage drops between probes 2 and 3, and the current I through probes 1 and 4, the resistivity can be determined using (II.6) and (II.7) as:

$$\rho = \frac{2\pi V / I}{\left(\frac{1}{s_1} + \frac{1}{s_2} - \frac{1}{s_2 + s_3} - \frac{1}{s_1 + s_2}\right)} \quad \text{(II.8)}$$

Thus, a direct measurement of the resistivity can be made using a high-impedance voltmeter and a current source. When the probe spacings are equal ($s_1 = s_2 = s_3 = s$), which is the most practical case, then (II.8) becomes:

$$\rho = 2\pi s \cdot \frac{V}{I} \quad \text{(II.9)}$$

Equations (II.8) and (II.9) are valid only for semi-infinite samples; that is, when both the thickness t and the sample surface are very large ($\rightarrow \infty$), and the probes' locations must be far from any boundary. Because these relations can be applied only to large ingots, then in many cases a correction factor f must be introduced in order to take into account the finite thickness and surface of the sample and its boundary effects. Further, for epitaxial layers, f must also consider the nature of the substrate – whether it is a conductor or an insulator. Thus, (II.9) becomes:

$$\rho = 2\pi s \cdot \frac{V}{I} \cdot f \quad \text{(II.10)}$$

For a thin semiconductor wafer or thin semiconducting layer deposited on an insulating substrate, and for the condition $t < s/2$, which represents most practical cases because the probe spacing s is usually on the order of a millimeter, then the correction factor due to the thickness is:

$$f = \frac{(t/s)}{2ln2} \quad \text{(II.11)}$$

so that: $$\rho = 4.532\, t\, \frac{V}{I} \quad \text{(II.12)}$$

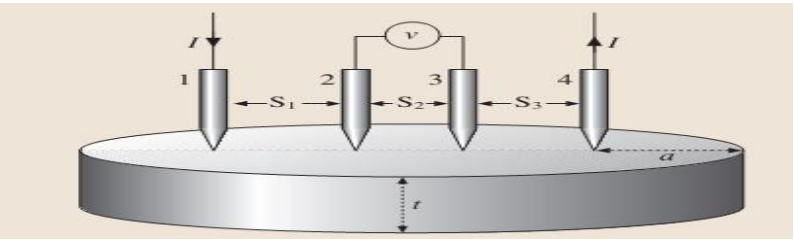

Figure II. 13. Linear four-point probe configuration. The sample thickness is t and a is the distance from the edge or boundary of the sample [13].

II. 4. 6. Optical measures through spectroscopy (UV-VIS)

This technique rests on the knowledge of the distances between interference rings in the spectra of transmission in the visible and the near infra-red. One uses a recording spectrophotometer with double beams, of which its principle of operation is represented on figure (II.14).

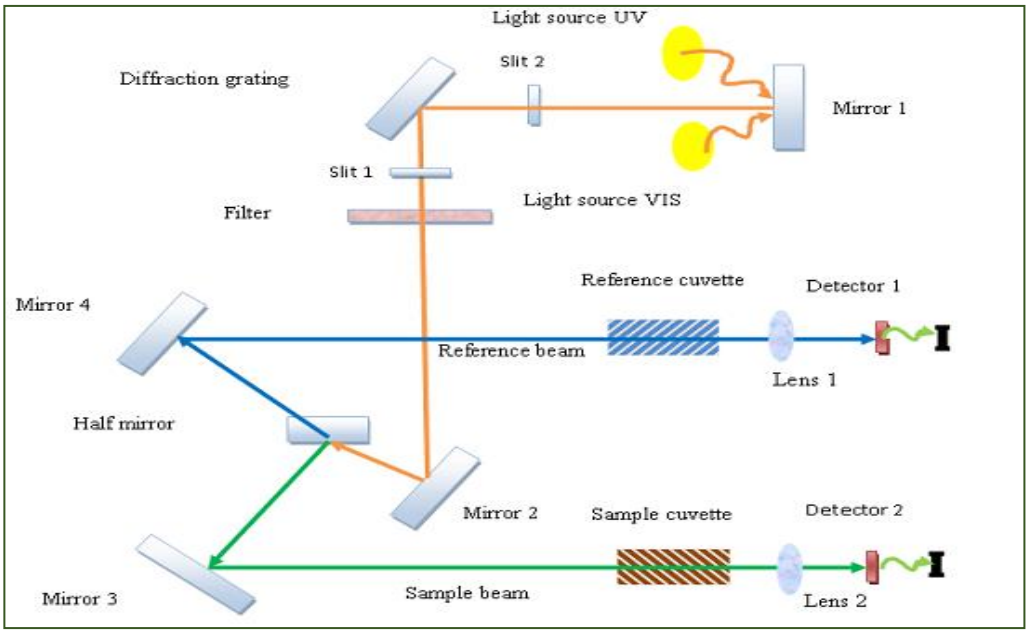

Figure II.14. The principle of operation of UV-visible [14].

The obtained spectra give the variation of transmittance expressed as a percentage $T(\%)$ according to their wavelength $\lambda\ (nm)$. Thanks to the interferences, one can determine the following parameters: thickness of the film, optical gap, absorption coefficient and the refraction index which can be calculated using the following relations:

II. 4. 6. 1. The thickness of the film d (Swanepoel method) [15]:

$$d = \lambda_1\lambda_2/2(\lambda_2 n_1 - \lambda_1 n_2) \qquad \text{(II.13)}$$

Where: n_1 and n_2 are the refraction index of the film for the wavelength λ_1 and $\lambda_2$respectively, we can calculate n_1 and n_2 from the following relation:

$$n_{1(2)} = \left[N_{1(2)} + (N_{1(2)}^2 - s^2)^{1/2}\right]^{1/2} \qquad \text{(II.14)}$$

Where: s is the refraction indexes of the substrate and $N_{1(2)}$ can be obtained using this relation:

$$N_{1(2)} = 2s(T_M - T_{m1(2)})/T_M T_{m1(2)} + (s^2 + 1)/2 \qquad \text{(II.15)}$$

With: $T_{m1(2)}$ is the minimum transmittance corresponds with $\lambda_1(\lambda_2)$ and T_M is the maximum transmittance confined between T_{m1} and T_{m2}.

II. 4. 6. 2. Absorption coefficient α:

In the spectral field where the light is absorbed, and by knowing the film's thickness, we can determine the absorption coefficient for each value of transmittance T (%) as follows:

$$\alpha\ (cm^{-1}) = \frac{1}{d} ln\left(\frac{100}{T}\right) \qquad \text{(II.16)}$$

This approximate relation is established, by neglecting the reflexions with all interfaces; air/film, air/substrate [13].

II. 4. 6. 3. Optical Gap E_g:

In high energy, absorption results from electronic transitions between wide states of band to band. It is usually described by Tauc law [16]:

$$\alpha\ (h\nu)\ =\ A(h\nu\ -E_g)^m \qquad \text{(II.17)}$$

Where: $h\nu$ is the photon energy, E_g is optical gap m and A are constants, m characterizes the optical type of transition and takes the values $2, 1/2$ (2 for allowed direct transitions or $1/2$ for allowed indirect transitions). In order to determine the nature of the transition from the films produced in this study, we will plot the curves $(\alpha h\nu)^m\ =\ f\ (h\nu)$ [17]. We can obtain E_g value as it showing in figure (II.15):

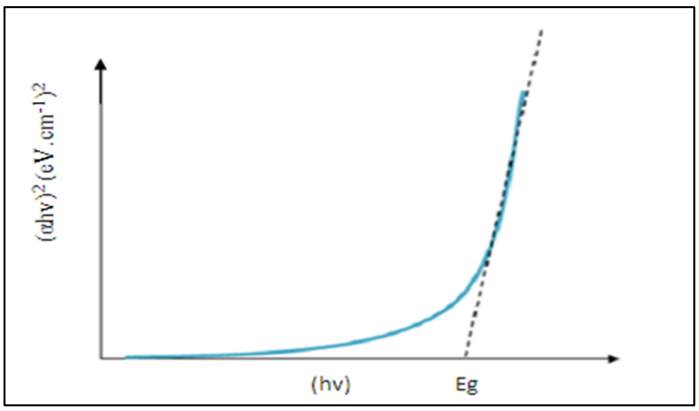

Figure II. 15. Determination of E_g.

References

[1] M. Ohring, *"Materials Science of Thin Films Deposition and Structure"*, 2nd Edition, Academic Press, (2002).

[2] A. Aldrin, *"Preparation and characterization of certain II-VI, I-III-VI$_2$ semiconductor thin films and transparent conducting oxides"*, PhD thesis, Cochin University of Science and Technology, Kerala, India, (2004).

[3] M. C. Sharma., B. Tripathi., S. Kumar., S. Srivastava and Y. K. Vijay, *"Low cost CuInSe$_2$ thin films production by stacked elemental layers process for large area fabrication of solar cell application*", Materials Chemistry and Physics, 131(3), (2012) 600–604.

[4] N. S. Xu and S. E. Huq,*"Novel cold cathode materials and applications"*, Materials Science and Engineering R, 48 (2-5), (2005) 47-189.

[5] J. Singh. *"Physics of semiconductors and their heterostructures"*. (Vol. 84) McGraw-Hill, New York, USA (1993).

[6] R. K. Bhakta, *"Rational development of Precursors for MOCVD of TiO$_2$: Precursor Chemistry, Thin Film Deposition, Mechanistic Studies"*, PhD thesis, Ruhr-University Bochum, Germany, (2005).

[7] A. Ashour., M. A. Kaid., N. Z. El-Sayed and A. A. Ibrahim, *"Physical properties of ZnO thin films deposited by spray pyrolysis technique"*, Applied Surface Science 252 (22), (2006) 7844–7848.

[8] H, Yilmazer., M, Niinomi., T, Akahori., M, Nakai and Y, Todaka, *"Effect of high–pressure torsion processing on microstructure and mechanical properties of a novel biomedical β–type Ti–29Nb–13Ta–4.6 Zr after cold rolling"*, International Journal of Microstructure and Materials Properties, 7 (2-3), (2012) 168-186.

[9] A. Sanchez-Juarez., A. Tiburcio-Silver and A. Ortiz, *"Properties of fluorine-doped ZnO deposited onto glass by spray pyrolysis"*, Solar Energy Materials and Solar Cells 52(3-4), (1998) 301-311.

[10] C. R. Brundle., L. Wilson., C. A. Evans., S. Wilson and G. Wilson, *"Encyclopedia of materials characterization Surface, Interface, Thin Films"*, Gulf Professional Publishing, USA (1992).

[11] R. Manoj, *"Characterisation of Transparent Conducting Thin Films Grown by Pulsed Laser Deposition and RF Magnetron Sputtering"*, PhD thesis, Cochin University of Science and Technology Cochin – 682 022, Kerala, India, (2006).

[12] A. Moustaghfir, *"Élaboration et caractérisation de couches minces d'oxyde de zinc. Application à la photoprotection du polycarbonate"*, PhD thesis, Université Blaise Pascal, Clermont-Ferrand, France, (2004).

[13] S. Kasap and P. Capper, *"Springer Handbook of Electronic and Photonic Materials",* Springer Science and Business Media, (2006).

[14] A. Fouchet, *"Croissance et caractérisations de films minces de ZnO et ZnO dopé cobalt préparés par ablation laser pulsé"*, Doctorate thesis, Caen University, Basse-Normandie, France, (2006).

[15] R. Swanepoel, *"Determination of the thickness and optical constants of amorphous silicon"*, Journal of Physics E: scientific instruments, 16(12), (1983) 1214.

[16] J. Tauc., R. Grigorovici., and A. Vancu, *"Optical properties and electronic structure of amorphous germanium"*, Physica Status Solidi (B), 15(2), (1966) 627- 637.

[17] D. Beena., K. J. Lethy., R. Vinodkumar., V. P. Pillai, V. Ganesan., D. M. Phase, S. K. Sudheer, *"Effect of substrate temperature on structural, optical and electrical properties of pulsed laser ablated nanostructured indium oxide films"*, Applied Surface Science, 255(20) (2009), 8334-8342.

Chapter III

TiO_2 and ZnO thin films deposition

III. 1. Sol-Gel method

The sol-gel method is a wet-chemical synthesis technique for preparation of oxide gels, glasses, and ceramics at low temperature. It's based on control of hydrolysis and condensation of alkoxide precursors. As early as the mid-1800s, interest in the sol-gel processing of inorganic ceramics and glass materials has begun with Ebelman and Graham's studies on silica gels. The investigator recognized that the product of hydrolysis of tetraethoxysilane (TEOS) under acidic conditions is SiO_2. In the 1950s and 1960s Roy and co-workers used sol-gel method to synthesize a variety of novel ceramic oxide compositions with very high levels of chemical homogeneity, involving Si, Al, Zr, etc, which couldn't be made using traditional ceramic powder methods. It's possible to fabricate ceramic or glass materials in a variety of forms, such as ultra-fine powders, fibers, thin films, porous aerogel materials or monolithic bulky glasses and ceramics. Since then powders, fibers, thin films and monolithic optical lens have been made from the sol-gel glass [1].

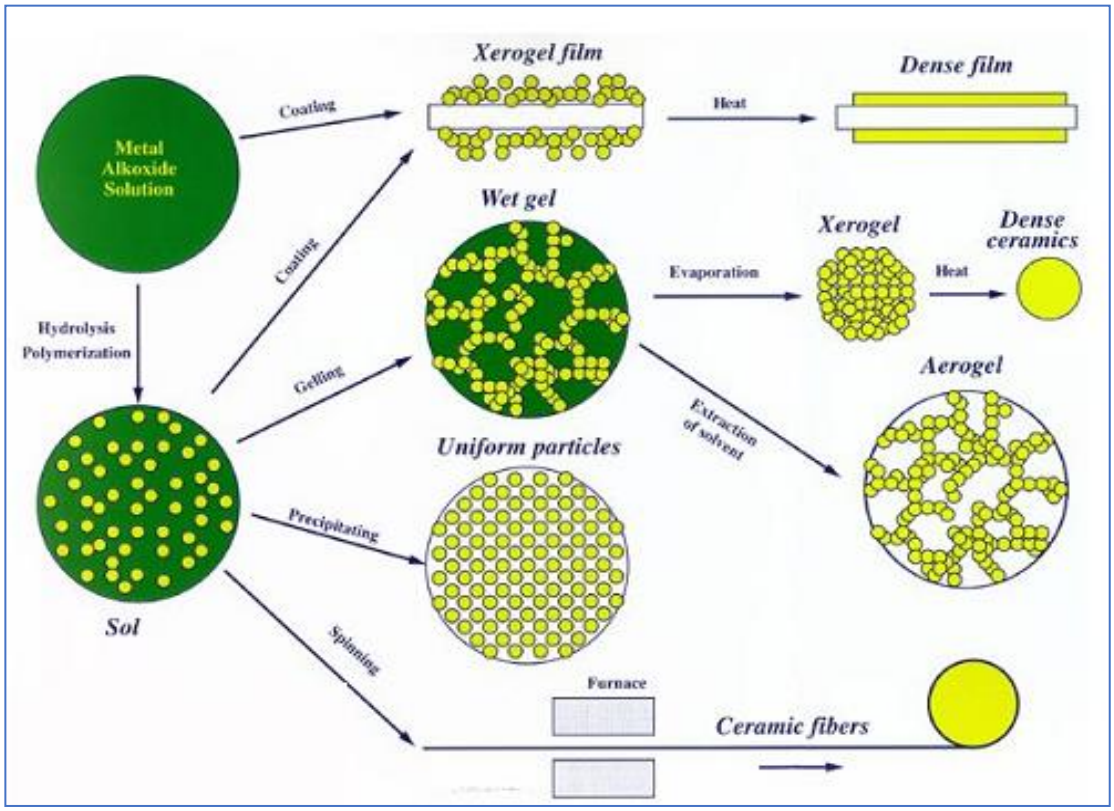

Figure III. 1. Sol-gel process [2].

III. 1. 1. An overview of sol-gel process steps

The sol-gel process, as the name implies, involves transition from a liquid 'sol' (colloidal solution) into a 'gel' phase. Usually inorganic metal salts or metal organic compounds such as metal alkoxide are used as precursors. A colloidal suspension or a 'sol' is formed after a series of hydrolysis and condensation reaction of the precursors. Then the sol particles condense into a continuous liquid phase (gel). With further drying and heat treatment, the 'gel' is converted into dense ceramic or glass materials. Generally, three reactions are used to describe the sol-gel process: hydrolysis, alcohol condensation and water condensation. Because water and alkoxides are immiscible, alcohol is commonly used as co-solvent [1].

The two phases which describe the sol-gel process are defined as follows:

Sol: a stable suspension of colloidal solid particles or polymers in a liquid.

Gel: porous, three-dimensional, continuous solid network surrounding a continuous liquid phase.

III. 1. 1. 1. Hydrolysis and condensation

- **Hydrolysis reaction**

During the hydrolysis reaction, the alkoxide groups (OR) are replaced with hydroxyl group (OH) through the addition of water as shown in the equation below:

$$M(OR)_n + H_2O \rightarrow M(OR)_{n-1}(OH) + ROH \qquad \text{(III.1)}$$

Although hydrolysis can occur without additional catalyst, it has been observed that with the help of acid or base catalyst the speed and extent of the hydrolysis reaction can be enhanced [1]. The mechanism of hydrolysis of a metallic alkoxide $\mathrm{M\,(OR)}_n$ (neutral medium, without additional catalyst) is given as follows [3].

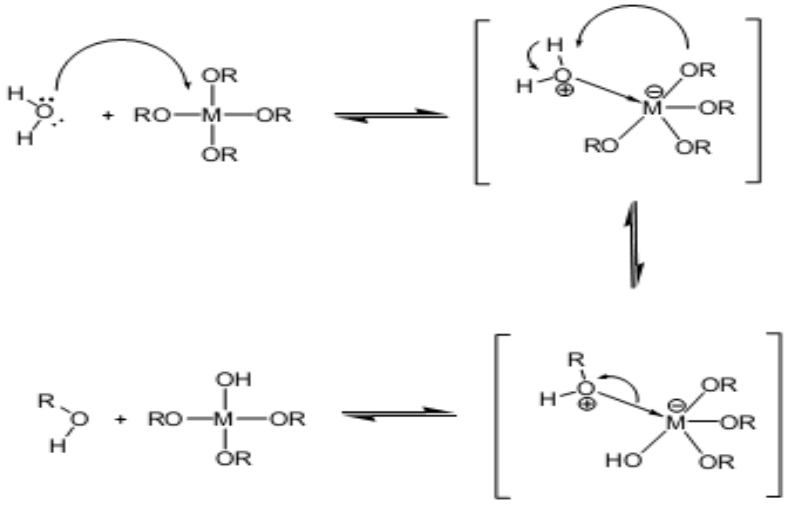

- **Condensation reaction**

The groups ($HO - M\ (-OR)_{n-1}$) generated during the hydrolysis react either with each other to give a molecule of water (oxolation) or with a molecule M of the alkoxy ($-OR$) to give an alcohol molecule (alcoxolation) and leading to the creation of the or each flight MOM oxygen atom becomes a bridge connecting two atoms of the metal M. This leads to the formation of a gel whose its viscosity increases during time; this gel contains solvents and precursors which have not yet reacted. This process is governed by the following reactions at room temperature. The mechanism of oxolation of a metallic alkoxide $M(OR)_n$ [3]:

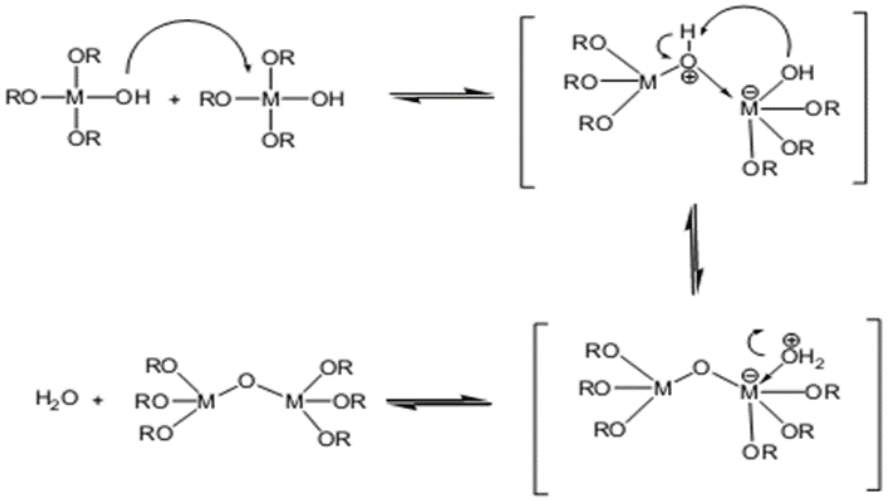

The mechanism of alcoxolation of a metallic alkoxide $M(OR)_n$:

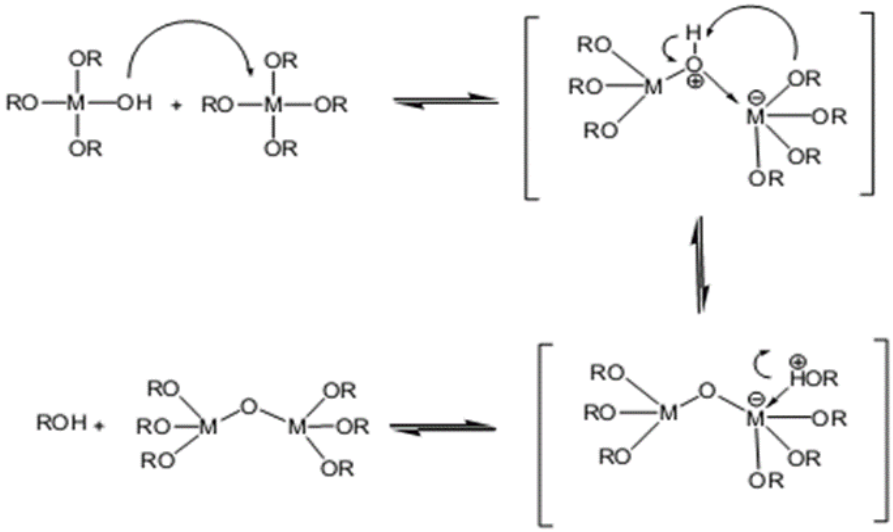

III. 1. 1. 2. Gelation

The simplest picture of gelation is that clusters grow by condensation of polymers or aggregation of particles until the clusters collides; then links form between the clusters to produce a single giant cluster that is called a gel. The giant spanning cluster reaches across the vessel that contains it, so the sol does not pour when the vessel is tipped. At the moment that the gel forms, many clusters will be present in the sol phase, entangled in but not attached to the spanning cluster; with time, they progressively become connected to the network and the stiffness of the gel will increase. According to this picture, the gel appears when the last link is formed between two large clusters to create the spanning cluster. This bond is no different from innumerable others that form before and after the gel point, except that it is responsible for the onset of elasticity by creating a continuous solid network. As one would expect from such a process, no latent heat is evolved at the gel point, but the viscosity rises abruptly and elastic response to stress appears, as shown in figure III. 2. The sudden change in rheological behavior is generally used to identify the gel point in a crude way [4].

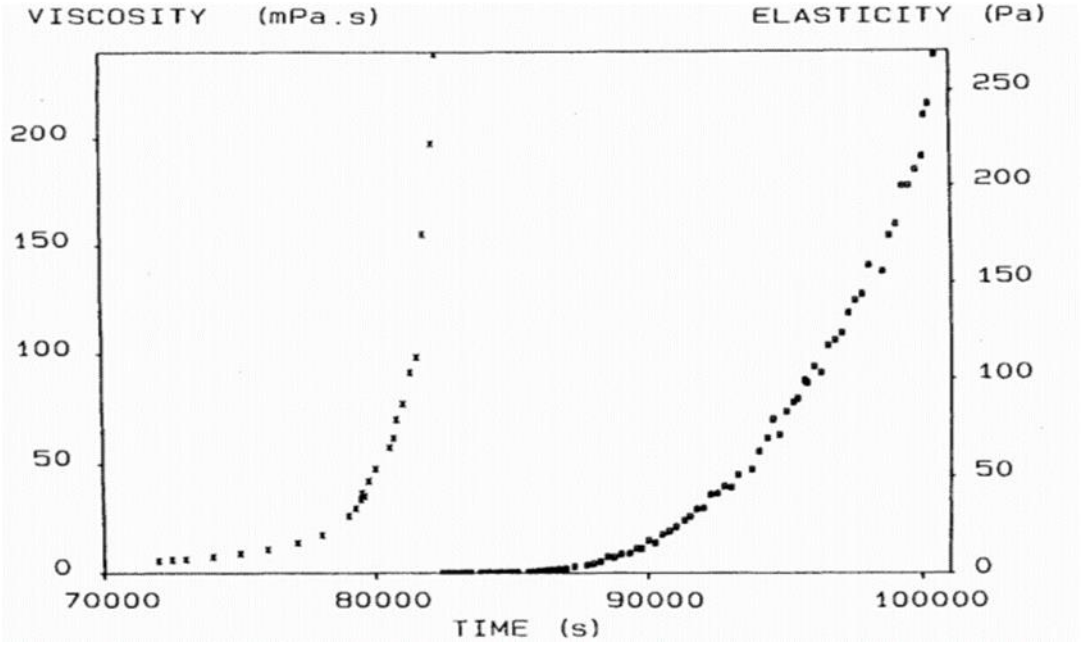

Figure III. 2. Evolution of viscosity (left) and elasticity (right) versus time for silica gel made from tetramethoxysilane [4].

III. 1. 1. 3. Ageing

The continuing chemical and physical changes during ageing after gelation are very important. During this process, further cross-links continuous, the gel shrinks as the covalent links replace non-bonded contacts and the pore sizes and pore wall strengths change with the evolution of the gel's structure [1].

III. 1. 1. 4. Drying

The gel has a high ratio of water and three-dimensional interconnected pores inside the structure. Before the pore is closed during the densification process, drying is needed to remove the liquid trapped in the interconnected pores. On the other hand, removal of the liquid from the tiny pores causes significant stress resulting from inhomogeneous shrinkage. Therefore, the main problem that had to be overcome is cracking due to the large stress in the structure. For small cross sections, such as powder, coating, or fiber, the drying stress is small and can be accommodated by the materials, so no special care is needed to avoid cracking for those sol-gel structures. While for monolithic objects greater than 1 cm, drying stress developed in ambient atmosphere can introduce catastrophic cracking, as a result control of the chemistry of each processing step is essential to prevent cracking during drying [1].

III. 1. 1. 5. Densification

Heat treatment of the porous gel at high temperature is necessary for the production of dense glass or ceramics from a gel. After the high temperature annealing, the pores are eliminated and the density of the sol-gel materials ultimately becomes equivalent to that of the fused glass. The densification temperature depends considerably on the dimension of the pores, the degree of connection of the pores, and the surface areas in the structure [1].

III. 1. 2. Different sol-gel methods

Several techniques can be used for the deposition of thin films on a given substrate: the "spin-coating", the "drain-coating" and "dip-coating". Each having their own characteristics, the choice of method of deposition depends on the characteristics of the substrate such that its geometry or size. The two methods presented below are the most commonly used.

III. 1. 2. 1. Spin-coating

This method involves depositing a small puddle of a fluid resin onto the center of a substrate. Then spinning the substrate at high speed. This technique has the advantage of being easily implemented, for moderate investments. It gives excellent results on planar substrates with dimensions of the order of cm^2. This deposition method can be divided into four phases, shown schematically in figure III. 3:

1) The deposition of the solution.
2) The start of rotation: the acceleration step causes the flow of liquid outwardly of the substrate.
3) Rotating at a constant speed allows the ejection of excess liquid in the form of droplets and the reduction of the thickness of the film uniformly.
4) Evaporation of the more volatile solvent which increases the reduction of the thickness of the deposited film [5]. Final film thickness and other properties depend on the parameters chosen for the spin process.

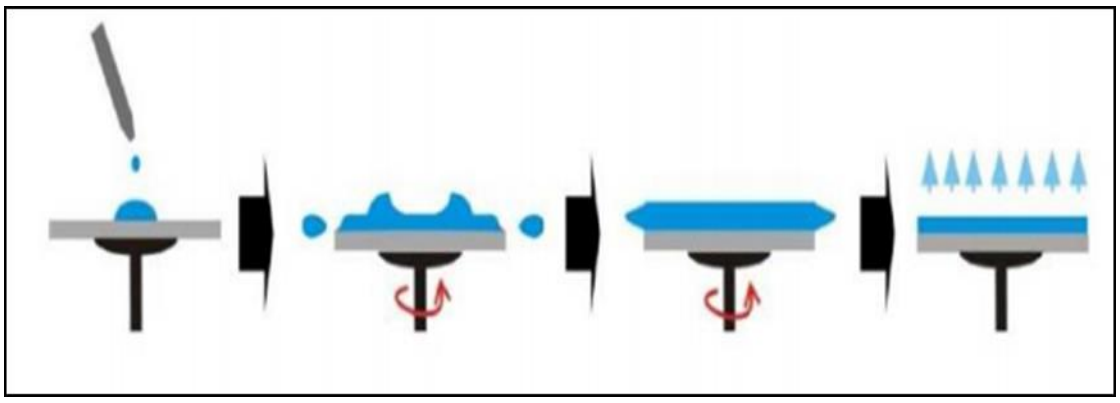

Figure III. 3. The four steps of spin coating [6].

We can measure the film thickness by the equation (III.2), which shows how there is some parameters affect thickness [7]:

$$d = (1 - \rho_A/\rho_{AO}) \,.\, (\, 3\eta.m/2\rho_{AO} \,.\, \omega^2)^{1/3} \qquad \text{(III.2)}$$

In which:

d: thickness.

ρ_A: density of volatile liquid (ρ_{AO} represents the initial mass of solvent over solution volume).

η: viscosity of solution.

m: rate of evaporation.

ω: rotational speed.

Because of the higher rotational speed, the film thickness reduces, a simpler equation is suggested as below:

$$d = \alpha\omega^{-2/3} \quad \text{(III.3)}$$

Where: α is a constant parameter that should be calculated experimentally.

III. 1. 2. 2. Dip-coating:

The dip-coating technique can be described as a film deposition process where the substrate to coated is immersed in a liquid and then withdrawn with a well-defined speed under controlled temperature and atmospheric conditions.

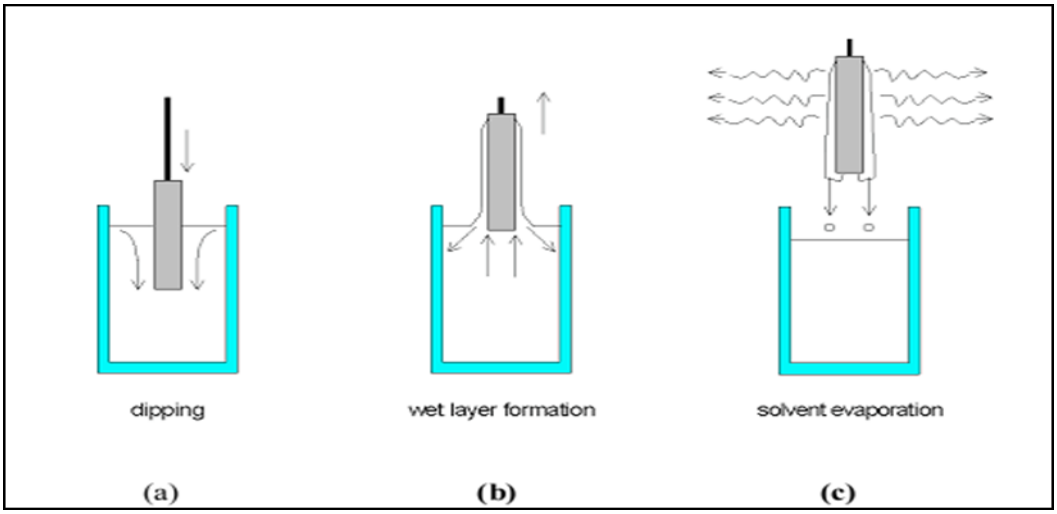

Figure III. 4. Stages of the dip-coating process: a) dipping of the substrate into the coating solution; b) wet layer formation by withdrawing the substrate; c) gelation of the layer by solvent evaporation [2].

III. 1. 3. Advantages and disadvantages of sol-gel method

III. 1. 3. 1. The advantages

The advantages of this method are manifold making it a coveted method; we quote here their main advantages:

- Simplicity of the process and speed of execution.
- Simultaneously coating both sides of the substrate in a single operation (dip-coating) and the ability to form multilayer.
- Feasibility of multicomponent coatings by simply mixing the corresponding alkoxy in the starting solution.
- Ability to optimize the morphology of the films based on researched applications.
- Ability to produce thin layers of inorganic oxides at low temperature on heat sensitive substrates.
- Possibility of making organo hybrid materials as thin or monolithic layers with specific properties.
- Doping facilitated in large quantities.

III. 1. 3. 2. The disadvantages

The main disadvantages are:

- Cost of high - alkoxide precursors.
- Manipulation of a large amount of solvents.
- The major drawback is the low thickness of the layers, so one must perform several steps of depositing and drying to obtain a thickness of several hundred nanometers, this increases the risk of cracking as the first deposited layers undergo all successive drying which increases the risk of short circuit when the electrical tests.

III. 2. Apparatus used (Spin coater)

The spin coater which was used to deposit the TiO_2 and ZnO thin films has the following shape and characteristics:

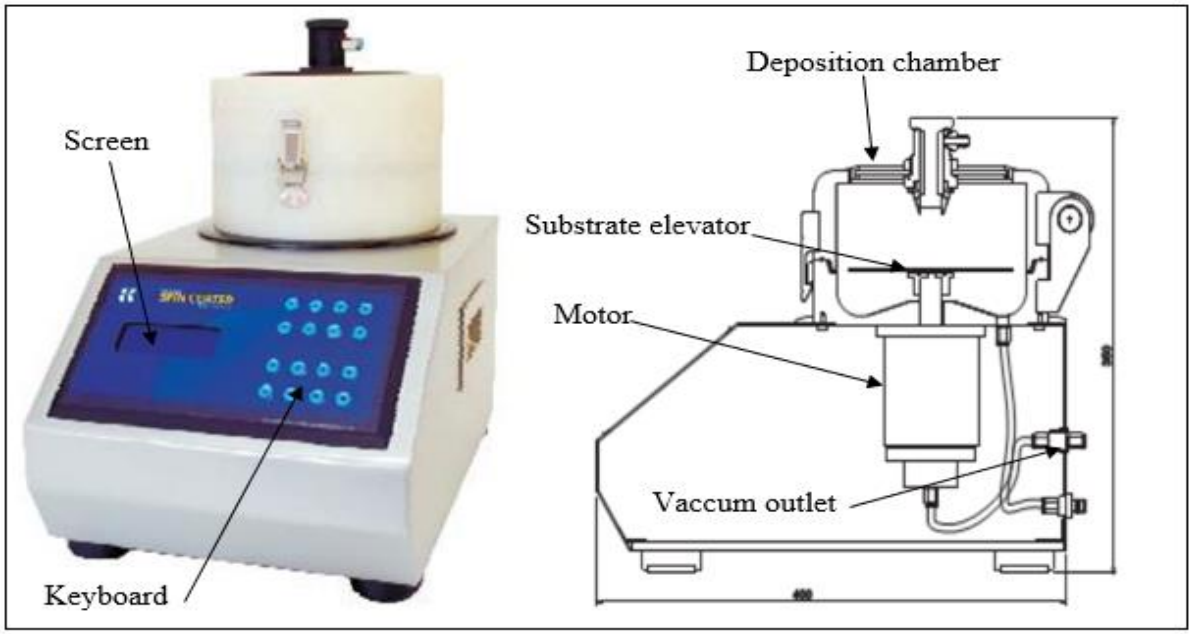

Figure III. 5. Holmarc Spin coater.

III. 2. 1. How does a spin coater work?

Firstly, deposition parameters are adjusted using the keyboard. Then, the substrate is placed onto the substrate elevator in the deposition chamber where it is fixed by a vacuum bomb through the vacuum outlet, after that, the precursor solution is dropped on the substrate. Once the deposition chamber is closed, we switch on the motor to rotate the substrate.

III. 2. 2. Specifications

Actuator.....	Brushless DC motor
Spinning speed.....	10-8000 rpm
Maximum substrate size.....	100 mm diameter
Power input.....	230V, 50Hz
Read out.....	20 x 4 line LCD
Acceleration.....	0-2000 rpm/sec
Spinning speed accuracy.....	< 5%
Programmable parameter.....	Speed, acceleration, dwell time and number of steps
Maximum number of steps.....	5

III. 3. Preparation of the substrate

III. 3. 1. Choice of the substrate

The studied films were deposited on substrates of solid glass which have a length of 2.5 cm and a width of 2.5 cm, the choice of glass like substrate of depot was adopted because of the following reasons:

- The thermal compatibility with TiO_2 and ZnO (thermal dilation coefficients is $\alpha_{glass} = 3.3 \times 10^{-6}K^{-1}$, $\alpha_{TiO_2} = 8 - 10 \times (10^{-6}K^{-1})$ and $\alpha_{ZnO} = 3.9 \times 10^{-6}K^{-1}$) which minimize the stress in the interface film/substrate.
- For their transparency which adapts well for the optical characterization of films in the visible one.
- As it is insulator it will not affect the conductivity measurement.
- For economic reasons.

III. 3. 2. Cleaning of the substrate

The adherence and the quality of the depot repose on purity and the state on substrate thus the cleaning of the substrate is one of the most important steps, the cleaning of our substrates surfaces is as follows:

- The substrates are cut using a pen with diamond point.
- Cleaning with soap solution.
- Rinsing with the water distilled and then with acetone during 5 min.
- Rinsing with distilled water.
- Rising with methanol during 5 min at ambient temperature.
- Cleaning in water distilled bath.
- Drying using a drier.

III. 4. Solutions preparation and film deposition

III. 4. 1. Titanium dioxide

To prepare the solution we use $0.605\ ml$ of Titanium Tetra Isopropoxide (TTIP) $Ti[OCH(CH_3)_2]_4$ ($Molecular\ weight\ =\ 284.25\ g.mol^{-1}$) as precursor, $10\ ml$ of ethanol as solvent (for a solution with a concentration of $0.2\ mol.L^{-1}$) and an amount of a catalyser (see table IV.1) , this last acts as stabilizer which its molar ratio to TTIP was fixed at 1. The mixture was stirred by a magnetic stirrer at 50 °C for 3 h until obtained a clear, yellowish and a little viscous solution. The prepared solution was dropped on glass substrate then it was rotated at 4000 rpm for 30 s. After each coating, the coated film was dried at 250 °C for 10 min on a furnace. This step was repeated for 5 times to obtain a multilayer film which were annealed in air furnace for 2 h. The flow chart of the preparation of TiO_2 thin films is shown in figure III. 6:

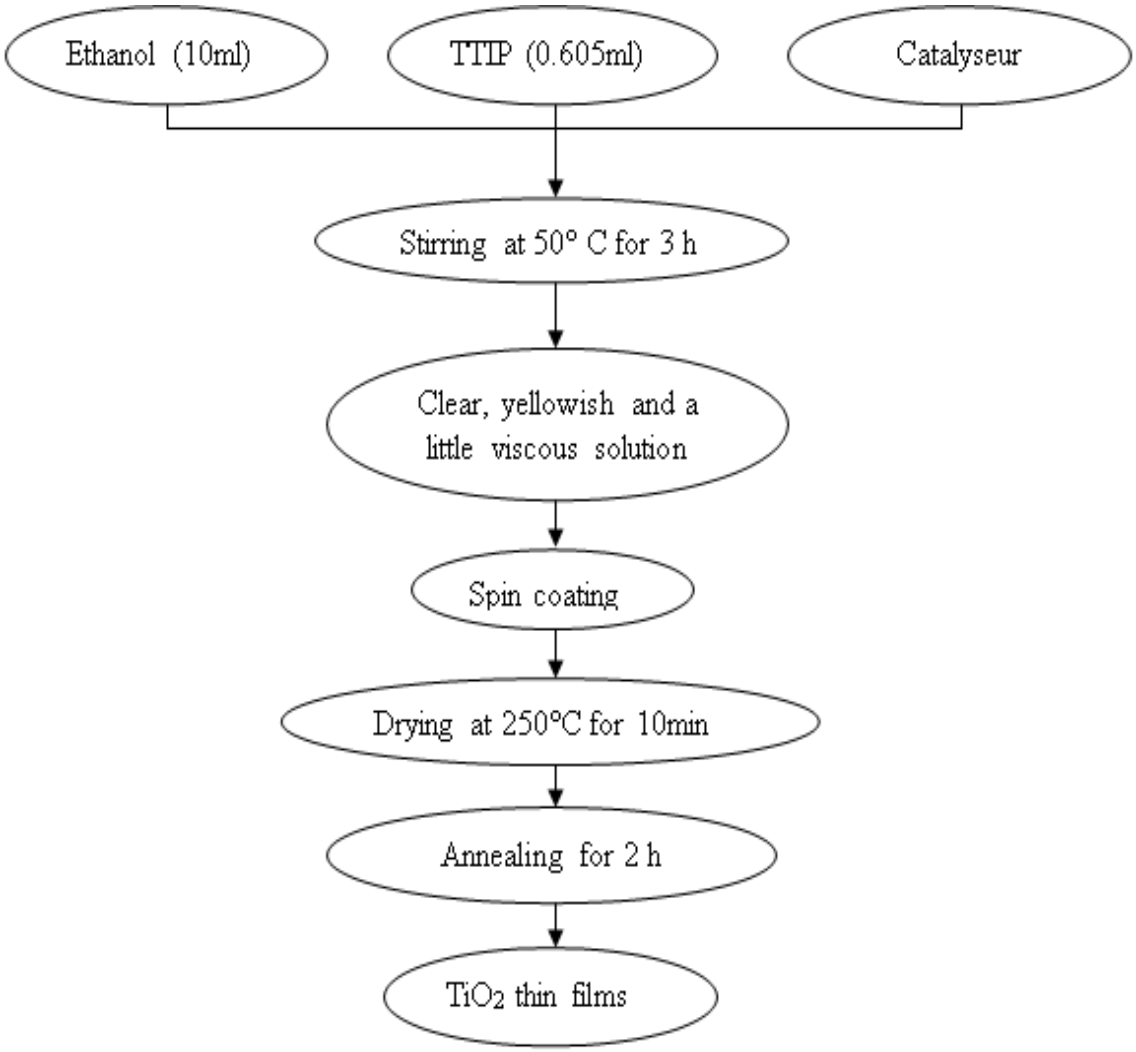

Figure III. 6. TiO_2 thin films deposition steps.

III. 4. 2. Zinc oxide

Zinc acetate dihydrate (Zn $(CH_3COO)_2.2H_2O$) ($Molecular\ weight = 219.5\ g.mol^{-1}$) was used as the starting material source. A homogeneous and stable solution with a concentration of 0.6 mol. L^{-1} was prepared by dissolving 2.635g of (ZAD) in 20 ml of ethanol (CH_3CH_2OH) and an amount of a catalyser (see table V. 1) which its molar ratio to (ZAD) was fixed at 1. The mixture was stirred by a magnetic stirrer at 50 °C for 2h until obtained a clear and homogeneous solution then allowed to age for 48 h.

The precursor solution mentioned previously was dropped on glass substrate until the covering of all the surface (the sufficient quantity is V= 0.25 ml). The substrate was rotated by using spin coater; the spinner reached 4000 rpm after 10 s which was maintained for 30 s. After each coating, the coated film was dried (preheated) at 250 °C for 10 min on a furnace since the thermal decomposition temperature of zinc acetate is 237 °C, the preheat-treatment temperature of 250 °C is required for the evaporation of organic solvents and the initiation of formation and crystallization of the ZnO film. After the deposition and drying of the sixth layer, the resulting thin films were inserted into a furnace and annealed in air for 2 h , then left to cool down to ambient temperature the flow chart of the preparation of ZnO thin films is shown in figure III. 7.

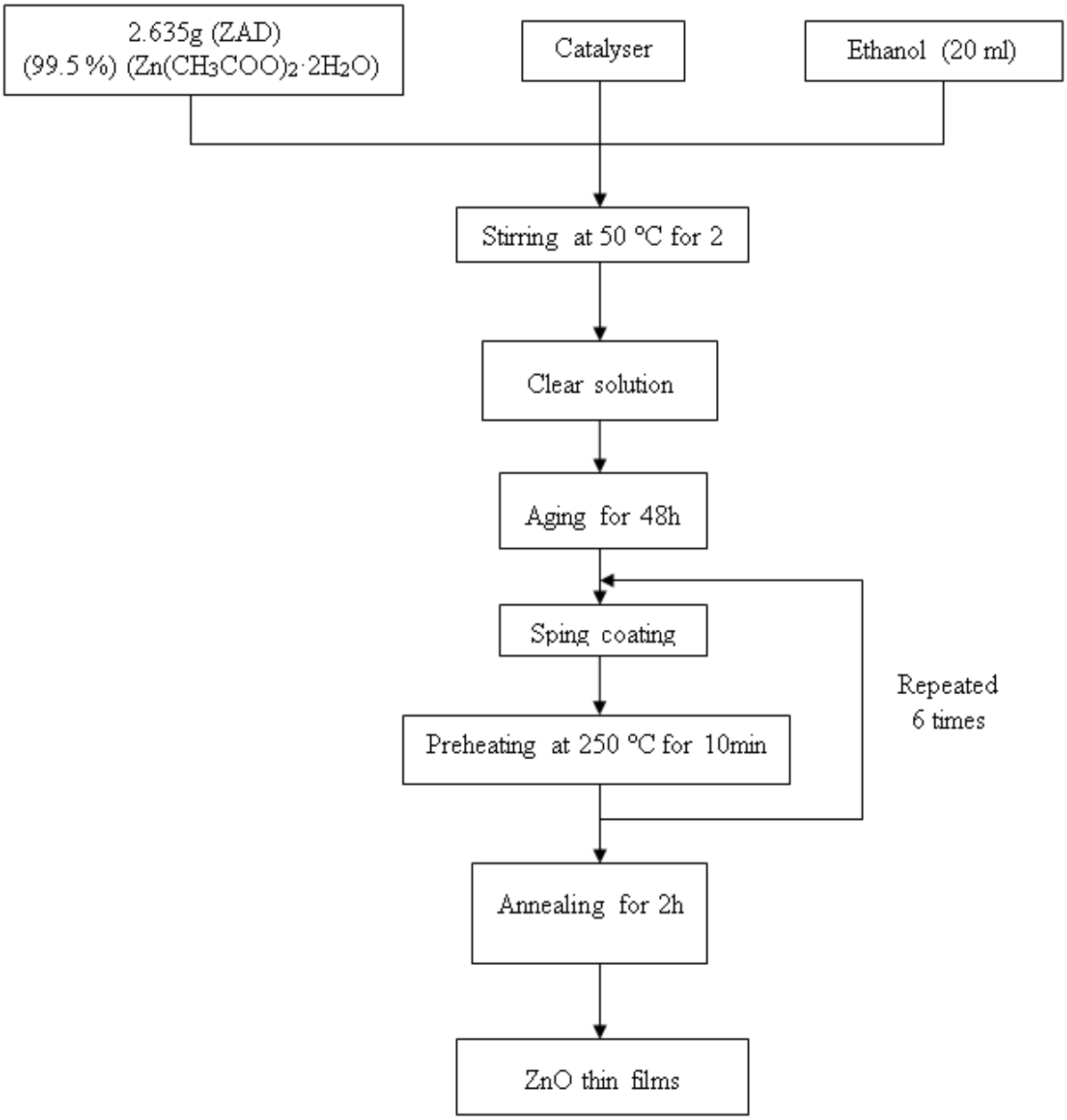

Figure III. 7. Flow chart of sol–gel method for preparation of ZnO thin films.

References

[1] L. Yang, *"Fabrication and characterization of microlasers by the Sol-Gel method",* PhD Thesis, California institute of technology, Pasadena, California, USA, (2005).

[2] E. Marenna., *"Sol-Gel Synthesis of functional nanocomposites based on inorganic oxides",* PhD Thesis, University of Naples Federico II, Italia, (2008).

[3] F. Collignon, "*Cahier technologique Sol-Gel",* Centre de Ressources Technologiques en Chimie B-7180 Seneffe – Belgium.

[4] C. J. Brinker and G. W. Scherer, *"Sol-gel science: The Physics and Chemistry of Sol-Gel Processing",* Academic press, Inc, USA, (1990).

[5] N. Nagayasamy., S. Gandhimathination and V. Veerasamy, *"The effect of ZnO thin films and its structural and optical properties prepared by Sol-Gel spin coating method",* Open Journal of Metal, 3, (2013) 8-11.

[6] L. Nadar, *"Surfaces fonctionnalisées à base de nanoparticules métalliques pour l'optique et la photonique",* PhD thesis, Jean Monnet university, Saint-Etienne, France, (2011).

[7] D. Meyerhofer, *"Characteristics of resist films produced by spinning",* Journal of Applied Physics, 49(7), (1978) 3993-3997.

Chapter IV

TiO_2 thin films characterisation (results and discussion)

IV. 1. Introduction

As mentioned above the aim of this work is to obtain TiO_2 thin films with appropriate properties for photovoltaic applications, in particular, these films should be well crystallized, have a high transparence in the visible region accompanied with a high absorbance in the UV and it should be conductive, thus, it is necessary to optimize the elaboration conditions such as annealing temperature and molar concentration…

This chapter is devoted to analysis the deposited films using the characterization tools mentioned in the paragraph (II.4), we were also interested in the study of the transformation of their properties with the variation of the following parameters:

- The nature of the stabilizer.
- Annealing temperature.
- Molar concentration.
- Amount of Zn doping.

Table IV. 1. A summary table of the experimental conditions of TiO_2 thin films deposition.

Nature of stabilizer	Annealing temperature $(°C)$	Molar concentration $(mol.L^{-1})$	Amount of doping $Zn(at.\%)$
Acetylacetone $(AcAc)$	600	0.2	0
Hydrochloric acid (HCl)			
Sulfuric acid (H_2SO_4)			
Acetylacetone $(AcAc)$	400	0.2	0
	450		
	500		
	550		
	600		
Acetylacetone $(AcAc)$	600	0.1	0
		0.15	
		0.2	
		0.25	
		0.3	
		0.35	
		0.4	
Acetylacetone $(AcAc)$	600	0.2	0
			4
			6
			8

IV. 2. Nature of stabilizer effect on TiO_2 thin films properties

In this series we have prepared three samples using different stabilizers which are Acetylacetone ($AcAc$), Hydrochloric acid (HCl) and Sulfuric acid (H_2SO_4). The first belongs to the ketones group and the other two are acids.

As these solutions are hazardous (harmful flammable and corrosive (acids)) it can be dangerous to the body, especially to the skin, eyes, and respiratory system, thus, we must take gloves and glasses when handling them.

IV. 2. 1. Adhesion test

The term adhesion refers to the interaction between the closely contiguous surfaces of adjacent bodies, i.e., a film and substrate. According to the American Society for Testing and Materials (ASTM), adhesion is defined as the condition in which two surfaces are held together by valence forces, by mechanical anchoring, or by both together. Adhesion to the substrate is certainly the first attribute a film must possess before any of its other properties can be manifested or exploited. Even though it is of critical importance, adhesion is one of the least understood properties. The lack of a broadly applicable method for quantitatively measuring adhesion makes it virtually impossible to test any of the proposed theories for it.

The simplest and quickest qualitative measure of film or coating adhesion is *Tape Test* which consists of:

An adhesive tape is applied to the film surface and pulled off again. The tape test is a subjective test which is not only dependent on the type of tape but also on the pull off velocity and the pull off angle [1].

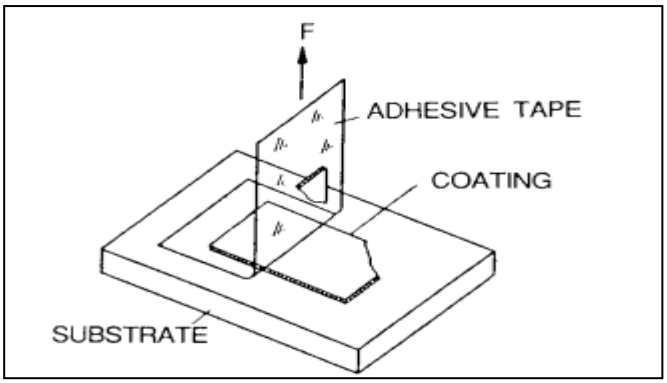

Figure IV. 1. Adhesive tape test [1].

For our films we make the test above, thereafter we observed no delaminates either completely neither partially so we can say that the adhesion of the films is acceptable.

IV. 2. 2. Structural study

X-ray spectra of the titanium dioxide thin films were done using Mini-Flex (Rigaku) diffractometer with a copper anode having a wavelength $\lambda_{k\alpha}(Cu) = 1.5405$ Å. The XRD spectra are given in Fig (IV.2). It was found that the material observed is TiO_2 polycrystalline having tetragonal structure of anatase which is agree with JCPDS (n° 21-1272). TiO_2 thin films were grown preferentially along to the [101] direction whatever the stabilizer used since this direction has minimum energy to growth. Also, we have to note that the peak (101) intensity was affected by the nature of stabilizer where it has the highest value for the films deposited using AcAc as stabilizer. In addition, this last display additional weak peaks such as (004) and (200).

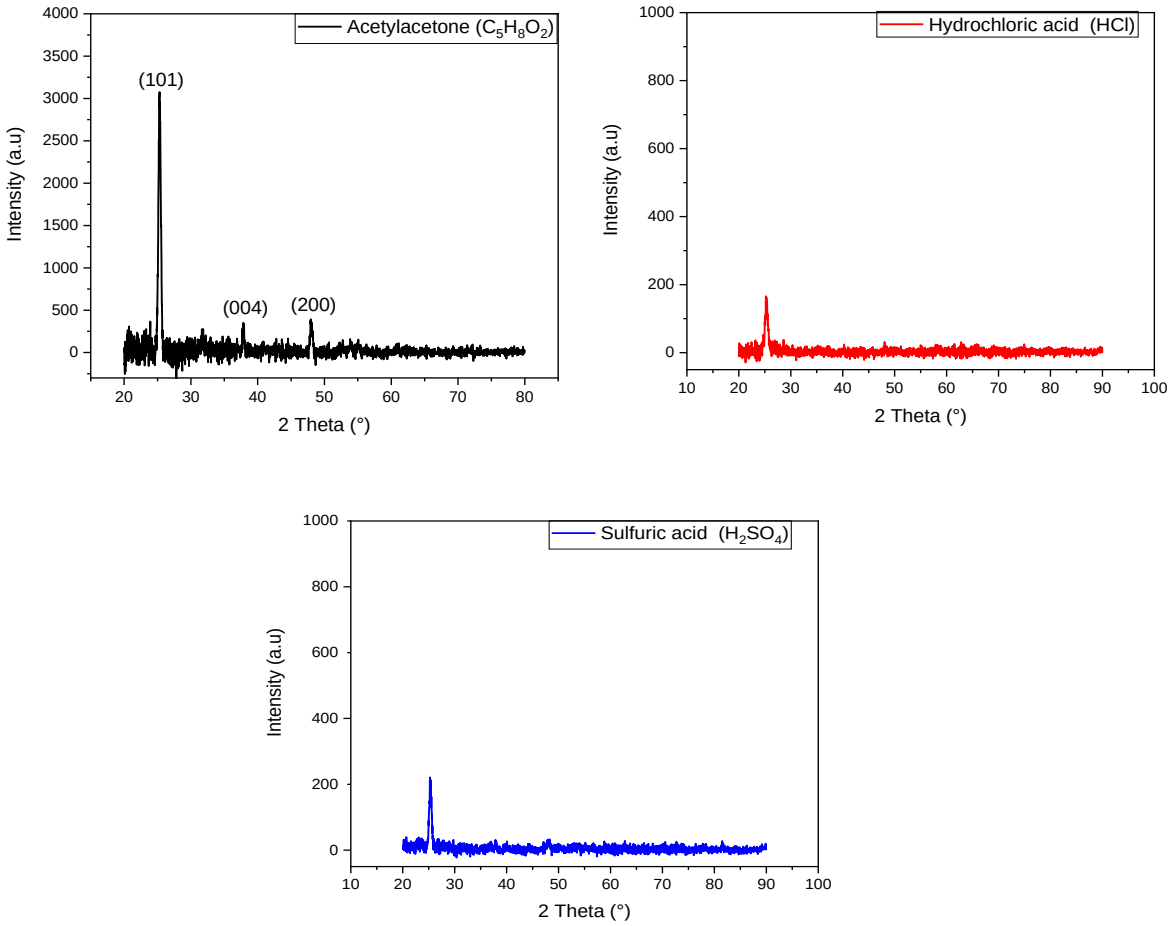

Figure IV. 2. X ray patterns of TiO_2 thin films prepared with different stabilizers.

The crystallite size D was calculated using Scherrer's formula (II.2). It is worthwhile noting, from table IV. 2. and fig IV. 3, that the films prepared using AcAc exhibit the largest crystallite size as compared to the other films which indicates that the AcAc stabilizer has improved the TiO_2 films crystallinity.

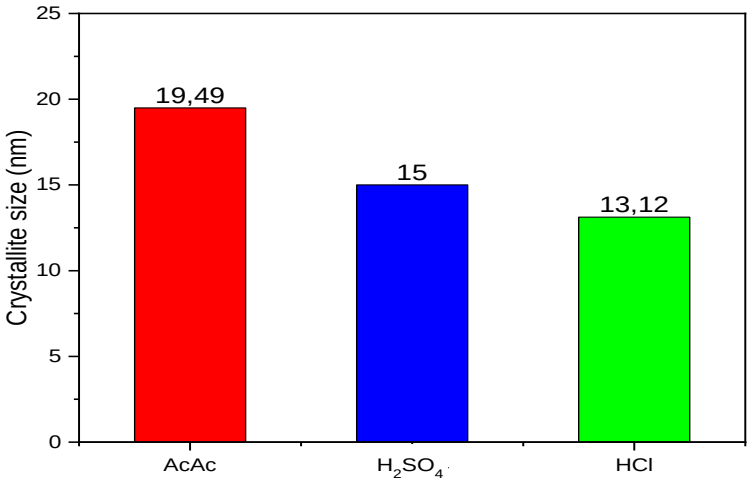

Figure IV. 3. Crystallite size variations.

IV. 2. 3. Raman spectroscopy

Fig IV. 4. shows the room temperature Raman spectrum of the TiO_2 thin films from 100 cm^{-1} to 800 cm^{-1}. The Raman spectrometer which was used in this study is HORIBA scientific (OLYMPUS 41) spectrometer. The spectra show five bands at $145.1, 197.9, 398.4, 516.3$ and 639 cm^{-1} which are corresponding to the fundamental modes' frequencies of anatase which confirm the existence of only anatase phase as stated in the XRD study. In particular, the very intense peak at $\upsilon = 145.1$ cm^{-1} is an E_g mode related to $O - Ti - O$ bending mode characterized by a soft force constant [2]. Table IV. 2, displays a comparison between our results and previous studies, Jorge Medina-Valtierra et al. [3] affirmed that differences with data reported in the literature are reasonable due to the structural distortions into the thin films or by intra-grain defects in samples which is confirmed by the reverse fit between the crystallite size and Raman intensity. Furthermore, the relative intensity, frequency and linewidth of the Raman modes is strongly dependent on the nature of stabilizer, where the films prepared using HCl present a high intensity for all the modes. In contrary, the films prepared with AcAc present a single E_g Raman mode.

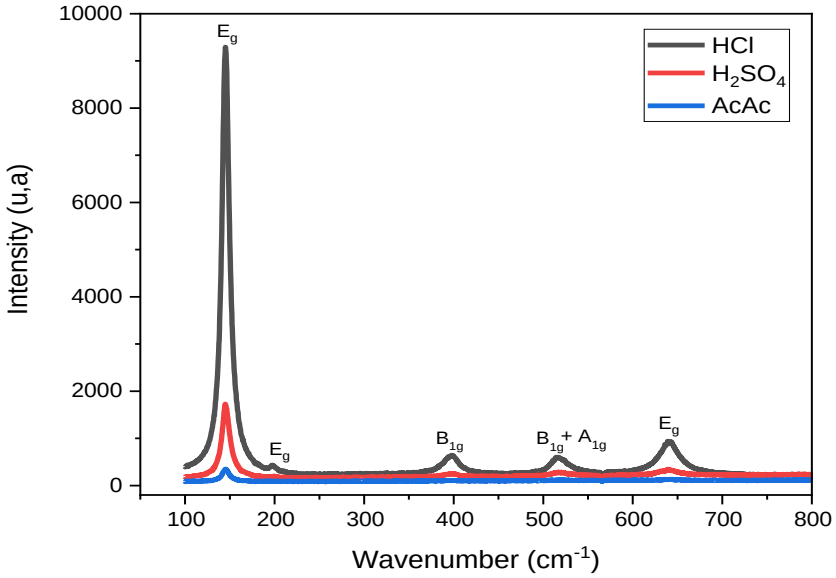

Figure IV. 4. Raman shift.

Table IV. 2. Frequency and assignment of the Raman bands of anatase TiO_2 [3].

Frequency (cm^{-1})	Frequency (cm^{-1}) in this work	Assignment
143	145.1	E_g
197	197.9	E_g
398	398.4	B_{1g}
513	516.3	$B_{1g} + A_{1g}$
639	639	E_g

IV. 2. 4. Optical study

The spectrophotometer exploited in all of our studies is Perkin Elmer Lambda 25 UV-VIS spectrophotometer. Transmittance spectra were given in fig IV. 5, as can be seen from this figure the films prepared using $AcAc$ show a high transmittance value in the visible region reaches to 86 %. We attribute the relatively high transmittance $AcAc$-prepared films to the large crystallite size and low grain boundaries. Also, these films present interference fringes as an indication of smooth and uniform films [4]. In opposition, the films with H_2SO_4 and HCl has a weak transmittance amount less than 60 % which refer to the small crystallite size and

high grain boundaries which may contain an elevated defect concentration which act as scattering centres.

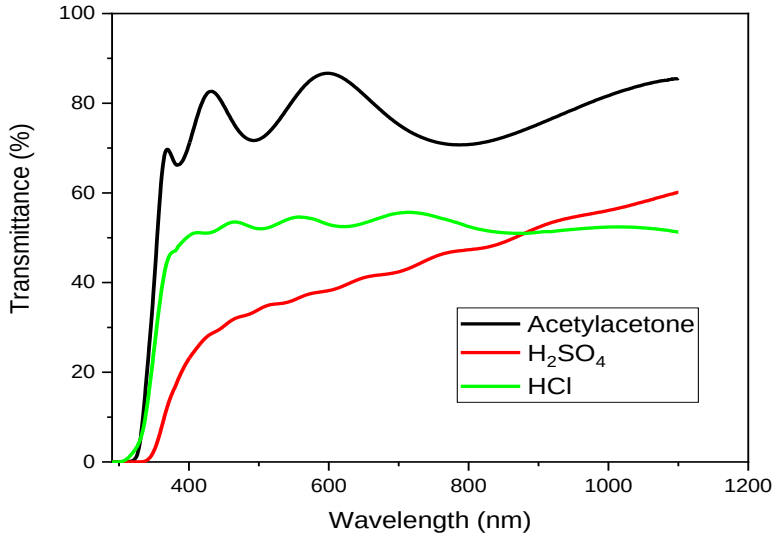

Figure IV. 5. Transmittance spectra of TiO_2 thin films prepared using different stabilizers.

There are many experimental results or calculations on the band structure of anatase assume that it has a direct band gap [5], but there are still several papers on the evaluation assuming an indirect band gap [5]. Here, we evaluated the optical band gap of our TiO_2 thin film assuming both direct and indirect transitions where their energies were established by extrapolating the linear parts of the $(\alpha h\nu)^2$ and $(\alpha h\nu)^{1/2}$ versus $h\nu$ curves, respectively.

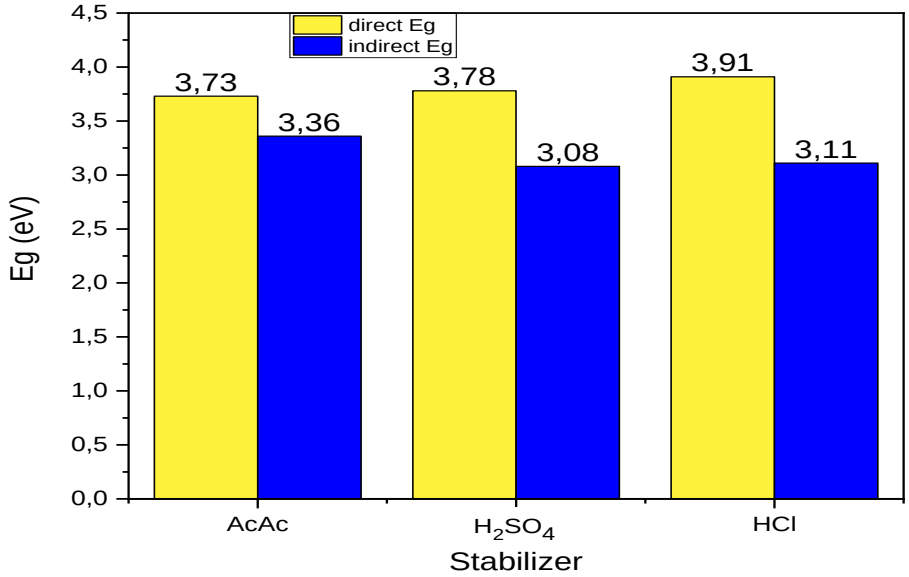

Figure IV. 6. Effect of the stabilizer nature on TiO_2thin films optical band gaps.

Corresponding to the fig IV. 6, the direct band gap takes high values compared to the bulk anatase one (3.2 eV) especially for HCl −prepared films in which, the film microstructure may alter the optical gap. It is well argued that in small crystallites, with the size of the exciton Bohr radius, the exciton is confined and the crystallites lose their bulk-like properties. This feature is called the quantum confinement effect, it causes the band gap widening in a semiconductor containing [6]. On the other hand, the values of the indirect band gap are very close to the bulk one.

IV. 2. 5. Photoluminescence studies

Figure IV. 7, depicts the photoluminescence spectrum of TiO_2 thin films prepared with different stabilizers and excited at 3.88 eV (320 nm). The $AcAc$-prepared films reveals four emission peaks. The first peak was at 356 nm (3.49 eV) which can be attributed to the exciton trapped at shallow level defects [7]. The second peak was appeared at 380 nm (3.20 eV) is due to phonon assisted indirect transition. The 460 nm peak and the broad peak centred at 592 nm are attributed to defect states due to oxygen vacancies [8, 9]. It is clear from the fig IV. 6, that the TiO_2 films prepared with $AcAc$ and those with HCl have approximately the same PL spectra shape with less intensity for this last. In the other hand, the PL emission peaks were disappeared in H_2SO_4 -prepared films (intensity ≈ 0) i. e., the emitted light may not be effectively detected, or these films may produce different kinds of defects such as non-radiative defects.

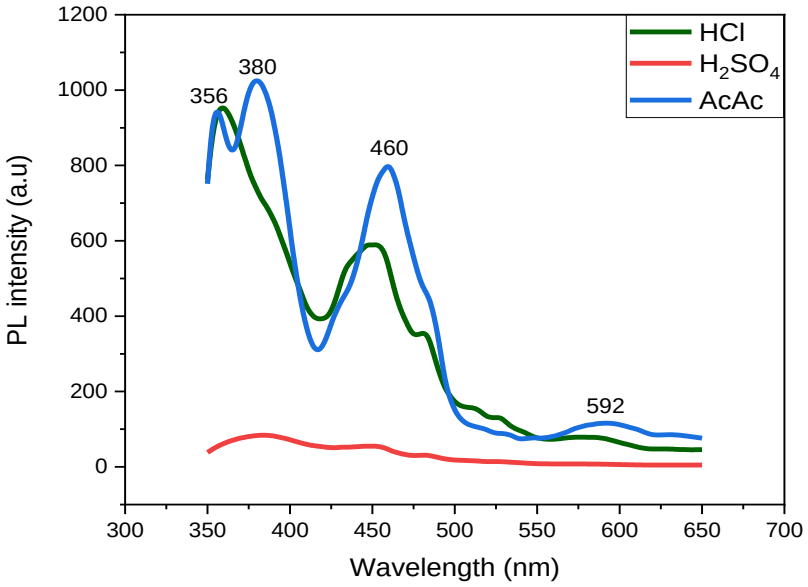

Figure IV. 7. Photoluminescence spectrum of TiO_2 thin films.

IV. 3. Effect of annealing temperature

Annealing is heat treatment of materials at elevated temperatures aimed at investigating or improving their properties. Material annealing can lead to phase transitions, recrystallization, polygonization, homogenization, relaxation of internal stresses, removal of after effects of cold plastic deformation (strain hardening), annihilation and rearrangement of defects and so on. The results of annealing depend significantly on its kinetics: the rate of heating and cooling and the time of exposure at a given temperature [10], to check these effects we have changed the annealing temperature from 400 to $600\ °C$, where the difference between two consecutive values is $50\ °C$.

IV. 3. 1. Thickness variations

Swanepoel method (see paragraph II. 4. 6. 1) was used to calculate the films thickness's, as fig IV. 8 illustrates, the thickness increases from $487\ nm$ to $514\ nm$ as annealing temperature increases from $400\ °C$ to $600\ °C$ so that we can say that it is almost constant. The slight increment may be due to the adsorption of air oxygen atoms in high temperatures on the one hand and the little change in the density on the other.

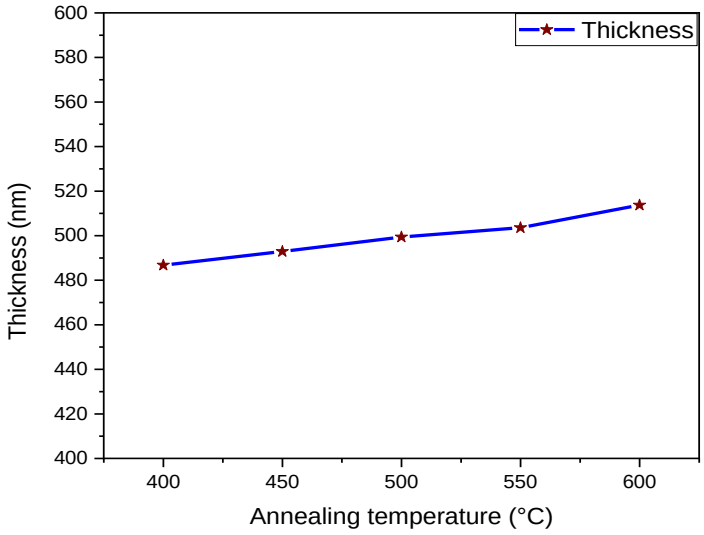

Figure IV. 8. Effect of annealing temperature on the thickness of the films.

IV. 3. 2. Structural characterization

Fig IV. 9 shows the X-ray patterns of annealed TiO_2 films. It has been found that the material observed is TiO_2 polycrystalline having tetragonal structure of anatase. For a crystalline phase to develop, the depositing atoms should have sufficient energy. This gives the atoms sufficient mobility to position themselves to low energy positions leading to the formation of crystalline phases. High annealing temperatures can achieve the sufficient energy to generate crystalline phases. This may be the reason for the growth of crystalline anatase phase in the present study [11]. It can be seen that the intensity of the (101) peak is higher than the others this may be due to the value of the free surface energy is minimal in this direction [12]. Also, it is clear that the intensity of (101) peak slightly increases with the increase of annealing temperature from 400°C to 600°C, i.e., the increasing annealing temperature improved the crystallinity of TiO_2 [11].

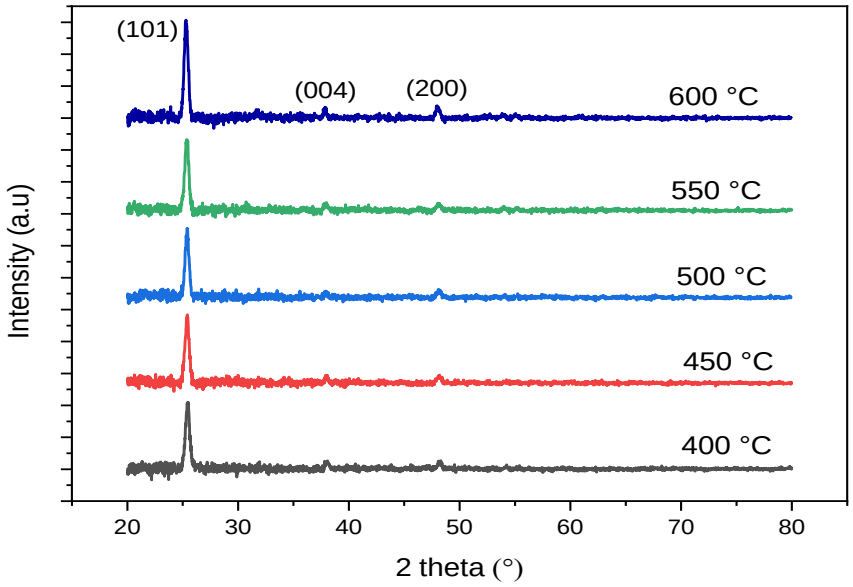

Figure IV. 9. XRD patterns of annealed TiO_2 thin films (The diffractometer used is $X'Pert\ Pro$).

The crystallite size D was calculated from Scherrer's formula. From fig IV. 10 and table IV. 2 we observe that the $FWHM$ slightly decreases when the annealing temperature increases. Decreasing in the $FWHM$ value leads to increase in crystallite size. This may probably be attributed to the following: when the film atoms obtain enough energy in the annealing process they will migrate and restructure into thin films. The crystallites then grow larger correspondingly [13].

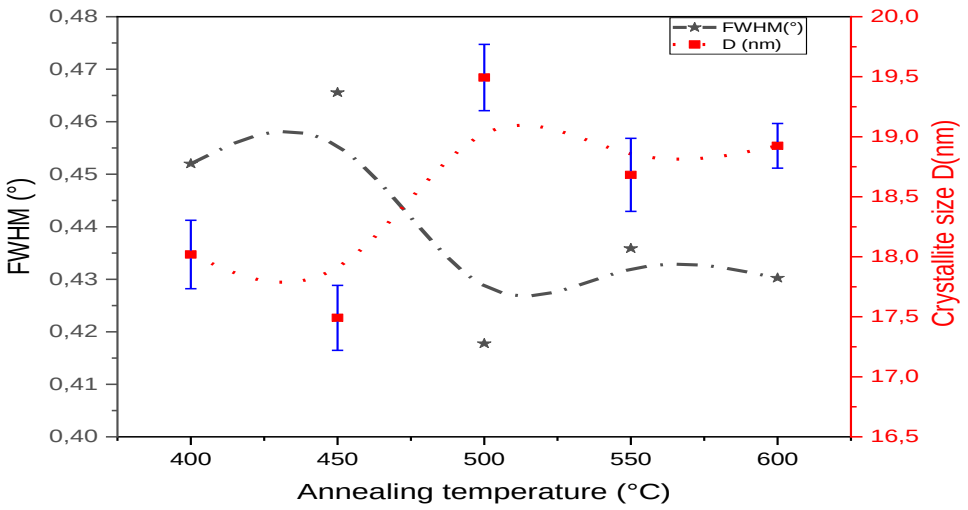

Figure IV. 10. Full width at half maximum (FWHM) and crystallite size D variations.

The residual strain ε and dislocation density δ were determined as follows [14]:

$$\varepsilon = \beta\cos\theta/4 \qquad \text{(IV.1)}$$

Where β is $FWHM$ in radians and θ is the Braggs angle. The dislocation density is defined as the length of dislocation lines per unit volume of the crystal, and it is estimated from the subsequent relation using simple approach of Williamson and Smallman [15]:

$$\delta = 1/D^2 \qquad \text{(IV.2)}$$

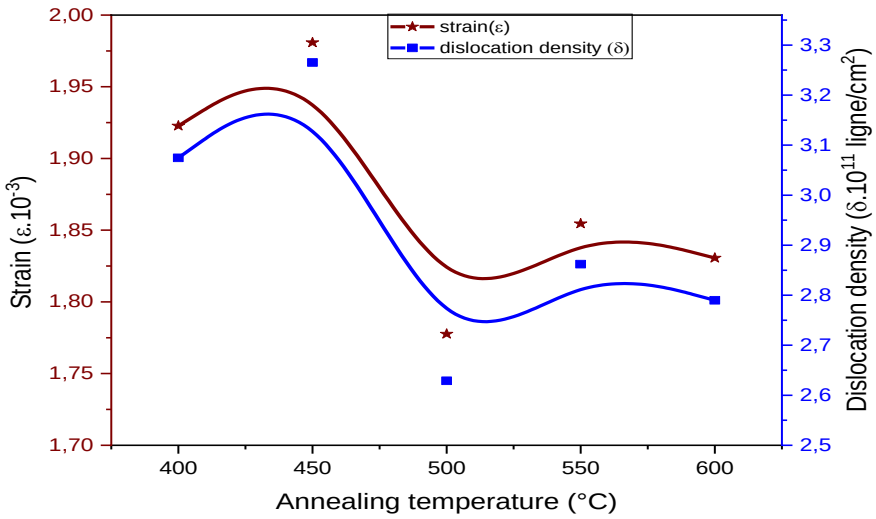

Figure IV. 11. Strain ε and dislocation density δ as a function of annealing temperature.

The strain values for the TiO_2 films deposited at the annealing temperature of 400, $450, 500, 550$ and 600 are $1.92, 1.98, 1.78, 1.85$ and 1.83 $(.10^{-3})$ respectively. Our results revealed a decrease of strain in the films with annealing temperature. This is due to the increase of crystallite size with temperature that led to reduction in inter-crystalline barriers as grain boundary area in the layers. Moreover, at higher growth temperature, the surface mobility increases, allowing the film to decrease its total energy by growing large grains thereby decreasing its grain boundary area [16].

The micro stress σ was calculated using the following formula [17]:

$$\sigma_{stress} = (\varepsilon/2).E \qquad \text{(IV.3)}$$

Where E is the Young's modulus of the TiO_2 ($E = 282.76\ GPa$) and ε is the strain of the film.

The lattice constants 'a' and 'c' of the films are calculated from [17]:

$$1/d^2 = (h^2 + k^2)/a^2 + l^2/c^2 \qquad \text{(IV.4)}$$

From table IV.3 we observed that the 'a' and 'c' values are less than the standard values of TiO_2 ($a = 3.785$ Å and $c = 9.514$ Å) $JCPDS$ ($n° 21 - 1272$) which indicate that the stress is compressive for Ta < 550 °C, whilst when Ta $= 600$ °C the lattice constants become greater than the standard values and the stress was converted into depressive correspondingly which leaves some suggests to that the appropriate annealing temperature to prepare a stress-free TiO_2 films is between 550°C and 600°C.

Table IV. 3. Structural parameters.

Annealing temperature ($°C$)	$D(nm)$	Strain ($\varepsilon.10^{-3}$)	Dislocation density ($\delta.10^{11} ligne/cm^2$)	Stress $\sigma\ (GPa)$	Lattice constant a (Å)	Lattice constant c (Å)
400	18,035	1,923	3,075	0,272	3,768	9,301
450	17,500	1,981	3,265	0,280	3,771	9,472
500	19,503	1,778	2,629	0,251	3,780	9,326
550	18,692	1,855	2,862	0,262	3,775	9,410
600	19.488	1,831	2,790	0,259	3,791	9,569

IV. 3. 3. Fourier transform-infrared (FTIR)

Fig IV.12 shows the Fourier transform-infrared absorbance spectra of TiO_2 films which were recorded on a BRUKER VERTEX-80V spectrophotometer. The peak around 445 $cm^{-1}$is assigned to the stretching vibration mode of $Ti-O-Ti$ bond and the peak located around 540 cm^{-1} is assigned to the $Ti-O$ stretching vibration mode. Larbot et al [18] and Chhor et al [19] have divided the range of the low frequencies of TiO_2 $[400-800]$ cm^{-1} to two parts. The first is between $[436-495]$ cm^{-1} which related to the vibration of $Ti-O-Ti$ and $Ti-O$ bonds, the second part is from 550 to 653 cm^{-1} which associated to $Ti-O$ bond. Moreover, we observe that the intensity of the two peaks increases with increasing annealing temperature due the improvement of the crystallization degree which confirms the results obtained from the DRX.

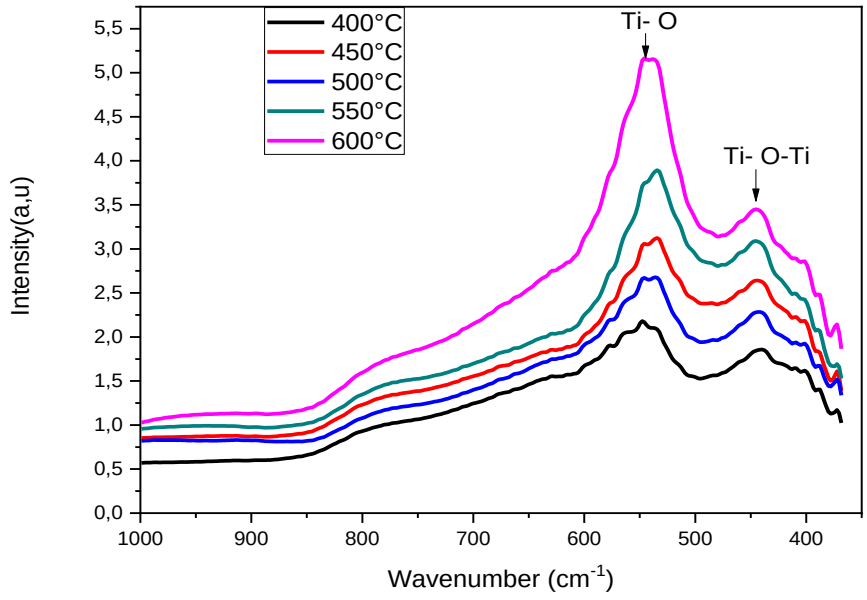

Figure IV. 12. FT-IR absorbance spectra of the annealed TiO_2 thin films.

IV. 3. 4. Optical characterization

Figure IV. 13 represents the transmission and reflection spectra of TiO_2 thin films in the wavelength range of $300-1100$ nm. We note that the films have a high transmittance in the visible region reach to 90 % and they have a very weak transmittance in the UV region close to 0 %, this last is due to the excitation and the migration of the electrons from the valence band to the conduction band. It is observed that the annealing temperature does not significantly affect the transmittance. It may be attributed to the slight variation of crystallinity and the

absence of phase transformation in the grown anatase TiO_2 films, a slight decrease in transmittance is observed with the increase of annealing temperature as can be seen in Fig IV. 11. Saini et al. [20] and Yang et al. [21] also reported the decrease of transmittance with increasing annealing temperature. Also, we note that the reflectance was changed inversely with the transmittance i.e. the top of the transmittance was corresponding to the bottom of the reflectance and vice versa.

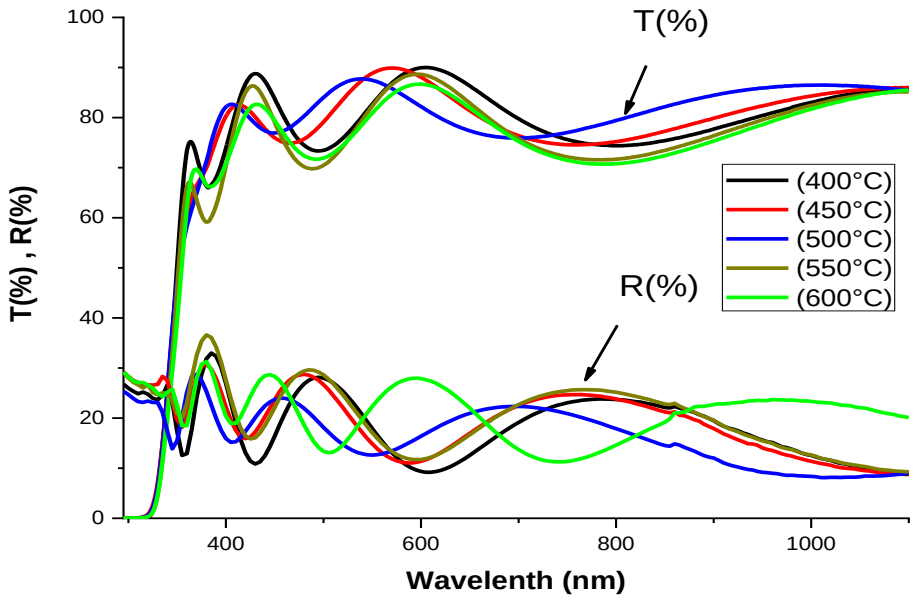

Figure IV. 13. Transmittance and reflectance spectra of annealed TiO_2 thin films.

The refractive index n was calculated at different wavelengths using the (IV.5) relation [22]:

$$n = (1 + R)/(1 - R) + [\,4R/(R-1)^2 - k^{\,2}]^{1/2} \qquad \text{(IV.5)}$$

Where $k = \alpha\lambda/4\pi$ is the extinction coefficient, α is the absorption coefficient and λ is the incident wavelength. Fig IV. 14 manifests the refractive index curves for the films annealed at different temperatures. From Fig IV. 14 and table IV.4 we can see that the value of refractive index of the films at $\lambda = 550\,nm$ close to the value of bulk TiO_2. Also, we note that the refractive index increases with annealing temperatures for $T > 500\,°C$ which found to be $2.10, 2.41$ and 2.79 at $500, 550$ and $600°C$ respectively. The increase may be attributed to higher packing density within the film and a slight increase in crystallization. Hasan et al. [11] also observed an increase in refractive index with annealing temperature in their RF-sputtered annealed films.

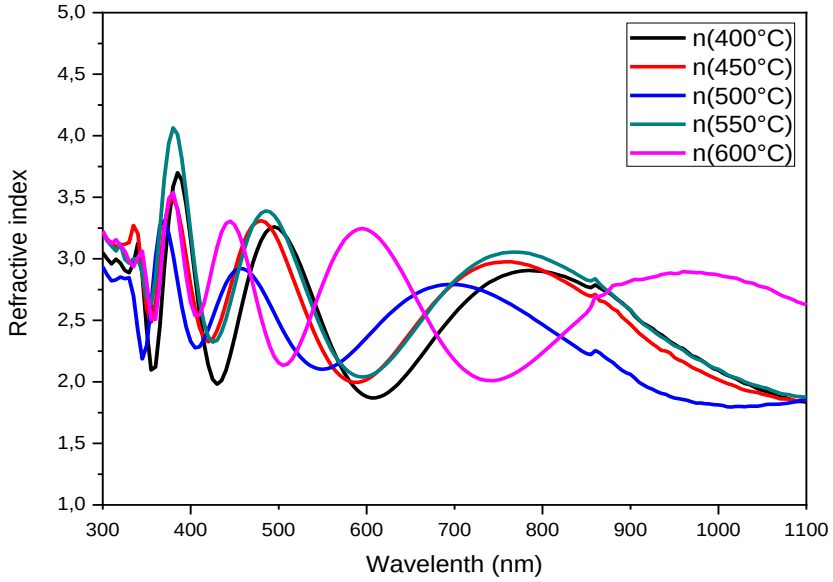

Figure IV. 14. Refractive index variations.

As can be seen from Fig IV. 15 and table IV.4, the direct and indirect band gaps for the annealed films were insignificantly larger than the bulk anatase band gap (3.2 eV). In the other hand, the values deduced in this work are in good agreement with the findings of Hasan et al. [11] and Wang et al. [23]. Also, we note that the optical gaps decrease with the increase of annealing temperature due to the improved crystalline structure of the TiO_2 thin films with annealing temperature [24]. The analogous trend for the direct and indirect optical band gap was reported by Ting et al. [25].

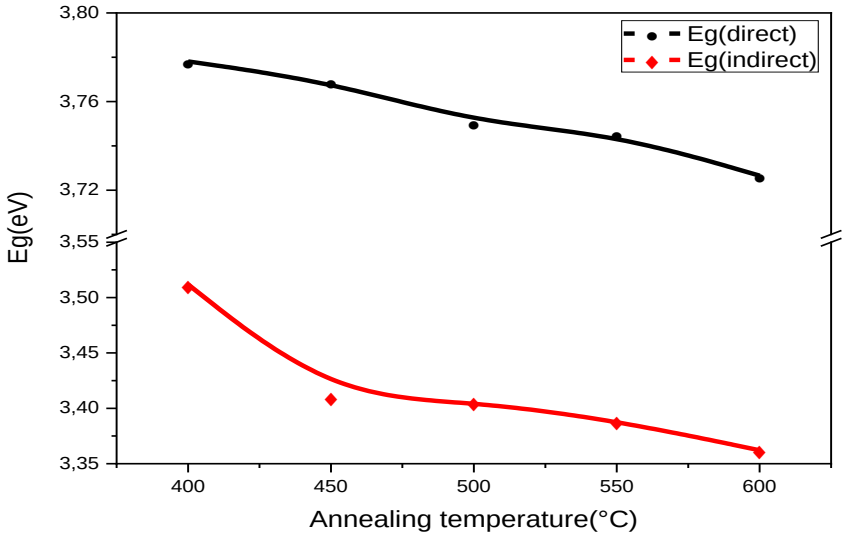

Figure IV. 15. Direct and indirect optical gap Eg as a function of annealing temperature.

Table IV.4. Refractive index n and optical gaps Eg for different Ta.

Annealing temperature ($°C$)	Refractive index n at 550 (nm)	Direct Eg (eV)	Indirect Eg (eV)
400	2,47	3,778	3,512
450	2,25	3,769	3,410
500	2,10	3,751	3,406
550	2,41	3,745	3,389
600	2,79	3,727	3,362

IV. 3. 5. Photoluminescence

Fig IV. 16 presents the photoluminescence spectrum of anatase TiO_2 films annealed at different temperatures, from this figure we can see that there are five interesting emission peaks at 385 (ultraviolet luminescence), $414, 438, 477$ and $524\ nm$ (visible emission). The PL spectra of anatase TiO_2 materials are because of three kinds of physical origins namely self-trapped excitons, oxygen vacancies and surface defects [26].

The visible emission can be attributed to the radiative defects related to the interface traps existing at the grain boundaries and which are emitted from the radiative transition between these levels and valence band. This last can be confirmed by the decrease of the peak's intensities with the decrease of the grain boundary area (increase of crystallite size) [27, 28].

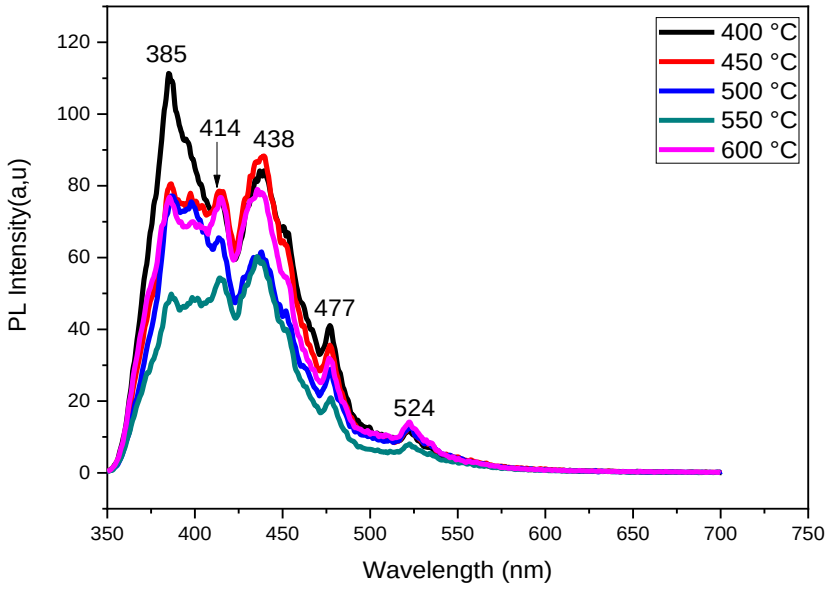

Figure IV. 16. Photoluminescence patterns of TiO_2 thin films.

IV. 4. Molar concentration effect

To study the influence of molar concentration on the TiO_2 thin films properties we changed the molarity from $0.1\ M$ to $0.4\ M$ with the step of $0.05\ M$ and set other parameters.

IV. 4. 1. Thickness variations

The thickness of the films was calculated starting from Swanepoel method. The thickness variations are given below, as Fig IV. 17 shows the film thickness's grow up from 528 to $783\ nm$ as the molar concentration augment from $0.1\ M$ to $0.4\ M$ due to the mount of the material amount in the films.

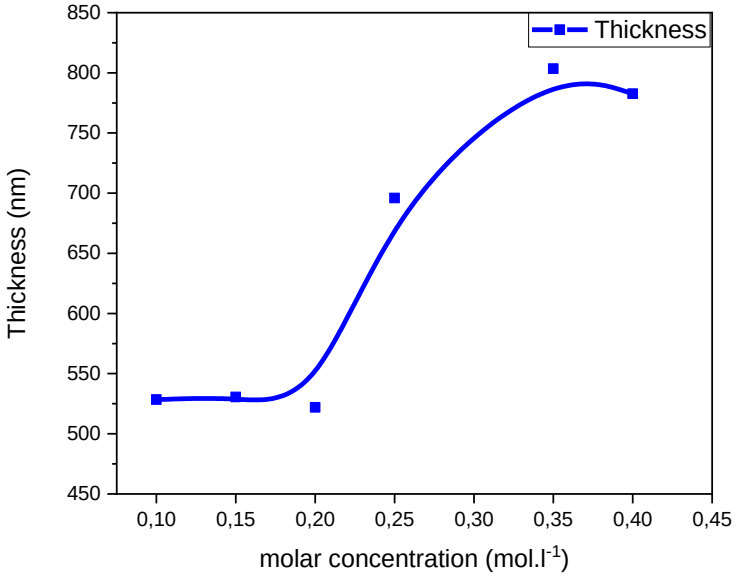

Figure IV. 17. Films thickness's as a function of molar concentration.

IV. 4. 2. Structural characteristics

In this study the utilised diffractometer is a $XPERT-PRO$ with a copper Cu anode having an X-ray beam of wavelength $K_\alpha = 1.54060$ Å. Fig IV. 18 shows XRD patterns of the deposited films which have a polycrystalline structure along to the (101) plane of the anatase phase (accompanied by the presence of some peaks belong to the same phase such as (004) and (200)). As can be seen from this figure the intensity of the (101) peak generally increases with molarity increasing i.e., the increasing molarity improved the TiO_2 crystallinity because of the increase of nucleation sites with a rising amount of the deposited material.

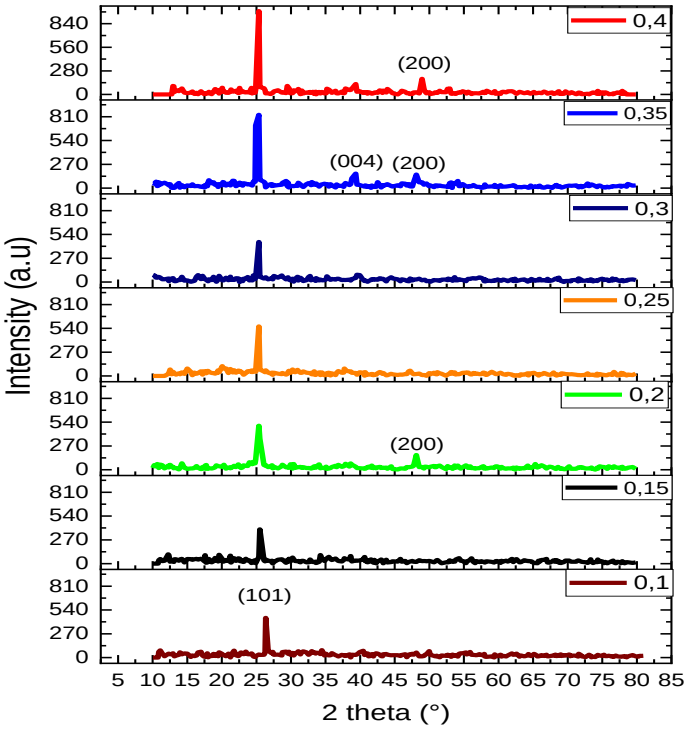

Figure IV. 18. The XRD spectra of TiO_2thin films deposited with different molarities.

The crystallite size D of the films was calculated starting from the full width at half maximum ($FWHM$) of the highest peak (101). In Fig IV. 19 we present the $FWHM$ and D variations, from this figure we can see that the crystallite size growing with the molar concentration from 15.21 nm at 0.1 M to 21.74 nm at 0.4 M due to the increase of nucleation sites with the amount of the deposited material.

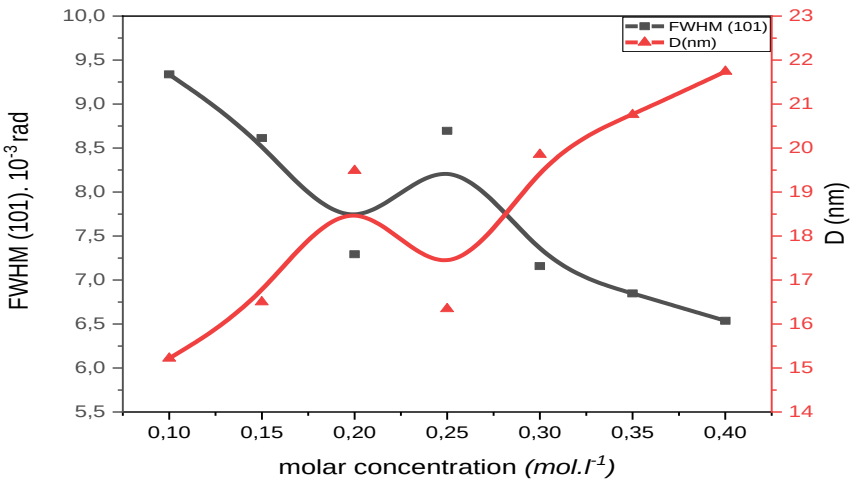

Figure IV. 19. $FWHM$ and crystallite size D as a function of molar concentration.

Fig IV. 20 shows that the strain and the dislocation density are reduced when molarity augmented which can be interpret by the growing of the crystallite size i, e., there is a correlation between increasing crystallite size and decreasing defects such as deformation and dislocation density. The lattice constants 'a' and 'c' were calculated through the relation (IV.4) and given in table IV. 5 from this table we can observe that the 'a' and 'c' values are close to the standard values and they are generally less than the standard values which means that the lattice was exposed to a compressive stress, this last is confirmed by a shift of the peak (101) to a large angle indicates a decrease in the plane spacing d .

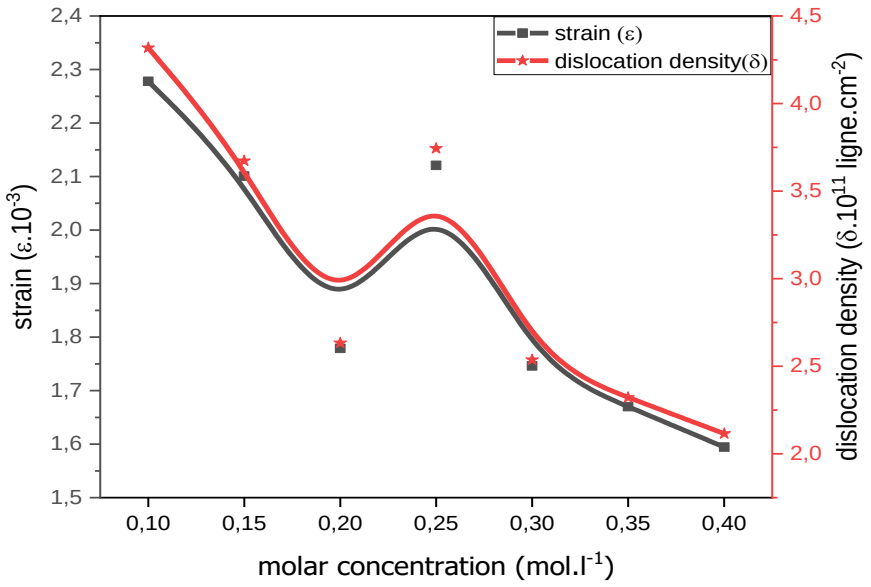

Figure IV. 20. Effect of molar concentration on strain ε and dislocation density δ.

Table IV.5. Structural parameters of TiO_2 thin films.

Molar concentration $(mol.l^{-1})$	Thickness (nm)	Crystallite size $D\ (nm)$	Strain $(\varepsilon.10^{-3})$	Dislocation density $(\delta.10^{11} ligne.cm^{-3})$	Lattice constant a(Å)	Lattice constant c(Å)
0.10	528	15,22	2.28	4.32	3,778	9,723
0.15	530	16,50	2.10	3.67	3,788	9,209
0.20	521	19,49	1.83	2.63	3,780	9,496
0.25	695	16,34	2.12	3.74	3,784	9,400
0.30	519	19,85	1.75	2.54	3,773	9,715
0.35	803	20,76	1.67	2.32	3,782	9,340
0.40	782	21,74	1.59	2.12	3,784	9,461

IV. 4. 3. Optical study

Fig IV. 21 depicts the transmission spectra of TiO_2 thin films in the wavelength domain of $[300 - 1100]\ nm$, from this figure we can recognize the following:

- TiO_2 thin films exhibit a high transmittance in visible range accomplish to 90% and a weakened transmittance in UV region reach to 0% results from the excitation and the migration of the electrons from the valence band to the conduction band.
- Presence of interference fringes which indicates that the films are smooth and uniform [4].
- The transmittance reduces when molarity increases owing to the thickness augmentation (Beer-Lambert low).

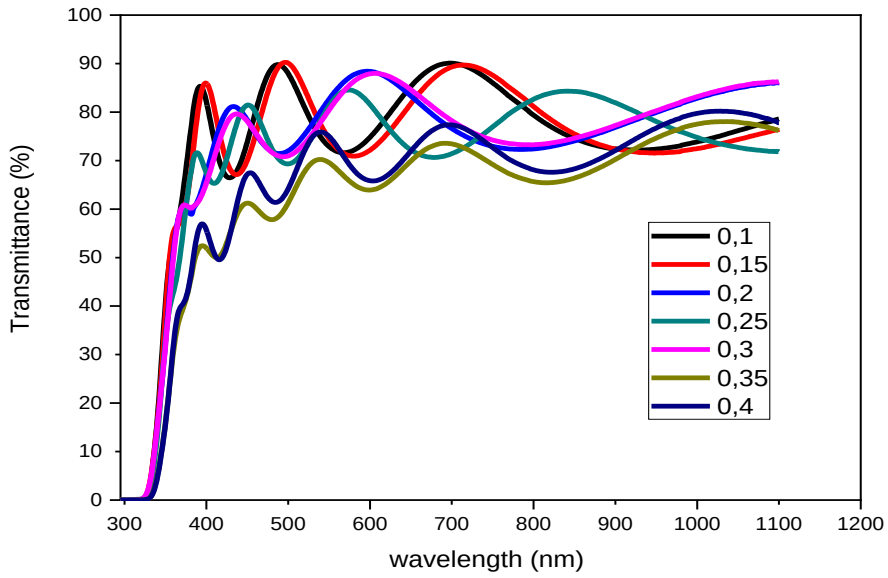

Figure IV. 21. Transmittance spectra of TiO_2 thin films with different molarities.

The direct and indirect gap values were deduced through the procedure explained in paragraph (II. 4. 6. 3) and drawing in fig (IV. 22). The direct and indirect Eg were reduced from 3.73 to 3.66 eV and from 3.39 to 3.25 eV when molarity increased from 0.1 to 0.4 $mol.l^{-1}$, respectively, this reduction resulted from the crystallite growth known as quantum confinement effect [6].

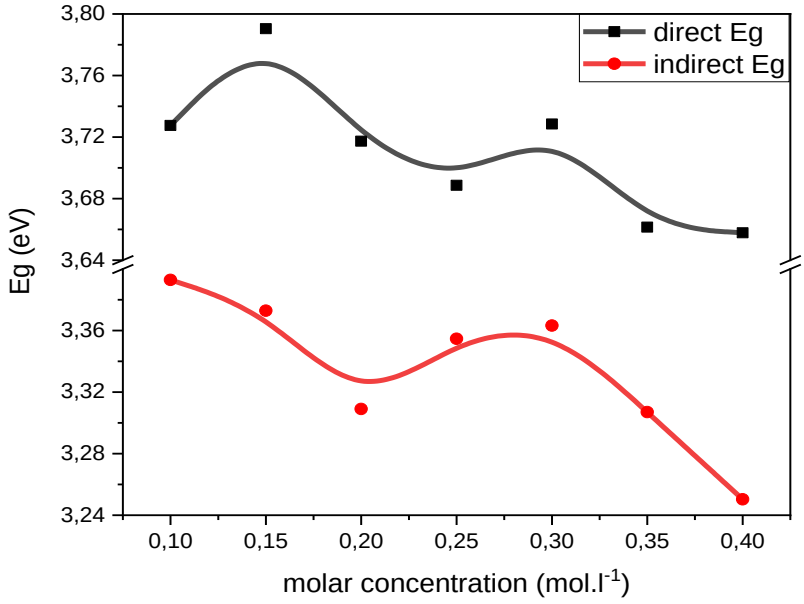

Figure IV. 22. Direct and indirect Eg as functions of molarity.

Disorder or Urbach's (Eu) energy is defined as the bandtailing (electronic states above E_v and below E_c , (see annex D), according to this definition there must be an inverse relationship between E_g and E_u which confirmed by our finding (fig IV. 23).

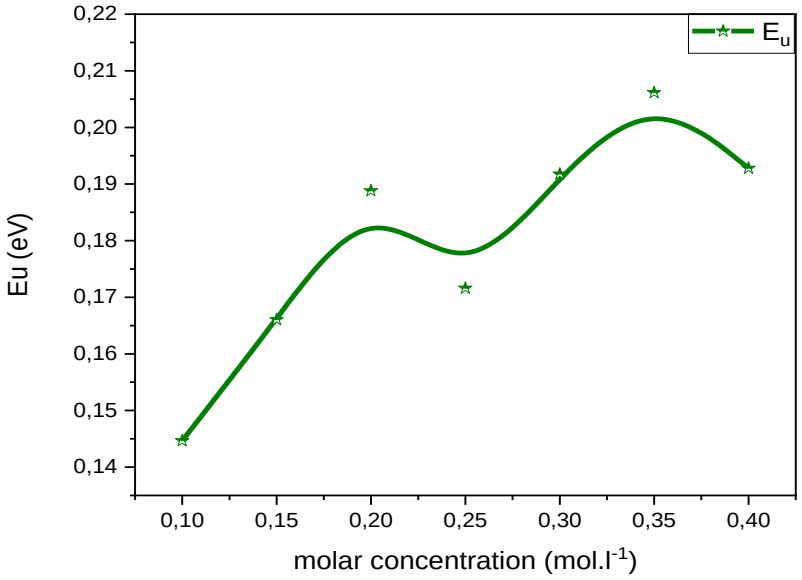

Figure IV. 23. Urbach energy E_u variations.

IV. 4. 4. Photoluminescence

Fig IV.24 exhibits the photoluminescence emission spectrum of the samples, excited at 3.82 eV (325 nm). In all samples the emission peak appears at 3.21 eV (386 nm) is due to phonon assisted indirect transition and the peak at 2.86 eV (434 nm) is assigned to self-trapped exciton (STE). TiO_2 anatase films exhibit oxygen defect related emission peaks at 2.60 eV (477 nm) and 2.37 eV (523 nm) these peaks are ascribed to oxygen vacancies without or with two electrons and oxygen vacancies with one electron respectively.

The non-radiative transition is initiated by defects present on the surface and on the grain boundary [29]. Actually, in a small nanocrystallite the defect formation energy on the grain boundary is less as compared to that in the grain interior or on the surface and thus, there is possibility that defects are accumulated on the amorphous grain boundary and these defects act as non-radiative centers. Nowtony et al. [30] reported that oxygen vacancies are mostly located at the core of the grain boundary and their concentration decreases toward the grain interior. Therefore, the quenching of PL emission in low molar concentration is due to the non-radiative recombination of the charge carriers trapped on the grain boundary oxygen vacancies. Another reason for the low intensity is associated with hopping of electrons from one defect center to the next and then to another and so on, until it finds a recombination center. This process also delays the electron–hole recombination and therefore quenches the PL emission. We have previously mentioned, during structural analysis, that the crystallinity in high molar concentration is improved because of the grain growth and because of the fusion of the grain boundary. As it is mentioned that non-radiative recombination mostly occurs on the grain boundary, removal of this boundary removes the non-radiative defects as well [31].

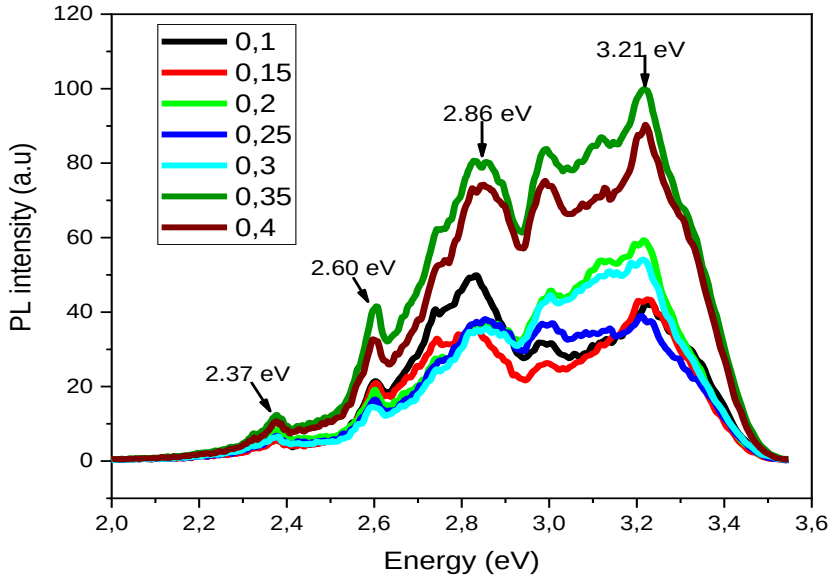

Figure IV. 24. Photoluminescence spectrum of TiO_2 thin films deposited with different molarities.

IV. 5. Effect of Zn doping

Doping of a semiconductor is defined as the addition of a small percentage of foreign atoms in its regular crystal lattice with the intent of producing dramatic changes in its properties (in particular electrical properties). Zinc (Zn) was used as a dopant of the TiO_2 thin films in which the atomic ratio of Zn in the precursor solution had $0, 4, 6$ and 8 at %, where Zinc acetate dehydrate (ZAD) [Zn $(CH_3COO)_2, 2H_2O$] was dissolved into the solution.

IV. 5. 1. Structural characteristics

The X-ray diffractograms of the pure TiO_2 and Zinc doped TiO_2 thin films are shown in Fig IV. 25. The results indicate that all of the films are polycrystalline with a tetragonal structure of anatase TiO_2 and depicts a sharp single phase of anatase peak of (101) plane without the appearance of the secondary phase such as $ZnTiO_3$ i, e., the presence of Zn as doping element behaves as a stabilizing factor of the crystalline structure of anatase TiO_2 by preserving its structure which is agree with finding of F. Huang et al [32]. Moreover, in the Zn doped TiO_2 films the anatase peak (101) become tight and weaker this is due to lack of arrangements caused by doping and also the difference between the ionic radius of Zn^{2+} and Ti^{4+} [33].

Crystallite size D was calculated using the same method mentioned above. As given in table IV.6 and fig IV. 26 the crystallite size slightly increases with Zn concentration. The relatively large crystallite size at 8 % at may be caused by the presence of only (101) peak (absence of the peak (200) compared to the other specimens). The strain, dislocation density, stress and lattice constants were calculated with the relations $(IV.1), (IV.2), (IV.3)$ and $(IV.4)$ respectively, and giving in table IV.6. The results display that the strain was decreased leading to stress decreasing with Zn concentration which may be due to that Zn atoms occupy substitutional positions and not interstitial positions which is confirmed by the approaching of the values of the lattice constants to the pure TiO_2 values.

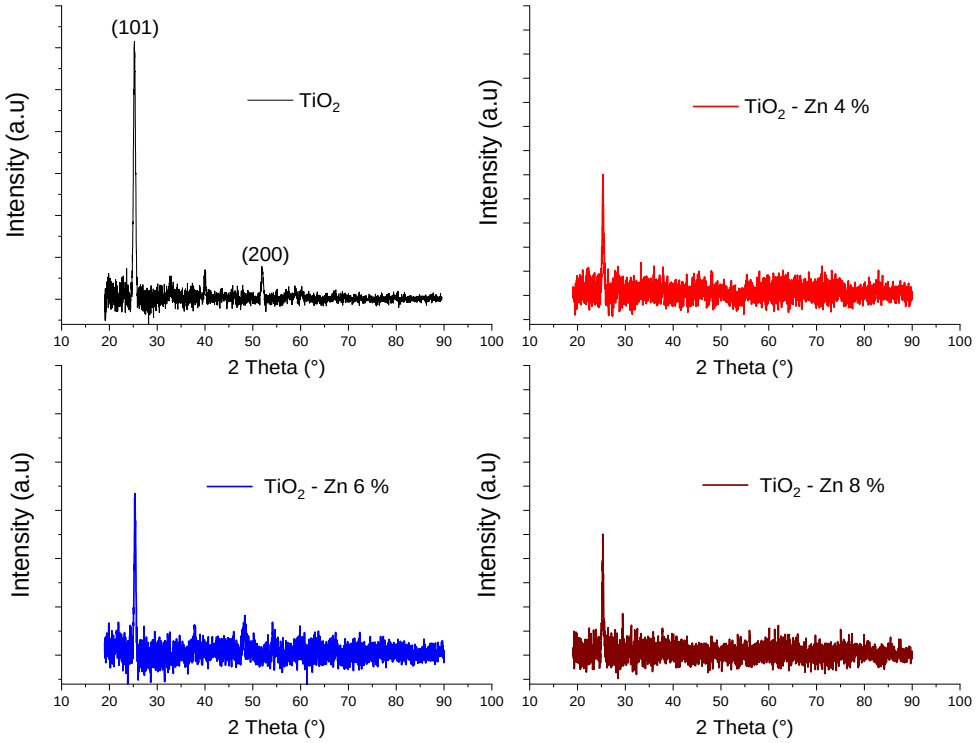

Figure IV. 25. XRD pattern of pure TiO_2 and Zn-doped TiO_2 thin films.

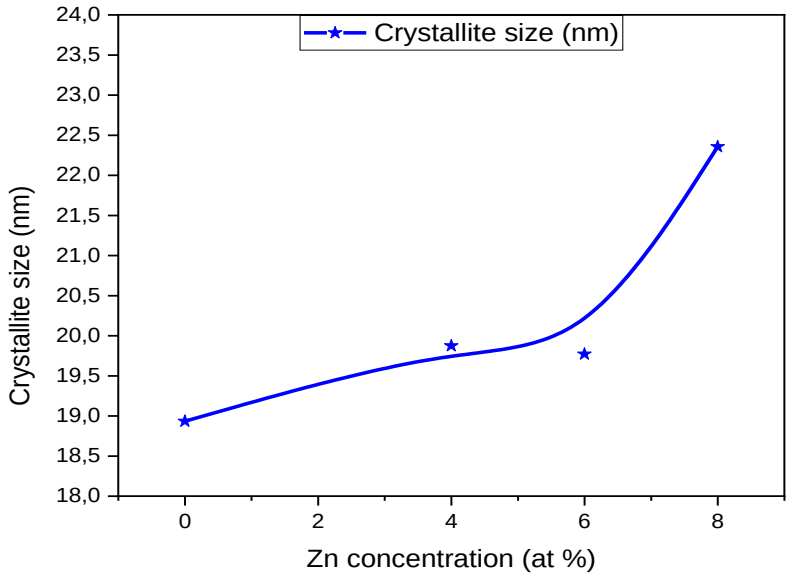

Figure IV. 26. Effect of Zn concentration on crystallite size.

Table IV. 6. Structural parameters values.

Zn concentration $(at\ \%)$	$D(nm)$	Strain $(\varepsilon.10^{-3})$	Dislocation density $(\delta.10^{11} ligne/cm^2)$	Stress $\sigma\ (GPa)$	Lattice constant a (Å)	Lattice constant c (Å)
0	19.488	1,831	2,790	0,259	3,791	9,569
4	19,874	1.744	2.532	0.247	3,786	9,558
6	19,770	1.753	2.558	0,248	3,778	9,649
8	22,356	1.551	2.001	0,219	3,793	9,528

IV. 5. 2. Optical properties

Transmittance spectra of pure TiO_2 and Zn-doped TiO_2 are revealed in fig IV. 27. The transmittance in the visible region for all the films is over $80\ \%$. Moreover, doping concentration did not affect on transmittance almost. The relative high transmittance value for Zn-doped TiO_2 $(8\ at.\%)$ is attributed to the large crystallite size (decrease in scattering centers).

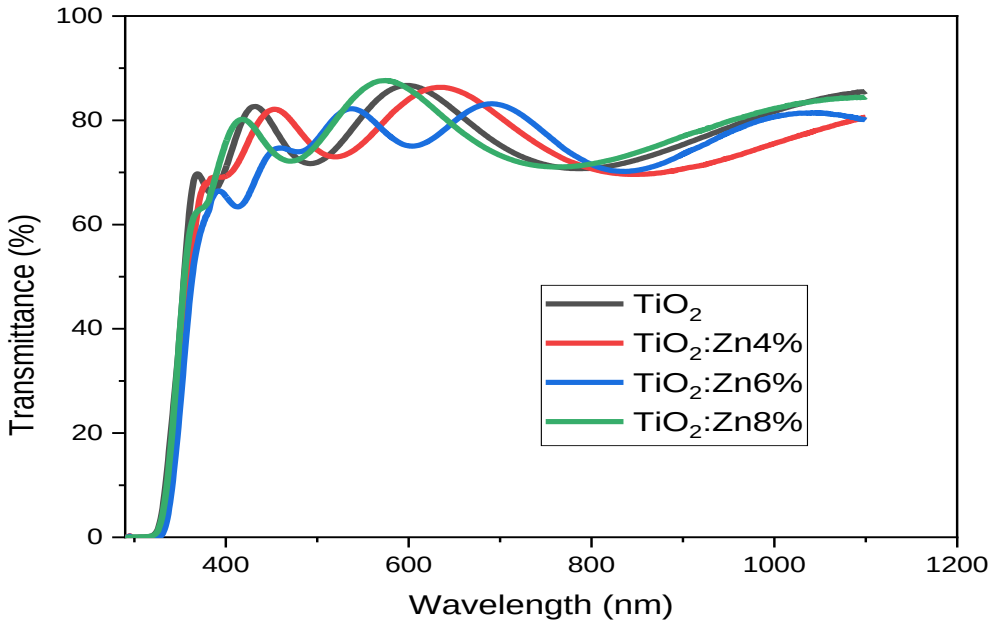

Figure IV. 27. Optical transmittance of pure TiO_2 and Zn-doped TiO_2 thin films.

The optical band gaps (direct and idirect) were calculated through the method described earlier and were illustrated in fig IV.28. The band gaps of the films remained greater than the bulk anatase band gap and they were reside nearly constants even after doping with Zn which may interpreted by insignificants structural changes.

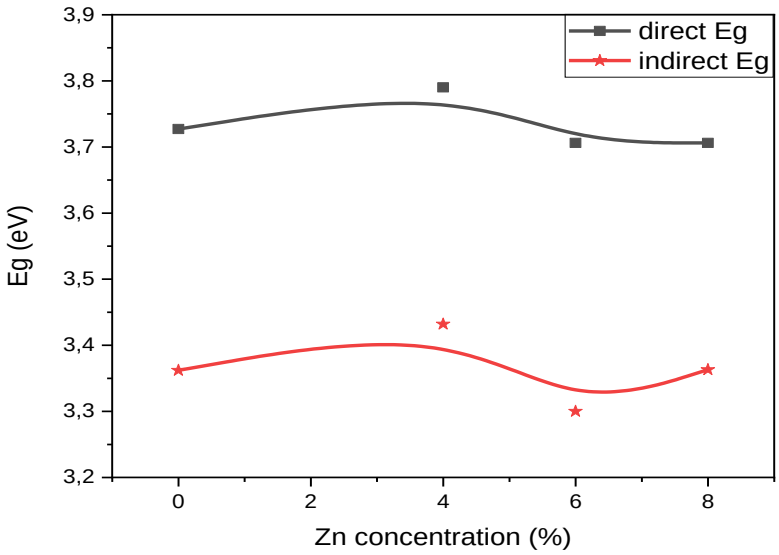

Figure IV. 28. Direct and indirect band gap of pure TiO_2 and Zn-doped TiO_2 thin films.

IV. 5. 3. Electrical conductivity

The electrical conductivity was measured via four-point probe method (see paragraph II. 4. 5), using this technique we could not determine the conductivity value of the undoped TiO_2 films due to its low value. As fig IV.29 depicts the conductivity was increased to $6 \times 10^{-4}\ (\Omega.cm)^{-1}$ for $8\ at.\%$ Zn-doped TiO_2 which is due to grain boundary decrease leading to increase in electron mobility from grain to grain [17].

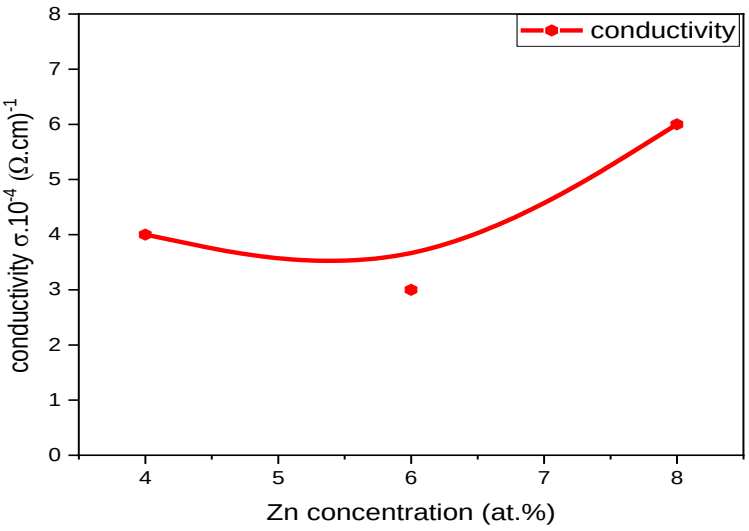

Figure IV. 29. Conductivity variations.

References

[1] M. Ohring, *"Materials Science of Thin Films Deposition and Structure"*, 2nd Edition, Academic Press, (2002).

[2] H. Berger., H. Tang and F. Lévy, *"Growth and Raman spectroscopic characterization of TiO_2 anatase single crystals"*, Journal of Crystal Growth 130 (1-2), (1993) 108-112.

[3] J, Medina-Valtierra., M, Sánchez-Cárdenas., C, Frausto-Reyes and Sergio Calixto, *"Formation of smooth and rough TiO_2 thin films on fiberglass by sol-gel method"*, Journal of Mexican Chemistry Society, 50 (1), (2006), 8-13.

[4] M. Jlassi., I. Sta., M. Hajji and H. Ezzaouia, *"Effect of nickel doping on physical properties of zinc oxide thin films prepared by the spray pyrolysis method"*, Applied Surface Sciences, 301 (2014) 216-224.

[5] Y. Gao., Y. Masuda., Z. Peng., T. Yonezawa and K. Koumoto, *"Room temperature deposition of a TiO_2 thin film from aqueous peroxotitanate solution"*, Journal of Materials Chemistry, 13 (3), (2003) 608–613.

[6] A. Mosbah., S. Abed., N. Bouhssira., M. S. Aida and E. Tomasella, *"Preparation of highly textured surface ZnO thin films"*, Materials Science and Engineering B 129 (1-3), (2006) 144–149.

[7] A. Suisalu., J. Aarik., H. Mändar and I. Sildos, *"Spectroscopic study of nanocrystalline TiO_2 thin films grown by atomic layer deposition"*, Thin Solid Films, 336 (1-2), (1998) 295-298.

[8] B. Choudhury and A. Choudhury, *"Oxygen defect dependent variation of band gap, Urbach energy and luminescence property of anatase, anatase–rutile mixed phase and of rutile phases of TiO_2 nanoparticles"*, Physica E: Low-Dimensional Systems and Nanostructures, 56, (2014) 364–371.

[9] K. Sahbeni., I. Sta., M. Jlassi., M. Kandyla., M. Hajji., M. Kompitsas M and W. Dimassi, *"Annealing Temperature Effect on the Physical Properties of Titanium Oxide Thin Films Prepared by the Sol-Gel Method"*, J Phys Chem Biophys, 7(257), (2017) 2161-0398.

[10] P. Charles and Jr. Poole, *"Encyclopedic dictionary of condensed matter physics"*, Volume 1, Department of Physics and Astronomy, University of South Carolina, Columbia, SC, USA, (2004).

[11] M. M. Hasan., A. S. M. A. Haseeb., R. Saidur., H. H. Masjuki and M. Hamdi, *"Influence of substrate and annealing temperatures on optical properties of RF-sputtered TiO_2 thin films"*, Optical Materials, 32 (6), (2010) 690-695.

[12] B. Stefanov and L. Österlund, *"Tuning the Photocatalytic Activity of Anatase TiO_2 Thin Films by Modifying the Preferred <001> Grain Orientation with Reactive DC Magnetron Sputtering"*, Coatings, 4 (3), (2014) 587-601.

[13] M. F. Malek., M. H. Mamat., M. Z. Musa., Z. Khusaimi., M. Z. Sahdan., A. B. Suriani and M. Rusop, *"Thermal annealing-induced formation of ZnO nanoparticles: Minimum strain and stress ameliorate preferred c-axis orientation and crystal-growth properties"*, Journal of Alloys and Compounds, 610 (2014) 575-588.

[14] I. B. Kherkhachi., A. Attaf., H. Saidi., A. bouhdjar., H. Bendjdidi., Y. Benkhetta., R. Azizi and M. S. Aida, *"Structural, morphological, optical and electrical characterization of spray ultrasonic deposited SnS_2 thin film"*, Optik, 127 (4), (2016) 2266–2270.

[15] G. K. Williamson and R. E. Smallman, *"III: Dislocation densities in some annealed and cold-worked metals from measurements on the X-ray debye-scherrer spectrum"*, Philosophical Magazine, 1(1), (1956) 34-46.

[16] V. K. Jain and A. Verma, *"Physics of Semiconductor devices"*, 17th International workshop on the physics of semiconductor devices, Springer science and business Media, (2013).

[17] A. Arunachalam., S. Dhanapandian., C. Manoharan and G. Sivakumar, *"Physical properties of Zn doped TiO_2 thin films with spray pyrolysis technique and its effects in antibacterial activity"*, Spectrochimica Acta Part A: Molecular and Biomolecular Spectroscopy 138, (2015) 105–112.

[18] A. Larbot., I. Laaziz., J. Marignan and J. F. Quinson, *"Porous texture of a titanium oxide gel: evolution as a function of medium used"*, Journal of Non-Crystalline Solids, 147 (1992) 157-161.

[19] K. Chhor, J. F. Bocquet and C. Pommier, *"Syntheses of submicron TiO_2 powders in vapor, liquid and supercritical phases, a comparative study"*, Materials chemistry and physics, 32(3), (1992) 249-254.

[20] K. K. Saini., S. D. Sharma., M. Kar, D. Singh and C. P. Sharma, *"Structural and optical properties of TiO_2 thin films derived by sol–gel dip coating process"*, Journal of non-crystalline solids, 353(24-25) (2007) 2469-2473.

[21] C. Yang., H. Fan., Y. Xi., J. Chen and Z. Li, *"Effects of depositing temperatures on structure and optical properties of TiO_2 film deposited by ion beam assisted electron beam evaporation"*, Applied Surface Science 254(9), (2008) 2685-2689.

[22] M. M. El-Nahass., A. A. Atta., H. E. A. El-Sayed and E. F. M. El-Zaidia, *"Structural and optical properties of thermal evaporated magnesium phthalocyanine (MgPc) thin films"*, Applied Surface Science, 254(8), (2008) 2458-2465.

[23] T. M. Wang., S. K. Zheng., W. C. Hao and C. Wang, *"Studies on photocatalytic activity and transmittance spectra of TiO_2 thin films prepared by RF magnetron sputtering method"*, Surface and Coatings Technology, 155(2-3), (2002) 141-145.

[24] J. P. Mathew., G. Varghese and J. Mathew, *"Effect of post-thermal annealing on the structural and optical properties of ZnO thin films prepared from a polymer precursor"*, Chinese Physics B, 21 (7), (2012) 078104.

[25] C. C. Ting, S. Y. Chen and D. M. Liu, *"Structural evolution and optical properties of TiO_2 thin films prepared by thermal oxidation of sputtered Ti films"*, Journal of Applied Physics, 88 (8), (2000) 4628-4633.

[26] P. Singh and D. Kaur, *"Room temperature growth of nanocrystalline anatase TiO_2 thin films by dc magnetron sputtering"*, Physica B: Condensed Matter, 405 (5), (2010) 1258-1266.

[27] T. S. Senthil., N. Muthukumarasamy., R. Balasundaraprabhu and C. S. Kumaran., *"Structural and Photoluminescence Properties of Sol-gel Spin Coated Nanocrystalline TiO_2 Films"*, J. Nanosci. Nanotechnol, 1(1), (2012) 6-9.

[28] A. K. Tripathi., M. K. Singh., M. C. Mathpal., S. K. Mishra and A. Agarwal, *"Study of structural transformation in TiO_2 nanoparticles and its optical properties"*, Journal of Alloys and Compounds, 549, (2013) 114-120.

[29] Y. G. Wang., S. P. Lau., X. H. Zhang, H. H. Hng, H. W. Lee., S. F. Yu and B. K. Tay, "Enhancement of near-band-edge photoluminescence from ZnO films by face-to-face annealing", Journal of Crystal Growth, 259(4), (2003) 335-342.

[30] J. Nowotny., T. Bak., T. Burg., M. K. Nowotny and L. R. Sheppard, "Effect pf grain boundaries on semiconducting properties of TiO_2 at elevated temperatures", Journal of Physical Chemistry C, 111(27), (2007) 9769-9778.

[31] C. Tsakonas., W. Cranton., F. Li., K. Abusabee., A. Flewitt, D. Koutsogeorgis and R. Ranson, *"Intrinsic photoluminescence from low temperature deposited zinc oxide thin films as a function of laser and thermal annealing"*, Journal of Physics D: Applied Physics 46(9), (2013) 095305.

[32] F. Huang., Qi. Li., G. J. Thorogood., Y. B. Cheng and R. A. Caruso, *"Zn-doped TiO_2 electrodes in dye-sensitized solar cells for enhanced photocurrent"*, Journal of Materials Chemistry, 22(33), (2012) 17128–17132.

[33] N. B. Abdollahi., S. Sanjabi and V. Ahmadi, *"Optical and photocatalytic characteristics of nitrogen doped TiO_2 thin film deposited by magnetron sputtering"*, Transaction F: Nanotechnology, 17(2), (2010) 102–107.

Chapter V
ZnO thin films characterisation (results and discussion)

V. 1. Introduction

The aim of this part is to obtain ZnO thin films with suitable properties for photovoltaic applications i. e., the films should be well crystallized, have a high transparence in the visible region and it should have high conductivity value, thus, it is necessary to optimize the elaboration conditions such as the nature of stabilizer and annealing temperature…

This chapter is consecrated to analysis the deposited films using the characterization tools mentioned in the paragraph (II.4), we were also interested in the study of the transformation of their properties with the variation of the following parameters:

- The nature of the stabilizer.
- Annealing temperature.
- Amount of Ga doping.

Table V. 1. A summary table of the experimental conditions of ZnO thin films deposition.

Nature of stabilizer	Annealing temperature ($°C$)	Molar concentration ($mol.L^{-1}$)	Amount of doping $Ga(at.\%)$
Acetylacetone ($AcAc$)	600	0.6	0
Hydrochloric acid (HCl)			
$Monoethanolamine$ (MEA)			
$Monoethanolamine$ (MEA)	300	0.6	0
	400		
	500		
	600		
Acetylacetone ($AcAc$)	600	0.6	0
			0.67
			1.33
			2.00
			2.67
			3.33

V. 2. Stabilizer effect on the properties of Zinc Oxide thin films

The three stabilizers used in this series are belonging to three different chemical groups which are: ketones (Acetylacetone), amines (Monoethanolamine) and acids (HCl), the effect of these three stabilizers on the ZnO films is given as follows:

V. 2. 1. Structural study

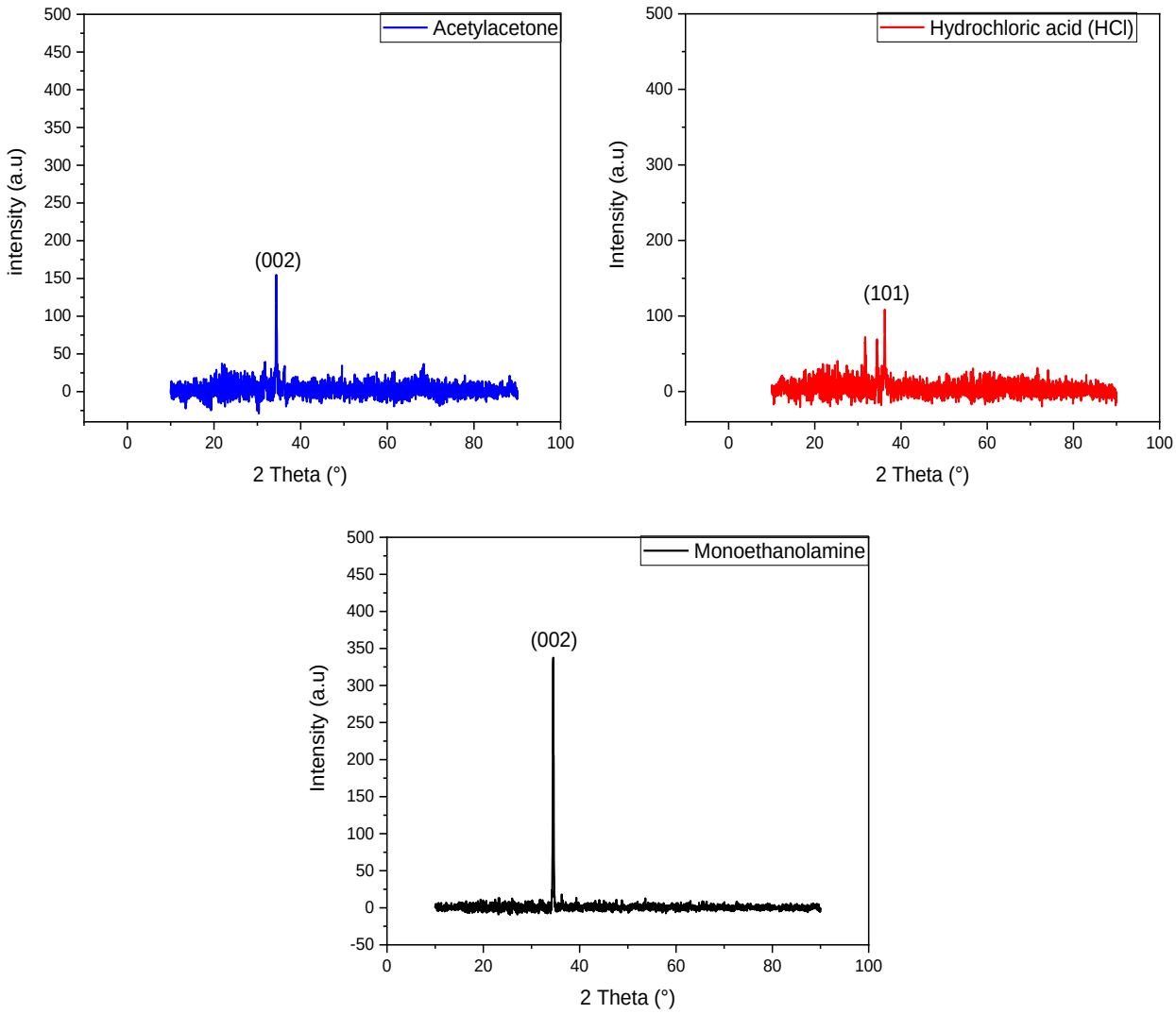

Figure V. 1. X ray patterns of ZnO thin films prepared with different stabilizers.

XRD patterns were obtained thru $Mini - Flex\ (Rigaku)$ diffractometer with a copper anode having a wavelength $\lambda_{k\alpha}(Cu) = 1.5405$ Å and were presented in fig V. 1 , it is observed that the elaborated ZnO films are polycrystalline with hexagonal wurtzite phase according to JCPDS (36-1451), the highest peak is assigned to the (002) plane in the samples prepared using monoethanolamine and acetylacetone as stabilizers, while the films prepared

with HCl growth along to the (101) plane which means that the type of stabilizer determine the growth orientation. The crystallite size D of the films was calculated using Scherre's formula, as showed in table V. 2 and fig V. 2 the D had some differences for the different used stabilizers where it had the large crystallite size in the films deposited with MEA.

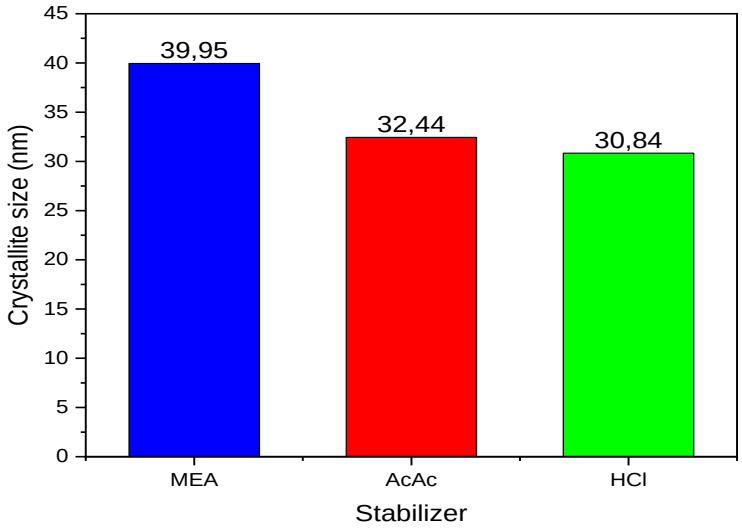

Figure V. 2. Crystallite size of ZnO thin films deposited using different stabilizers.

Both lattice parameters 'a' and 'c' within the hexagonal compact phase are calculated via the (002) orientation using the relation (V.1):

$$1/d^2 = 4/3((\mathrm{h}^2 + \mathrm{hk} + \mathrm{k}^2)/a^2) + l^2/c^2 \qquad \text{(V.1)}$$

It is worth noticing that the films prepared with MEA stabilizer have the values of the parameters a and c about 3.248 Å and 5.203 Å respectively which almost equal to the reported ones in $JCPDS$ standard data $a_0 = 3.249$ Å and $c_0 = 5.206$ Å , the slightly lower values of a c than the standard ones interpreted by the compressive stress applied on the films. Although, the films prepared by $AcAc$ and HCl had a lattice parameters higher than the standard ones and present a depressive stress.

Table V. 2. Structural parameters of ZnO thin films.

Stabilizer	***2theta*** (°)		***Crystallite size D (nm)***	***Lattice parameter c*** (Å)	***σ (Gpa)***
	(002)	**(101)**			
MEA	34,51	36.28	39.95	5,203	0,269
$AcAc$	34,37	/	32.45	5,218	−1,078
HCl	34,45	36,23	30.84	5,212	−0,410

V. 2. 2. Fourier transform-infrared (FTIR)

Fig V. 3 depicts the $FT-IR$ spectrum of the specimens, extended from 400 cm^{-1} to 4000 cm^{-1}, from this figure we can perceive that all the films present a two vibrations peaks at 570 cm^{-1} and 802 cm^{-1} which were assigned to $Zn-O$ and $Si-O$ liaison respectively, this last is come from the substrate. Moreover, the MEA films present a peak at 1126 cm^{-1} which assigned to the stretching mode of $C-N$ liaison in the MEA stabilizer [1]. The symmetric bending of $O-H$ liaison was appeared at 1273 cm^{-1} in $AcAc$ and HCl films.

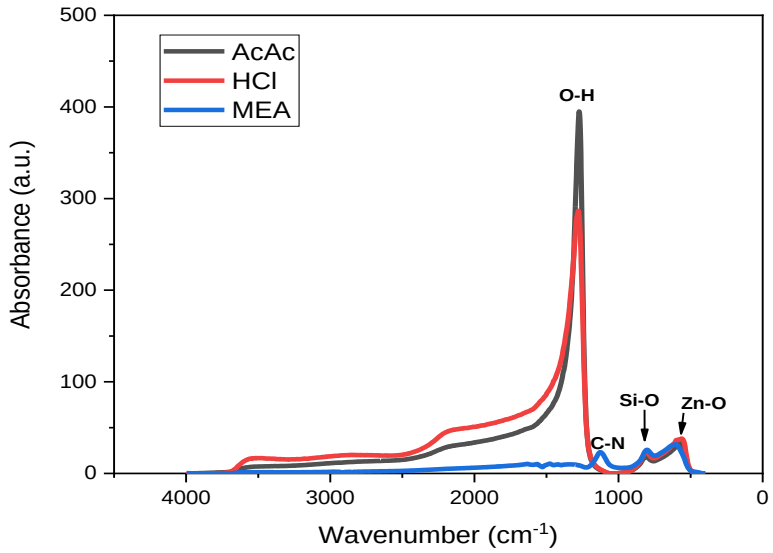

Figure V. 3. FT-IR absorbance spectra of ZnO thin films deposited with different stabilizers.

V. 2. 3. Optical study

The transmittance spectra of the films are presented in fig V.4, as can be seen from this figure the films deposited using MEA and $AcAc$ exhibit a high transmittance value upto 85 % in the visible range, in contrast the films deposited using HCl as a stabilizer have a low transmittance amount less than 40 %, which affirm that the HCl is not suitable to prepare a ZnO thin films with high transmittance. Furthermore, there is an abrupt decay in the films prepared with HCl and MEA, in contrary, for the $AcAc$ stabilizer the films have two absorption edges around 310 and 380 nm which may be attributed to the low thickness for this specimen.

The band gap of the prepared films was calculated using the Tauc relationship, the Eg values are given in fig V. 5 where the nature of stabilizer defines the Eg value, the ZnO films with MEA and $AcAc$ have a gap close to the bulk one which is equal to 3.27 eV, whereas HCl yield to a ZnO thin films with a gap significantly higher than the bulk one (around 3.94 eV) due the quantum confinement effect.

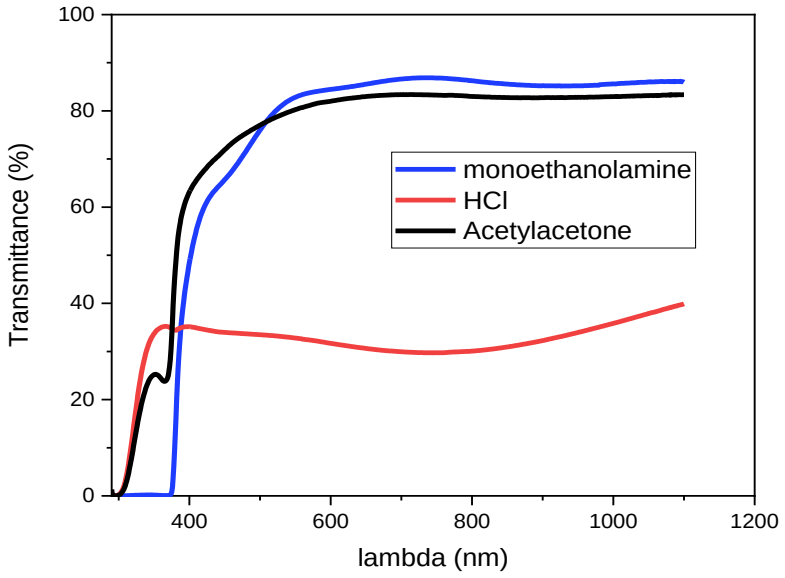

Figure V. 4. Transmittance spectra of ZnO thin films prepared using different stabilizers.

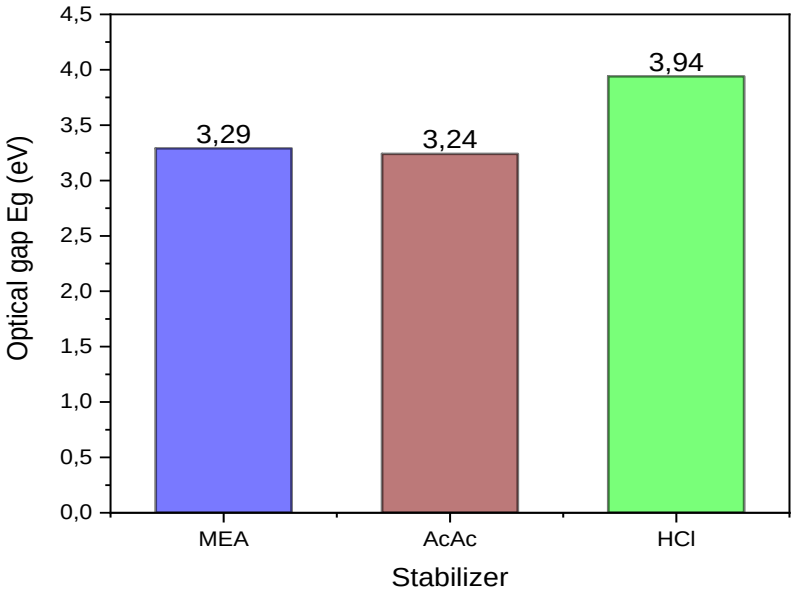

Figure V. 5. Effect of type of stabilizer on optical gap.

V. 2. 4. Photoluminescence studies

The room temperature PL spectra are given in fig V. 6. Zinc Oxide thin films were excited at $320\ nm$. The PL spectra exhibit two ultraviolet (UV) emission bands prevailing for all films whatever the sol stabilizer used for their preparation, the first was centred around $\sim 363\ nm$ and the second was appeared at $390\ nm$ for MEA and HCl then it was shifted to $376\ nm$ for $AcAc$, UV emission is known as a near-band-edge (NBE) emission, which attributed to the radiative recombination of excitons during their transition from localized level near the condition band to the valence band [2]. The violet emission band observed in all the samples between 420 and $460\ nm$ is attributed to the presence of zinc interstitials (Zn_i) shallow donors, which have a $0.22\ eV$ energy gap below the conduction band (see Fig V. 7). Exciton recombination between the electrons localized at the zinc interstitials and holes in the valence band leads to this violet emission. This type of violet emission band was also observed in the ZnO nanoneedle arrays reported by [3]. A broad green emission band (between 505 and $535\ nm$) was showed in the films prepared with $AcAc$ and HCl, known as a deep-level emission, is related to the deep-level defect states [4]. This green emission originates from the recombination of a photo-generated hole with an electron, occupying the oxygen vacancy and interstitials of zinc, respectively. In addition, we must be noticed that for $AcAc$ samples all the emission peaks are higher than the peaks of other stabilizers.

As a result, the present PL study infers that the type of stabilizer has high impact on the luminescence property of the ZnO sample.

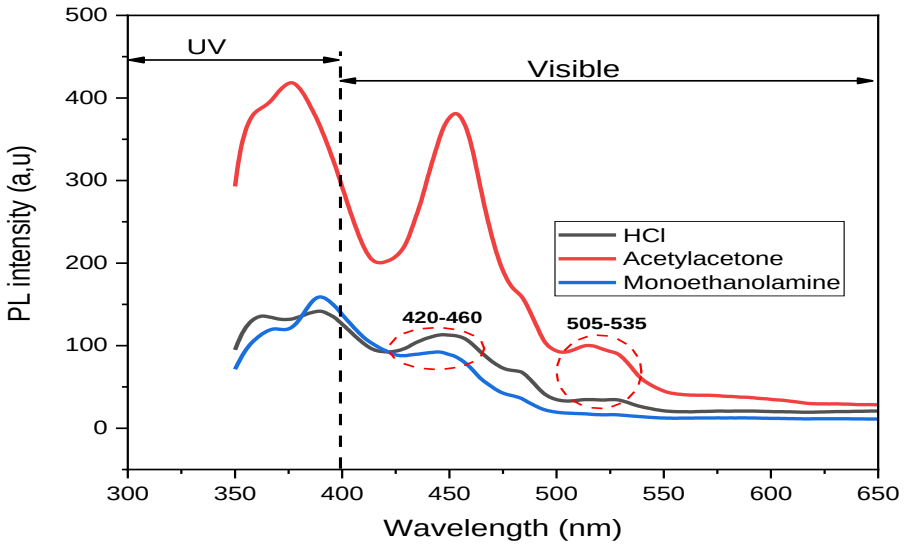

Figure V. 6. Room temperature PL spectra of ZnO thin films.

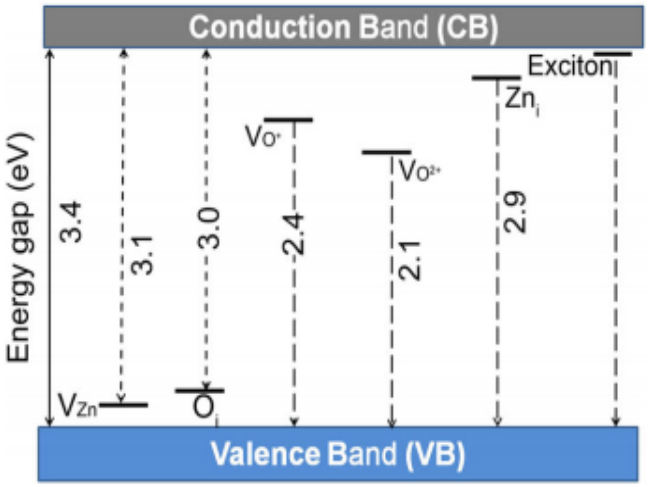

Figure V. 7. Schematic illustration of different defect levels in ZnO, which are responsible for the emission of different wavelengths [5].

V. 3. Effect of annealing temperature on ZnO properties

As given in table V. 1 the annealing temperature has $300, 400, 500$ and $600\ °C$, the effect of T_a on the deposited films was studied using XRD, $UV-VIS$ spectroscopy and two-point probe method.

V. 3. 1. Structural characteristics

The structural characterization is carried out by a ($Bruker\ D8\ Advance$) diffractometer with copper anode having an X-ray beam of wavelength $K_\alpha\ (Cu) = 1.5418$ Å. Fig V. 8 shows the XRD spectra of ZnO for different annealing temperatures. By comparing the peaks of the samples with $JCPDS$ $(36-1451)$ library, it was found that the material observed is ZnO polycrystalline. The intensity of the highest peak assigned to the preferential orientation (002) plane which indicating that the structure is Wurtzite. L. Znaidi [6] proposed that the (002) orientation appears to be favored by amorphous substrates such as glass. However, Takahashi et al. [7] reported that the preferential orientation according to c-axis perpendicular to the substrate due to the using of zinc acetate dehydrate as precursor which is consisting with our results. In the other hand Lee et al. [8] said that the growth of ZnO thin films along the (002) plane owing to the low surface free energy of this plane. Also, it is interesting to note that the intensity of (002) peak gradually increases with the increasing annealing temperature i.e. the increasing annealing temperature caused the crystallinity of ZnO to enhance which is agree with the result obtained by Y. Zhang et al [9].

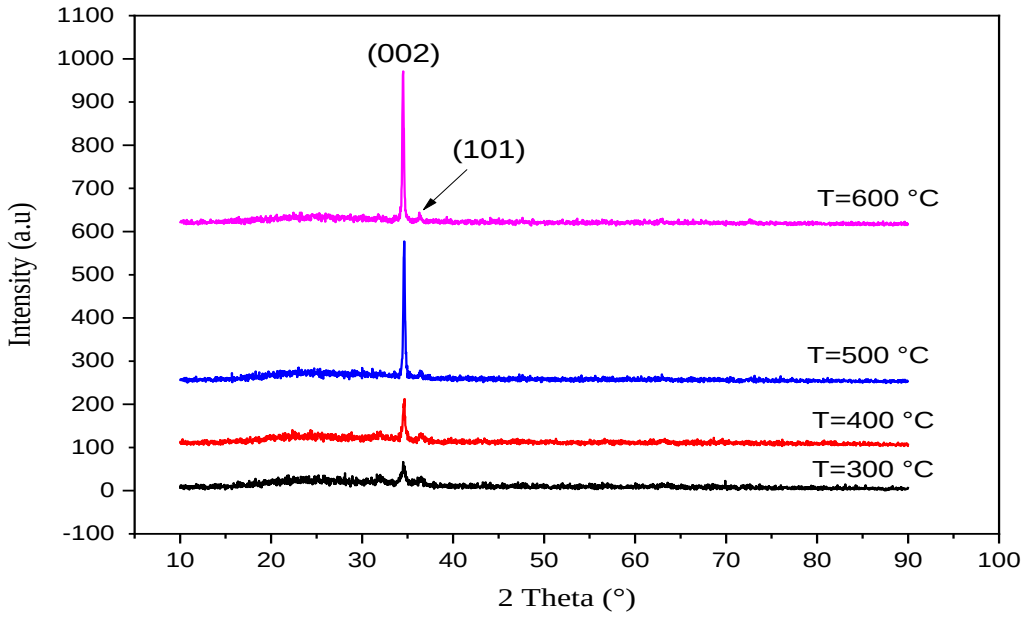

Figure. V. 8. X-ray diffraction patterns of ZnO thin films, for different annealing temperatures.

The crystallite size D of the various ZnO films was calculated starting from the full width at half maximum ($FWHM$) of the peak (002). We have calculated D using Scherrer's formula. The results are illustrated in table V. 3. Using these results, we draw the variation of the crystallite size as a function of annealing temperature which is represented in the fig V. 9.

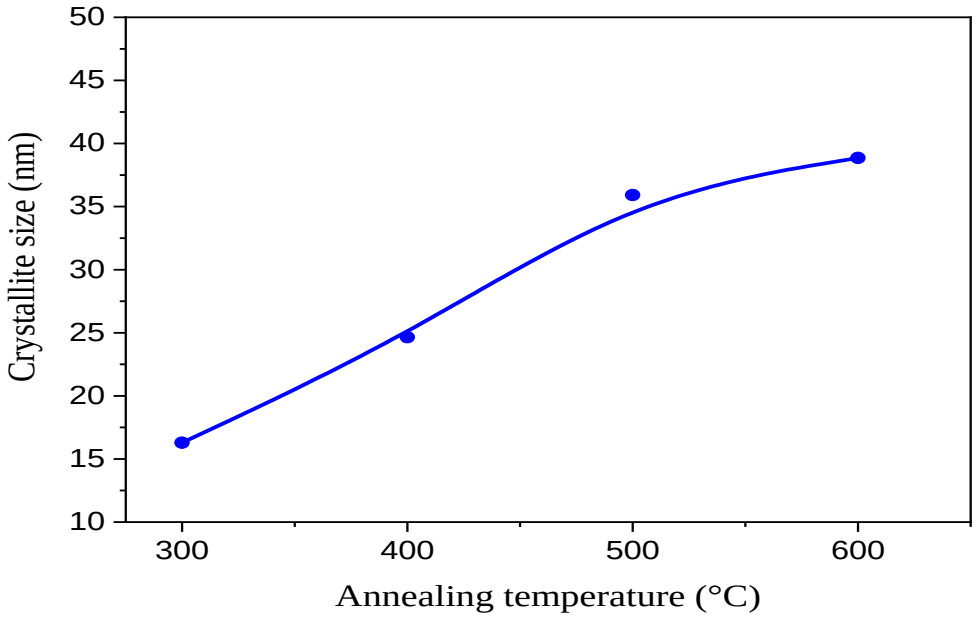

Figure. V. 9. The crystallite size as a function of annealing temperature.

We observe that the crystallite size grows with the annealing temperature from ~16 nm to ~39 nm since when the film atoms obtain enough energy in the annealing process they will migrate and restructure into thin films. The crystallites then grow larger correspondingly [10]. The stress σ values of the diverse ZnO thin films were calculated using the following relations [11, 12]:

$$\sigma = [2C_{13} - (C_{11}+C_{12})C_{33}^{film}/C_{13}]. \varepsilon \quad (V.2)$$

With: $$C_{33}^{film} = 0.99\, C_{33}^{cristal}/(1-\varepsilon)^4 \quad (V.3)$$

And: $$\varepsilon = (c^{film} - c^{bulk})/c^{bulk} \quad (V.4)$$

Where ε is the strain, and C_{ij} are elastics constants, for example for ZnO: C_{11}, C_{12}, C_{13} and $C_{33}^{cristal}$, the values are 209.7, 121.1, 105.1 and 210.9 GPa respectively [13]. The results are illustrated in table V. 3, and fig V. 10. The internal stress increases between 300°C and 500°C then it decreases at 600°C and take its weakest value at this temperature

which is interpreted by the increase of the crystallite size with the elevating of the annealing temperature. Further, the positive sign indicate that the biaxial stress is compressive [14]. The c axis lattice parameter of the various ZnO thin films was calculated using the relation (V.1).

Fig V. 10 shows the variation of the value of the lattice parameter c. The value of the lattice parameter of the film annealed at $300°C$ is 5.190 Å. Then it diverge from the c value of the stress-free lattice (c^{bulk} = 5.206 Å, $JCPDS$ no 36-1451) and takes 5.183 Å for the film annealed at $400°C$ and 5.177 Å for the film annealed at $500°C$ this can be interpreted by the presence of the intermediate zinc copolymer such as $Zn_4O(COOCH_3)_6$ and $ZnNH(C_2H_4O)_2$ during the reaction of forming ZnO which disturb the crystallization and give the film a less chance to be structurally relaxed [15, 16]. On the other hand, when the annealing temperature is high ($Ta = 600°C$) the film is given an enough energy to be structurally relaxed as a result of disappearing of the intermediate zinc copolymer.

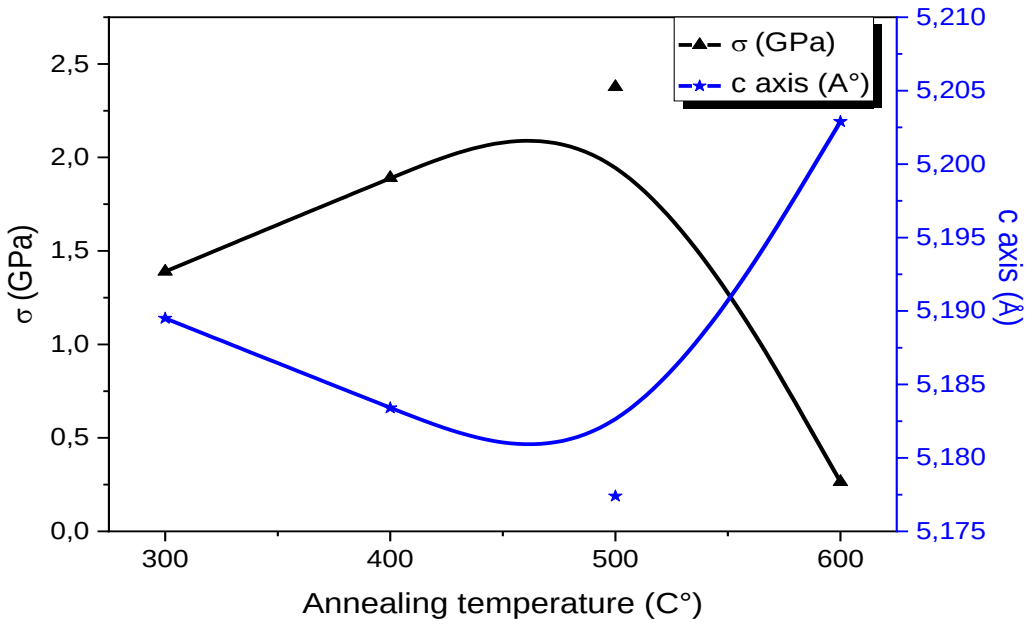

Figure V. 10. Stress σ and c-axis lattice parameter as a function of annealing temperature.

Table V. 3. The crystallite size, stress and c −axis lattice parameter of ZnO thin films.

T_a $(°C)$	D (nm)	σ (GPa)	c (Å)
300	16.29	1.390	5.190
400	24.65	1.891	5.183
500	35.91	2.377	5.177
600	39.95	0.269	5.203

V. 3. 2. Optical studies

The optical characterization has been done using $Perkin\ Elmer\ Lambda\ 25\ UV-VIS$ spectrophotometer with spectral range extends from wavelength $\lambda = 280\,nm$ to $1100\,nm$. The transmittance spectra are shown in fig V. 11.

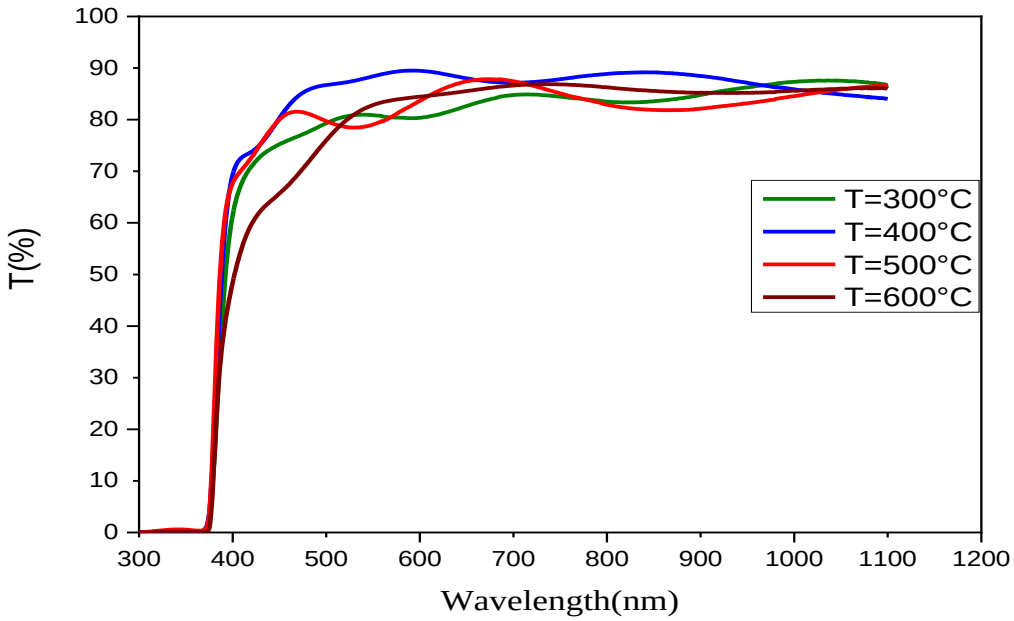

Figure. V. 11. Optical transmittance spectra of ZnO thin films annealed at different temperatures.

The optical transmission spectra of the films annealed at 300, 400, 500 and $600°C$ indicating a highly transparent material ($> 80\%$) in the visible range and a very weak transmittance in the UV close to 0 % for all films, it means strong absorbance for all films in the interval where $\lambda < 400\,nm$ due to the excitation and the migration of the electrons from the valence band to the conduction band. The absorption edge abrupt decay in the transmission spectra is characteristic of a semiconductor with direct forbidden energy band gap Eg.

V. 3. 3. Films' thickness

We calculate the film thickness using the method of interference fringes (Swanepoel method). The values of the films thickness are represented in table V. 4 and fig V. 12. The thickness d decreases when T_a increases in the $300°C - 500°C$ interval and increases for $T_a = 600°C$. The behavior for $T_a \leq 500°C$ could be originated by the increment of material density owing to the evaporation of organic residual coming from the precursor solution, for $T_a > 500°C$ the softening of the glass substrate could influence an increasing of d by the

formation of an interlayer between the glass and the ZnO consisting of other oxide compounds of Si and Zn in amorphous phase [17].

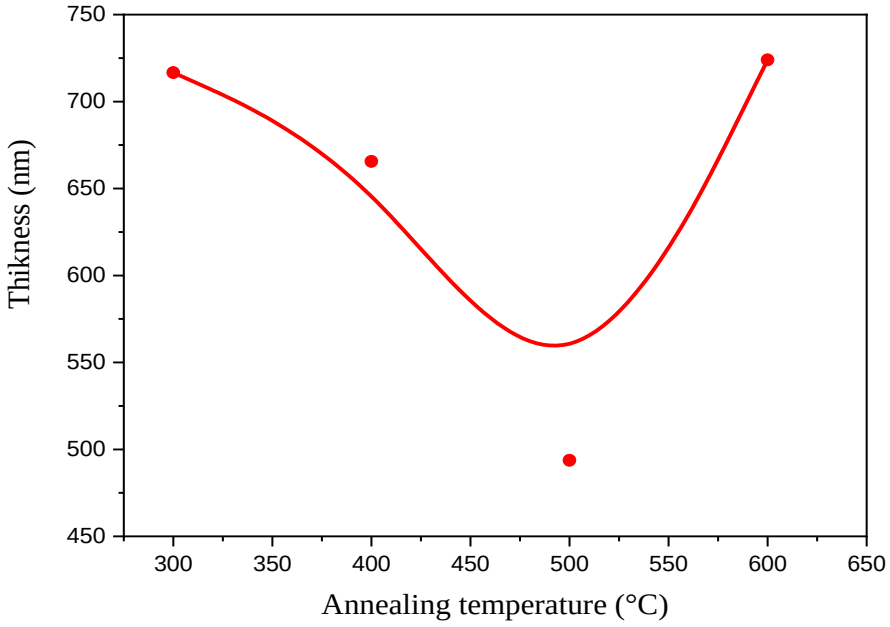

Figure. V. 12. The variations of the thickness d with annealing temperature.

V. 3. 4. Optical band gap and Disorder (Urbach energy)

We were estimated the optical gap Eg starting from Tauc's law. As shown in fig V. 13 using this method the band gap values of the ZnO thin films are located around 3.28 eV which is in good agreement with the Eg value of bulk ZnO $(3.2 - 3.3\ eV)$ [18]. From fig V. 13, the optical gap Eg exhibits a little increment which can be attributed to the growth of crystallite size which is resulted from the rise of annealing temperature the same outcome was found by V. Soleimanianet al [19].

The Urbach energy, corresponding with the tail width of the localized states within the optical band gap, thus it changes inversely with the optical band gap [10].

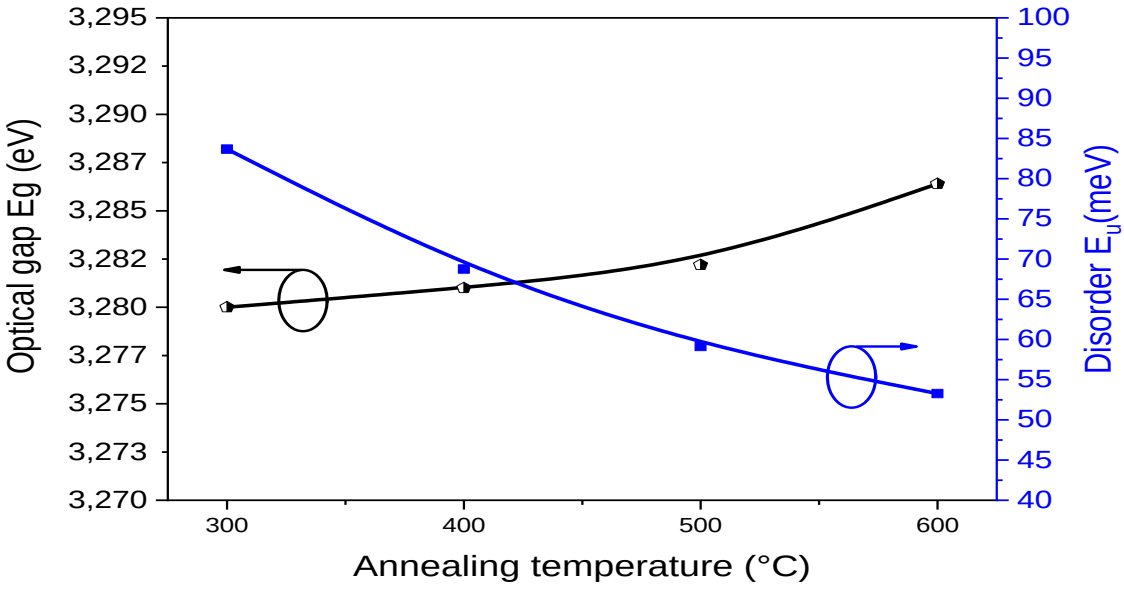

Figure. V. 13. Annealing temperature effect on the optical gap Eg and disorder Eu.

Table V. 4. Thickness, optical gap and Urbach energy of ZnO thin films.

$T_a\ (°C)$	$Thickness\ (nm)$	$\boldsymbol{Eg}\ (eV)$	$\boldsymbol{Eu}\ (meV)$
300	716.65	3.280	83.68
400	665.59	3.281	68.76
500	493.69	3.282	59.12
600	723.98	3.286	53.26

V. 3. 5. Electrical conductivity

We measured the electrical conductivity with two-point probe method after the deposition of metallic contacts by sputtering. The measures of $R\ (Giga\ Ohm)$ were obtained by a picoamperemeter ($Keithley\ 617$). As can be seen from the table V. 5 ZnO films exhibit low electrical conductivity due the effect of factors like defect association and chemical changes especially for sol–gel films which cannot be ruled out [20].

Table V. 5. Electrical resistance R and conductivity σ.

$T_a\ (°C)$	$R(G.\Omega)$	$\sigma.10^{-6}\ (\Omega.cm)^{-1}$
300	2.087	1.12
400	6.847	0.389
500	2.045	2.86
600	2.681	1.34

V. 4. Ga-doped ZnO

Gallium (III) nitrate hydrate was used as Ga source to doped ZnO films, where Ga/Zn atomic percentage was changed from 0 to 3.33 $(at.\%)$ with step of $2/3$.

V. 4. 1. Thickness of the films

The film thickness d can be calculated from the mass of the coating m if the density of the deposit material ρ and the area A on which the material is deposited is known:

$$d = m/(A.\rho) \qquad \text{(V.5)}$$

For this method one has to bear in mind that the density of a coating may deviate significantly from that of the bulk (e.g. due to porosity). For exact measurements a sensitive balance is necessary. Using these methods, we obtained the results which are represented in the table below:

Table V. 6. Thickness of undoped and Ga doped ZnO thin films.

$Ga\ concentration\ (at.\%)$	0	0.67	1.33	2	2.67	3.33
$Thickness\ (nm)$	223.11	248,99	192.92	224.85	195.22	167.97

V. 4. 2. Structural charachteristics

Fig V. 14. shows XRD patterns of gallium doped zinc oxide thin films. It is clear that the (002) peak dominates in all patterns, which indicates that the GZO films are composed by highly c-axis oriented growth polycrystals. Preferred orientation effects are common in zinc oxide films, and the crystallites tend to pack in the c-direction along the (002) plane, which is

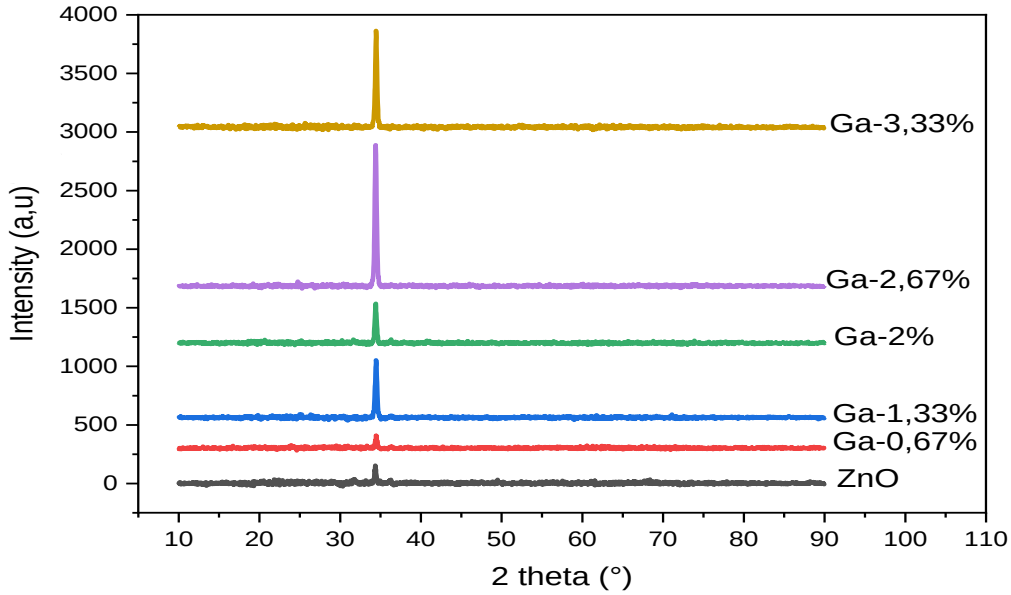

Figure V .14. XRD patterns of GZO thin films.

the most energetically stable crystal plane in zinc oxide as investigated before. But there also has been a long discussion in the literatures about the dominant mechanism of this texture formation should be a preferred nucleation or selective film growth. No reflections due to other phases, e.g. Ga_2O_3, were detected suggesting that these samples are composed of only the ZnO phase. The Ga −doped ZnO films exhibited a higher peak intensity than undoped ZnO. The (002) diffraction angle for the studied GZO films are listed in table V. 6 It can be seen that the 2θ values are all higher than that undoped one. According to the Bragg law $2d\sin\Theta = n\lambda$, the increase in diffraction angle corresponds to a reduction in the interplanar spacing d_{002}. As the Ga^{3+} has a smaller ionic radius with respect to Zn^{2+}, the substitution of Zn^{2+} with Ga^{3+} at lattice sites could decrease the lattice constant [21] and shift of the diffraction peaks toward greater angles.

By applying the Scherrer equation the average crystallite size has been estimated and given in the table V. 7 and fig V. 15. The crystallite size decreases in GZO films compared to ZnO films which indicated shrinkage of crystallites after addition of Ga due to the substitution of Ga into ZnO lattice [22].

Table V. 7. 2 theta values of (002) and crystallite size of undoped and Ga −doped ZnO thin films.

$Ga\ (at\ \%)$	$2\theta\ (°)\ (002)$	$Crystallite\ size\ D\ (nm)$
0	34,37	32,44
0.67	34,46	30,36
1.33	34,46	27,81
2.00	34,42	28,90
2.67	34,40	28,10
3.33	34,46	29,01

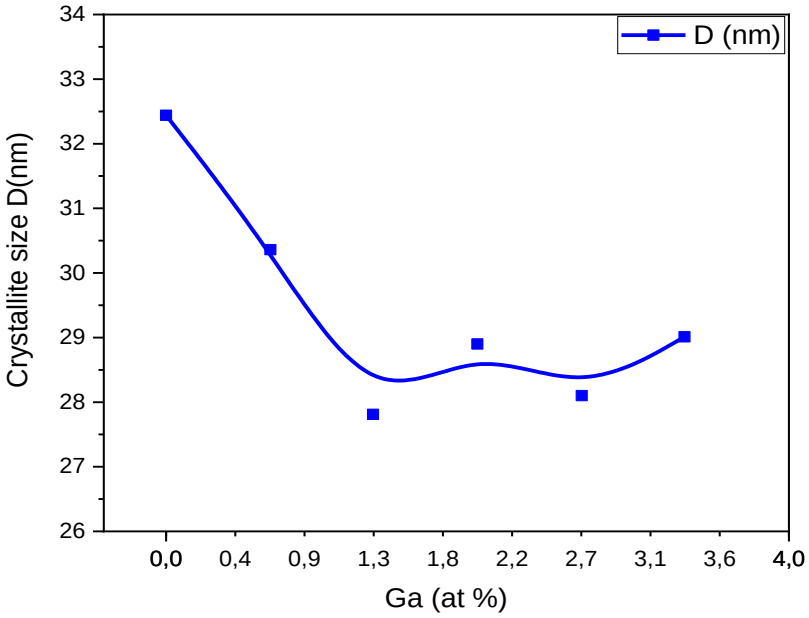

Figure V. 15. Effect of Ga doping on crystallite size.

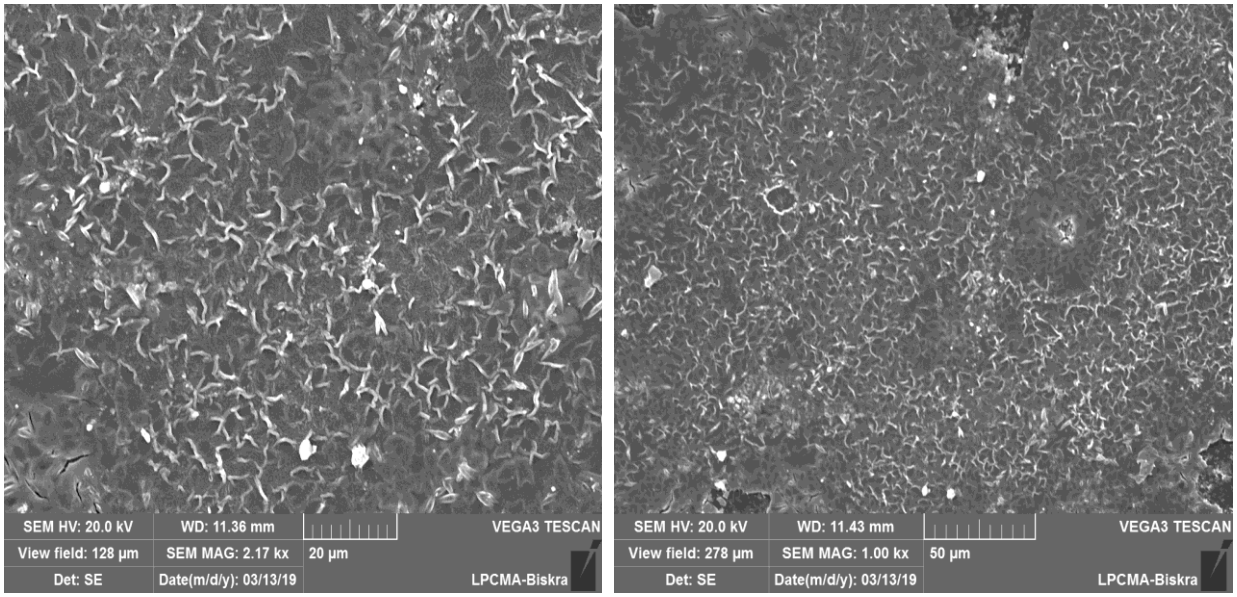

Figure V. 16. Scanning electron micrograph (SEM) of nanocrystalline Ga −doped ZnO $(2.67\ at.\%)$ at different magnifications.

Figure V. 16 shows the surface morphology of Ga −doped ZnO thin films by SEM. It is clear in the SEM images that the film is uniform and rough.

V. 4. 3. Optical study

Fig V. 17 shows the optical transmittance of undoped and Ga −doped ZnO films. All the films were highly transparent in the visible region. The optical properties of Ga −doped films are important to understand the effect of doping on the electronic structure of ZnO. The average transparency of films in the visible range was around 82%, which indicated a good structural homogeneity and crystallinity of ZnO films. The Ga −doped ZnO films exhibited a higher transparency than undoped films and this phenomenon can be attributed to the weakening of light scattering caused by enhancement of c-axis orientations after Ga doping. Also, the double shift phenomenon which were observed in all of the films is interpreted by the weak values of the thickness and it indicate the high degree of roughness of the films. In the other hand, the spectra present no interference fringes which confirm that the films are porous.

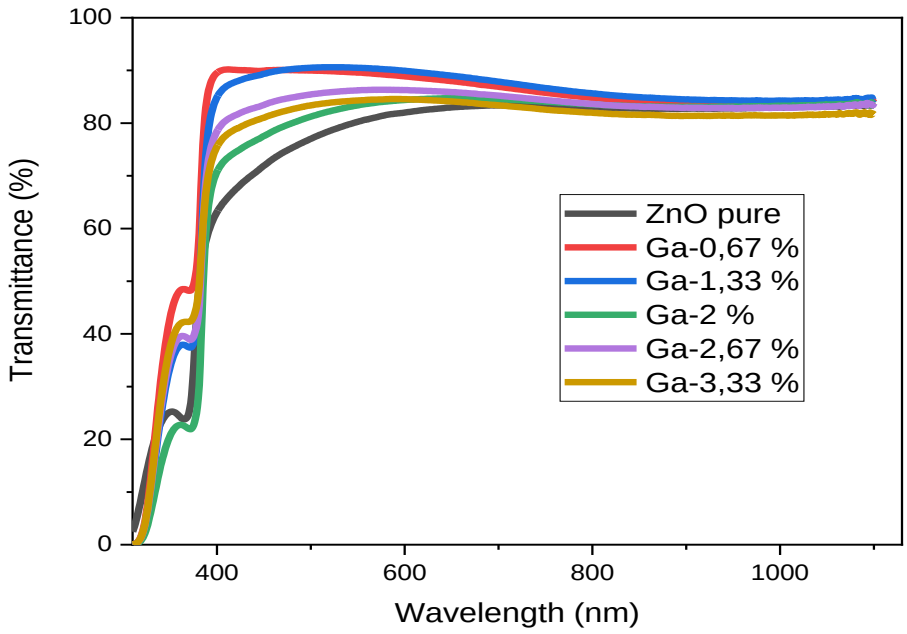

Figure. V. 17. Optical transmittance of undoped and Ga −doped ZnO films.

The optical band gap of undoped and Ga −doped ZnO thin films was estimated with the same steps which were cited previously, Eg variation is given in fig V. 18, from this figure we can remark that the Ga $(at.\%)$ doping leads to gap narrowing from 3.24 eV for undoped ZnO to 3.18 eV for high doping concentration (3.33 $at.\%$) owing to the donor level corresponding to Ga impurities localized below the bottom of conduction band. Tang et al [23] said that the donor energy level gradually widens and merges with conduction band which leads to decrease of ZnO band gap.

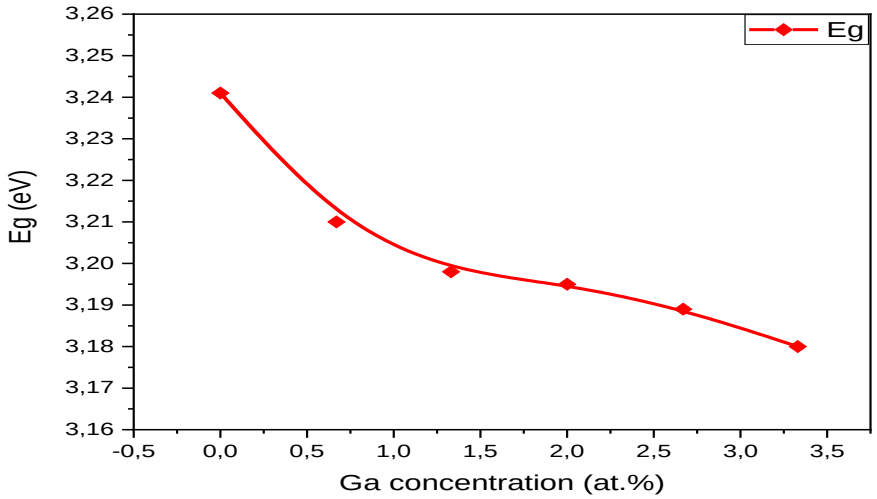

Figure. V. 18. Band gap variation with Ga-doping concentration.

V. 4. 4. Electrical properties

Four-point probe method was used to found the electrical conductivity which is presented in fig V. 19. Electrical conductivity increased with Ga concentration which is ascribed to the augmentation on carrier concentration (electrons) resulting from the difference in number of valence between Ga^{3+} and Zn^{2+}.

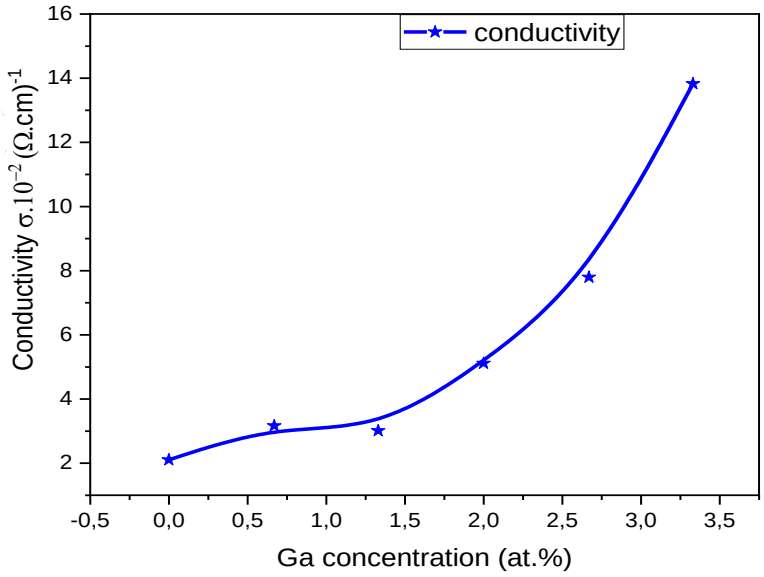

Figure. V. 19. Electrical conductivity as a function of Ga doping concentration.

References

[1] Z. Liu., Z. Jin., W. Li and J. Qiu, *"Preparation of ZnO porous thin films by sol–gel method using PEG template"*, Materials Letters 59(28), (2005) 3620 – 3625.

[2] H. B. Wannes., R. B. Zaghouani., R. Ouertani., A. Araújo., M. J. Mendes., H. Aguas., E. Fortunato., R. Martins and W. Dimassi, *"Study of the stabilizer influence on the structural and optical properties of sol-gel spin coated zinc oxide films"*, Materials Science in Semiconductor Processing, 74 (2018) 80–87.

[3] C. H. Ahn., Y. Y. Kim, D. C. Kim, S. K. Mohanta and H. K. Cho, *"A comparative analysis of deep level emission in ZnO layers deposited by various methods"*, Journal of applied Physics, 105(1), (2009) 013502.

[4] D. Wang., H. W. Seo., C. C. Tin., M. J. Bozack., J. R. Williams., M. Park., N. Sathitsuksanoh., A. J. Cheng and Y. H. Tzeng, *"Effects of post growth annealing treatment on the photoluminescence of zinc oxide nanorods"*, Journal of Applied Physics, 99(11), (2006) 113509.

[5] M. J. Chithra., M. Sathya and K. Pushpanathan, *"Effect of pH on crystal size and photoluminescence property of ZnO nanoparticles prepared by chemical precipitation method"*, Acta Metallurgica Sinica (English Letters), 28(3), (2015) 394-404.

[6] L. Znaidi, *"Sol–gel deposited ZnO thin films: A review"*, Materials Science and Engineering B, 174(1-3), (2010) 18–30.

[7] Y. Takahashi., M. Kanamori., A. Kondoh., H. Minoura and Y. Ohya, *"Photoconductivity of Ultrathin Zinc Oxide Films"*, Japanese Journal of Applied Physics 33 (12R), (1994) 6611-6615.

[8] H. S. Lee., J. Y. Lee., T. W. Kim., D. W. Kim and W. J. Cho, *"Formation mechanism of preferential c-axis oriented ZnO thin films grown on p-Si substrates"* . Journal of Material Science, 39(10), (2004) 3525-3528.

[9] Y. Zhang., W. Fa., F. Yang., Z. Zheng and P. Zhang, *"Effect of annealing temperature on the structural and optical properties of ZnO thin films prepared by sol–gel method*", Ionics, 16(9), (2010) 815 – 820.

[10] M. F. Malek., M. H. Mamat., M. Z. Musa., Z. Khusaimi., M. Z. Sahdan., A. B. Suriani., A. Ishak., I. Saurdi., S. A. Rahman and M. Rusop, *"Thermal annealing-induced formation of ZnO nanoparticles: Minimum strain and stress ameliorate preferred c-axis orientation and crystal-growth properties"*, Journal of Alloys and Compounds, 610, (2014) 575–588.

[11] W. Walter and S. Y. Chu, *"Physical and structural properties of ZnO sputtered films"*, Materials Letters, 55(1-2), (2002) 67-72.

[12] G. A. Kumar., M. R. Reddy and K. N. Reddy, *"Structural, Optical and Electrical Characteristics of Nanostructured ZnO Thin Films with various Thicknesses deposited by RF Magnetron Sputtering"*, Res. J. Physical Sci, 1(6), (2013) 17-23.

[13] T. B. Bateman, "Elastic Moduli of Single-Crystal Zinc Oxide", Journal of Applied Physics, 33(11), (1962) 3309-3312.

[14] M. Kim., K. Yim., J. Leem., S. Kim., G. Nam., D. Lee and J. Kim, *"Effects of Annealing Temperature on the Structural and the Optical Properties of ZnO Thin Films Grown on Porous Silicon by Using Plasma-assisted Molecular Beam Epitaxy"*, Journal of the Korean Physical Society, 59(3), (2011) 2343-2348.

[15] R. Ghosh., G. K. Paul and D. Basak, *"Effect of thermal annealing treatment on structural, electrical and optical properties of transparent sol–gel ZnO thin films"*, Materials Research Bulletin, 40(11), (2005) 1905–1914.

[16] M. Wang., J. Wang., W. Chen., Y. Cui and L. Wang, *"Effect of preheating and annealing temperatures on quality characteristics of ZnO thin film prepared by sol–gel method"*, Materials Chemistry and Physics, 97(2-3), (2006) 219–225.

[17] G. T. Delgado., C. Z. Romero, S. M. Hernández., R. C. Pérez and O. Z. Angel, *"Optical and structural properties of the sol–gel-prepared ZnO thin films and their effect on the photocatalytic activity"*, Solar Energy Materials and Solar Cells, 93(1), (2009) 55–59.

[18] T. K. Gupta, *"Application of Zinc Oxide Varistors"*, Journal of the American Ceramic Society, 73(7), (1990) 1817-1840.

[19] V. Soleimanian and S. R. Aghdaee, *"The influence of annealing temperature on the slip plane activity and optical properties of nanostructured ZnO films"*, Applied Surface Science, 258(4), (2011) 1495–1504.

[20] S. Bandyopadhyay., G. K. Paul., R. Roy., S. K. Sen and S. Sen, *"Study of structural and electrical properties of grain-boundary modified ZnO films prepared by sol–gel technique"*, Materials Chemistry and Physics, 74(1), (2002) 83–91.

[21] S. Liang and X. Bi, *"Structure, conductivity, and transparency of Ga-doped ZnO thin films arising from thickness contributions"*, Journal of Applied Physics, 104(11), (2008) 113533.

[22] Y. Hou and A. H. Jayatissa, *"Low resistive gallium doped nanocrystalline zinc oxide for gas sensor application via sol–gel process"*, Sensors and Actuators B: Chemical, 204 (2014) 310–318.

[23] G. Tang., H. Liu and W. Zhang, *"The Variation of Optical Band Gap for ZnO:In Films Prepared by Sol-Gel Technique"*, Advances in Materials Science and Engineering, 2013 (2013).

General conclusion and perspectives

The study presented in this thesis focused on the synthesis and characterization of two transparent conducting oxides which are Titanium dioxide and Zinc oxide via Sol-Gel spin coating as a wet chemical technique in order to investigate the effect of preparation parameters such as the nature of stabilizer, annealing temperature and doping on the structural, optical and electrical properties of these thin films aims to use it in photovoltaic applications.

In the first part of the experimental work we studied the influence of the deposition parameters which are: the nature of stabilizer, annealing temperature, molar concentration and Zn doping on the properties of TiO_2 thin films. The structural quality, transparency and conductivity of the films have been optimized. From the results obtained through the different characterizations and the corresponding discussions, we can conclude that: we have been able to deposit pure TiO_2 thin films using Acetylacetone as stabilizer at 600 °C and a molar concentration of 0.2 $mol.L^{-1}$ with: thickness less than 805 nm, crystallite size about 19.49 nm, and a transparency in the visible range around 88 %. Doping TiO_2 with Zn increased the conductivity from very low value to $\sim 10^{-4}(\Omega.cm)^{-1}$.

In the second part we have prepared and investigated the influence of the nature of stabilizer, annealing temperature and Ga doping on the properties of ZnO thin films. We have successfully obtained polycrystalline thin films of undoped and Ga doped ZnO using spin coating technique. The prepared ZnO thin films having good structural, optical and electrical properties at the optimized conditions such as: molar concentration of 0.6 $mol.L^{-1}$, annealing temperature equal to 600 °C and rotational speed of 4000 rpm, these conditions led to deposit ZnO thin films with interesting properties make it appropriate in the photovoltaic filed (high transparency reaches 86 % and a conductivity about 1.4×10^{-1} $(\Omega.cm)^{-1}$). Raising the annealing temperature leads to increased crystallite size which decreased the stress in the films and enhances the structural quality. Moreover, the effect of the doping amount on the conductivity value is very clear.

The comparison between the two obtained thin films shows that:

- Both TiO_2 and ZnO thin films show a preferential growth directions which are (101) and (002) respectively, with too small other peaks, this feature is ascribed to spin coating technique.

- The crystallite size found to increase with annealing temperature and have its largest value at 600 °C for TiO_2 and ZnO thin films. It should be note that the crystallite size of ZnO is higher than that of TiO_2.
- TiO_2 and ZnO thin films exhibit a transparency higher than 85 %. Moreover, both materials reveal that the acidic stabilizer is not suitable to deposit thin films with an acceptable transmission.
- Doping ZnO with Ga increases the conductivity from $2.1 \times 10^{-2}\ (\Omega.cm)^{-1}$ to $1.38 \times 10^{-1}\ (\Omega.cm)^{-1}$ whereas doping TiO_2 with Zn rises the conductivity value from the insulator range (not detectable) to semiconducting region $\sim 10^{-4}(\Omega.cm)^{-1}$.

Finally, the different perspectives that we can take into account to complete this work are:

- Some additional characterisations could still be made on the deposited films such as Hall effect, TEM and EDX …etc.
- Deposit TiO_2 and ZnO films at high temperatures using a different substrats such as ITO.
- Doping and co-doping TiO_2 films with other elements such as Cu…etc.
- Integrated the optimised films in one of the multiple applications such as transparent front electrodes for solar cells, photocatalysis, gas sensors…etc.

Annexes

Annex (A)

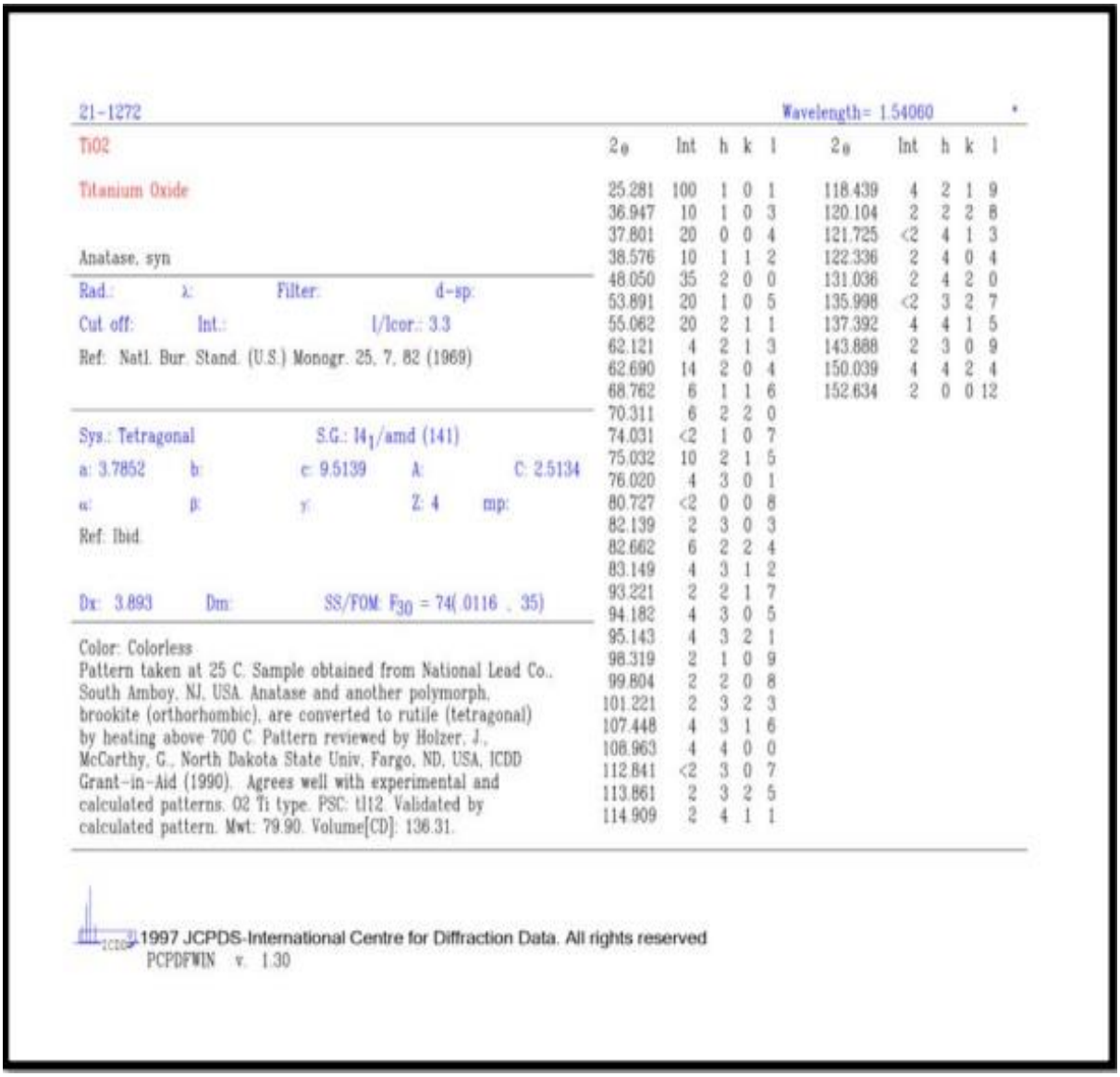

21-1272 Wavelength= 1.54060 *

TiO2

Titanium Oxide

Anatase, syn

Rad.: λ: Filter: d-sp:

Cut off: Int.: I/Icor.: 3.3

Ref: Natl. Bur. Stand. (U.S.) Monogr. 25, 7, 82 (1969)

Sys.: Tetragonal S.G.: $I4_1/amd$ (141)

a: 3.7852 b: c: 9.5139 A: C: 2.5134

α: β: γ: Z: 4 mp:

Ref: Ibid.

Dx: 3.893 Dm: SS/FOM: F_{30} = 74(.0116 , 35)

Color: Colorless

Pattern taken at 25 C. Sample obtained from National Lead Co., South Amboy, NJ, USA. Anatase and another polymorph, brookite (orthorhombic), are converted to rutile (tetragonal) by heating above 700 C. Pattern reviewed by Holzer, J., McCarthy, G., North Dakota State Univ, Fargo, ND, USA, ICDD Grant-in-Aid (1990). Agrees well with experimental and calculated patterns. O2 Ti type. PSC: tI12. Validated by calculated pattern. Mwt: 79.90. Volume[CD]: 136.31.

2θ	Int	h	k	l	2θ	Int	h	k	l
25.281	100	1	0	1	118.439	4	2	1	9
36.947	10	1	0	3	120.104	2	2	2	8
37.801	20	0	0	4	121.725	<2	4	1	3
38.576	10	1	1	2	122.336	2	4	0	4
48.050	35	2	0	0	131.036	2	4	2	0
53.891	20	1	0	5	135.998	<2	3	2	7
55.062	20	2	1	1	137.392	4	4	1	5
62.121	4	2	1	3	143.888	2	3	0	9
62.690	14	2	0	4	150.039	4	4	2	4
68.762	6	1	1	6	152.634	2	0	0	12
70.311	6	2	2	0					
74.031	<2	1	0	7					
75.032	10	2	1	5					
76.020	4	3	0	1					
80.727	<2	0	0	8					
82.139	2	3	0	3					
82.662	6	2	2	4					
83.149	4	3	1	2					
93.221	2	2	1	7					
94.182	4	3	0	5					
95.143	4	3	2	1					
98.319	2	1	0	9					
99.804	2	2	0	8					
101.221	2	3	2	3					
107.448	4	3	1	6					
108.963	4	4	0	0					
112.841	<2	3	0	7					
113.861	2	3	2	5					
114.909	2	4	1	1					

Figure 1. JCPDS card of anatase TiO_2.

Annex (B)

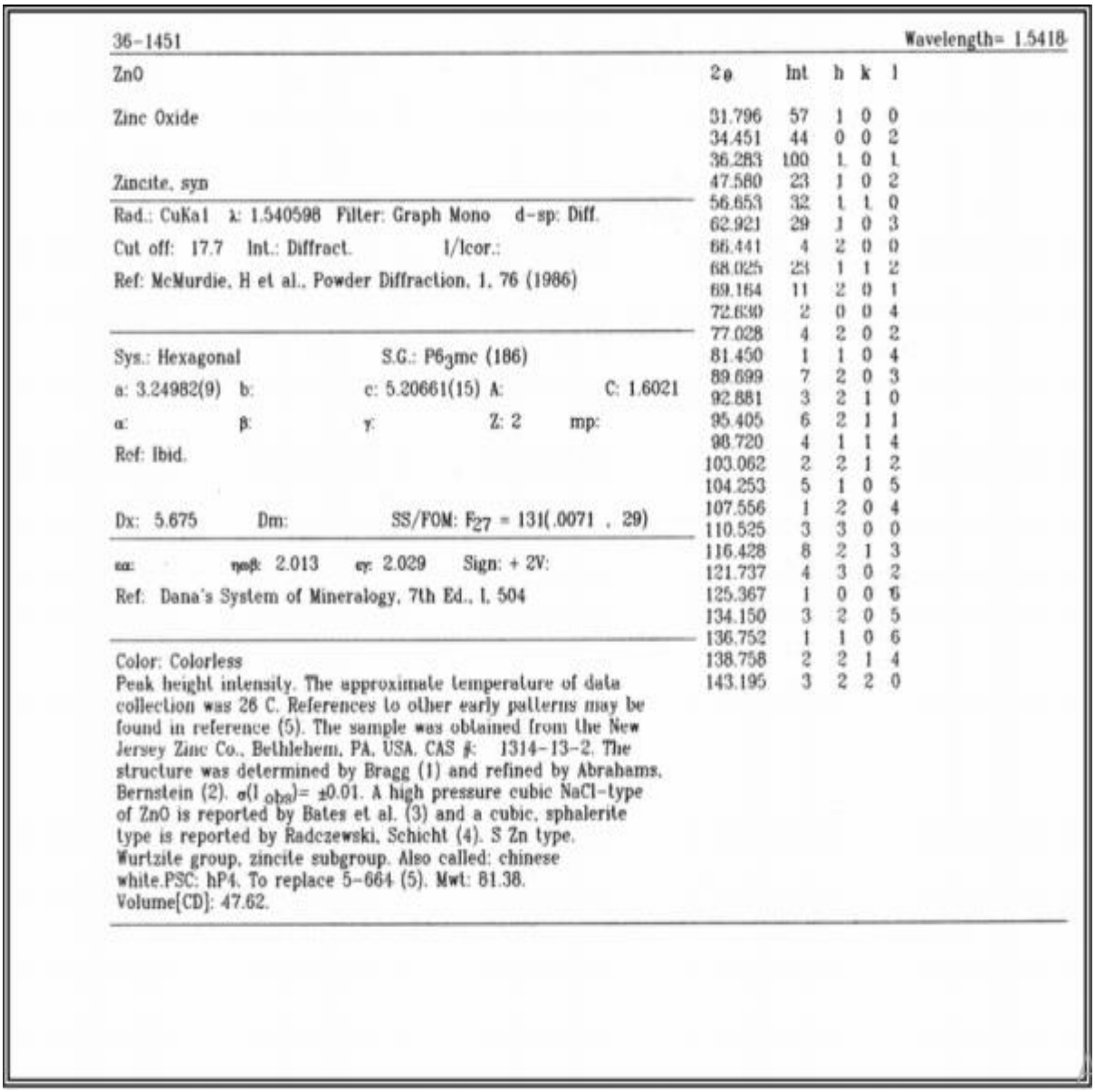

36-1451 Wavelength= 1.5418

ZnO

Zinc Oxide

Zincite, syn

Rad.: CuKa1 λ: 1.540598 Filter: Graph Mono d-sp: Diff.

Cut off: 17.7 Int.: Diffract. I/Icor.:

Ref: McMurdie, H et al., Powder Diffraction, 1, 76 (1986)

Sys.: Hexagonal S.G.: $P6_3mc$ (186)

a: 3.24982(9) b: c: 5.20661(15) A: C: 1.6021

α: β: γ: Z: 2 mp:

Ref: Ibid.

Dx: 5.675 Dm: SS/FOM: F_{27} = 131(.0071 , 29)

ωα: ηωβ: 2.013 εγ: 2.029 Sign: + 2V:

Ref: Dana's System of Mineralogy, 7th Ed., I, 504

Color: Colorless

Peak height intensity. The approximate temperature of data collection was 26 C. References to other early patterns may be found in reference (5). The sample was obtained from the New Jersey Zinc Co., Bethlehem, PA, USA. CAS #: 1314-13-2. The structure was determined by Bragg (1) and refined by Abrahams, Bernstein (2). $\sigma(I_{obs})$= ±0.01. A high pressure cubic NaCl-type of ZnO is reported by Bates et al. (3) and a cubic, sphalerite type is reported by Radczewski, Schicht (4). S Zn type. Wurtzite group, zincite subgroup. Also called: chinese white.PSC: hP4. To replace 5-664 (5). Mwt: 81.38. Volume[CD]: 47.62.

2θ	Int	h	k	l
31.796	57	1	0	0
34.451	44	0	0	2
36.283	100	1	0	1
47.580	23	1	0	2
56.653	32	1	1	0
62.921	29	1	0	3
66.441	4	2	0	0
68.025	23	1	1	2
69.164	11	2	0	1
72.630	2	0	0	4
77.028	4	2	0	2
81.450	1	1	0	4
89.699	7	2	0	3
92.881	3	2	1	0
95.405	6	2	1	1
98.720	4	1	1	4
103.062	2	2	1	2
104.253	5	1	0	5
107.556	1	2	0	4
110.525	3	3	0	0
116.428	8	2	1	3
121.737	4	3	0	2
125.367	1	0	0	6
134.150	3	2	0	5
136.752	1	1	0	6
138.758	2	2	1	4
143.195	3	2	2	0

Figure 2. JCPDS card of ZnO.

Annex (C)

Two-point probe method

For this method of measurement two metallic (Gold) contacts were deposited by sputtering. The value of resistance R (Giga Ohm) were directly obtained by a picoamperemeter and the conductivity σ value is deduced from:

$$\sigma = (1/R) \times (L/W.d)$$

Where:

R: is the resistance.

L: the distance between the two contacts $(L = 2mm)$.

W: the channel width.

d: the thickness of the film.

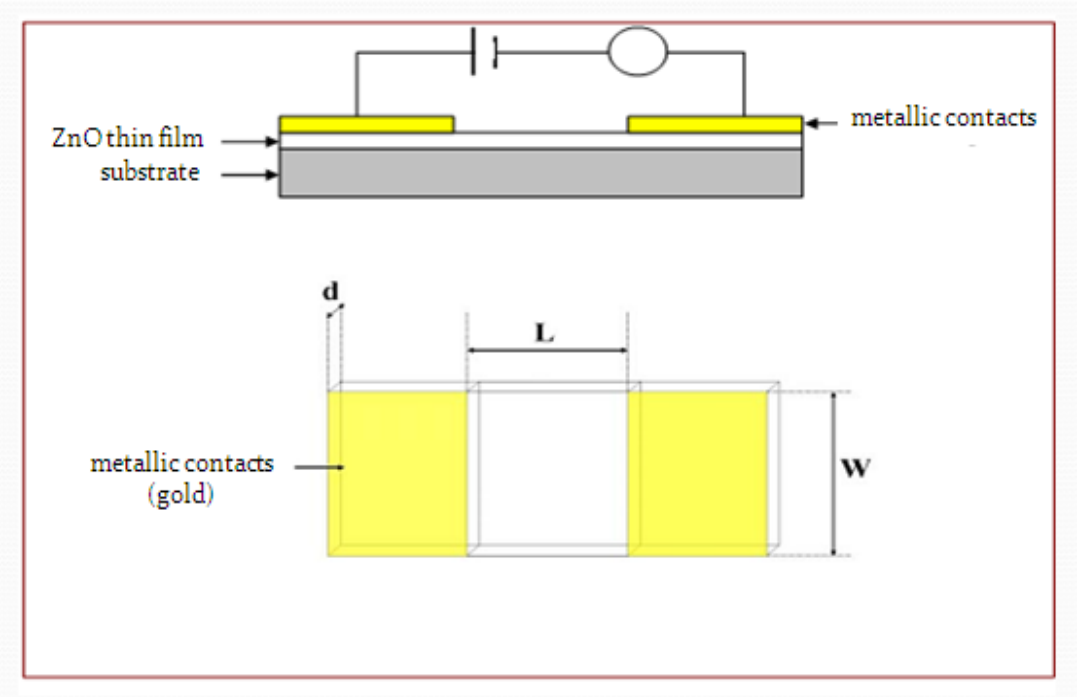

Figure 3. Two-point probe method.

Annex (D)

When interatomic distance, length or angle of bond is changes within the material it appears what is called a “disorder”. In this case, the band edges described in the case of crystalline lattice which is delimited by Ev and Ec is disappear and leads to what is known as localized states forming band tails at the border of the forbidden band in the valence band and conduction band (figure below).

When the disorder becomes too great, the tails can get attached, we will then define the notion of Urbach parameter which corresponds to transitions between the extended states of the valence band and the localized states of the conduction band.

According to the Urbach law the expression of the absorption coefficient is as follows [1]:

$$\alpha(h\nu) = \alpha_0 exp\ (h\nu/E_u)$$

By tracing $ln\ (\alpha)$ as function of $h\nu$ we can establish the E_u value.

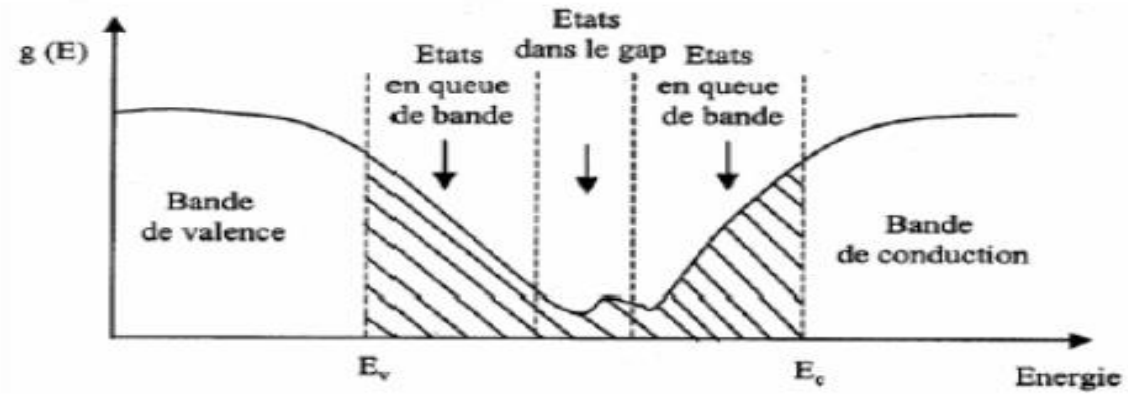

Figure 4. Density of states function in a semiconductor [2].

References

[1] F. Urbach, *"The long-wavelength edge of photographic sensitivity and of the electronic absorption of solids"*, Physical Review, 92(5), (1953) 1324.

[2] A. Moustaghfir, *"Élaboration et caractérisation de couches minces d’oxyde de zinc. Application à la photoprotection du polycarbonate"*, Doctorat thesis, Université Blaise Pascal, France, (2004).

Abstract

Preparation and characterization of Titanium dioxide and Zinc oxide thin films via Sol-Gel (spin coating) technique for optoelectronic applications

In the present work we used Sol-Gel spin coating technique to deposit Titanium dioxide and Zinc oxide thin films. Our main goal is the production of films with suitable optoelectronic properties required for application as front transparent electrodes. In the first part we have prepared and characterized Titanium dioxide by varying the deposition parameters such as: the nature of stabilizer, annealing temperature, molar concentration and Zn doping, this last is accomplished with the goal to enhance the electrical properties.

In the second part of this work we have deposited and studied the influence of the nature of stabilizer, annealing temperature and Ga doping on the properties of ZnO thin films. The structural, optical and electrical properties were investigated through: X-ray diffraction, Fourier transform-infrared, Photoluminescence, Raman spectroscopy, UV-visible spectroscopy, Scanning electron microscopy and Four-point probe method.

Key words: Thin films, Sol-Gel spin coating, Titanium dioxide, Zinc oxide, optical properties, electrical properties, optoelectronic applications.

مُلخّص:

ترسيب وتخصيص الشّرائح الرّقيقة لأكسيد التيتان وأُكسيد الخارصين بتقنية سائل – هلام (طريقة الترسيب باللف) من أجل التطبيقات الكهروضوئية

في هذا العمل استخدمنا تقنية سائل-هُلام (تقنية التّرسيب باللّف) لترسيب شرائح ثنائي أكسيد التيتان وأكسيد الخارصين. الهدف من هذا العمل هو تحضير شرائح رقيقة بخصائص كهروضوئية مُناسبة لتطبيقها كتماسات أمامية شفّافة. في الجزء الأوّل قُمنا بتحضير وتخصيص ثُنائي أكسيد التيتان بتغيير شروط التّرسيب التّالية: طبيعة الوسيط ودرجة حرارة التّلدين والتّركيز المولي وكذلك نسبة التّطعيم بالخارصين هذا الأخير كان الهدف منه تحسين الخصائص الكهربائية.

في الجزء الثّاني من هذا العمل قُمنا بترسيب شرائح أكسيد الخارصين ودراسة تأثير طبيعة الوسيط ودرجة حرارة التّلدين ونسبة التّطعيم بالغاليوم على خصائص هذه الشرائح. كما قُمنا بدراسة الخصائص البنيوية والضّوئية والكهربائية باستعمال تقنيات التّوصيف التّالية: انعراج الأشعّة السّينية – مطيافية الأشعة تحت الحمراء الخاضعة لتحويل Fourier – التّألّق الضّوئي – مطيافية Raman - مطيافية الأشعّة فوق البنفسجية-المرئية – المجهر الإلكتروني الماسح وتقنية المسابير الأربعة.

الكلمات المفتاحية: الطّبقات الرقيقة، سائل-هُلام (التّرسيب باللّف)، ثُنائي أكسيد التيتان، أكسيد الخارصين، الخصائص الضّوئية، الخصائص الكهربائية، التّطبيقات الكهروضوئية.

Résumé

Préparation et caractérisation de couches minces de dioxyde de Titane et d'oxyde de Zinc par la technique Sol-Gel (spin-coating) pour des applications optoélectroniques

Dans ce travail, nous avons utilisé la technique Sol-Gel revêtement par rotation pour déposer des couches minces de dioxyde de titane et d'oxyde de zinc. Notre objectif principal est la production de films avec des propriétés optoélectroniques appropriées requises pour une application en tant qu'électrodes transparentes. Dans la première partie, nous avons préparé et caractérisé le dioxyde de titane en faisant varier les paramètres de dépôt tels que : la nature du stabiliseur, la température de recuit, la concentration molaire et le dopage par Zn, ce dernier est accompli dans le but d'améliorer les propriétés électriques.

Dans la deuxième partie de ce travail, nous avons déposé et étudié l'influence de la nature du stabiliseur, la température de recuit et du dopage par Ga sur les propriétés des couches minces de ZnO. Les propriétés structurelles, optiques et électriques ont été étudiées par : diffraction des rayons X, infrarouge à transformée de Fourier, photoluminescence, spectroscopie Raman, spectroscopie UV-visible, microscopie électronique à balayage et méthode de quatre points.

Mots clés : Couches minces, Sol-Gel revêtement par rotation, Dioxyde de Titane, Oxyde de Zinc, propriétés optiques, propriétés électriques, applications optoélectroniques.